Observation of sulphate aerosols and SO_2 from volcanic eruptions using data from the Atmospheric Chemistry Experiment (ACE)

presented by

Debora Doeringer

MSc by research

Department of Physics at the University of York

- July 2011 -

Observation of sulphate aerosols and SO_2 from volcanic eruptions using data from the Atmospheric Chemistry Experiment (ACE)

Infrared spectra measured by the Atmospheric Chemistry Experiment Fourier Transform Spectrometer (ACE-FTS) on board of the SCISAT satellite were used to analyse the temporal and spatial evolution of volcanic aerosols from the Kasatochi (August 2008), Sarychev (June 2009) and Grimsvötn (May 2011) eruptions. Evidence of the Kasatochi and Sarychev eruptions has first be seen one month after the eruptions, while the Grimsvötn plume has been detected with a maximum age of 3 days, from enhanced SO_2 concentrations and atmospheric extinction. Evidence for differences within these plumes have been obtained, showing the evolution of H_2SO_4 from no sulphate aerosol signature in fresh volcanic plumes to clear signatures in aged volcanic plumes. The atmosphere had returned to pre-eruption conditions, between seven and eight months after the eruptions of Kasatochi and Sarychev.

The first SO_2 and sulphate aerosol retrievals determined using the infrared solar occultation spectra recorded with ACE-FTS are presented here. The size distribution parameters, aerosol volume slant column and composition of the sulphate aerosol were obtained using a least-squares algorithm, employing a continuum spectrum between $800 - 4200\,\mathrm{cm}^{-1}$. The maximum volume slant column of the aerosol was found to be $500\,\mu\mathrm{m}^3\,\mathrm{cm}^{-3}\,\mathrm{km}$ (for Kasatochi) and $850\,\mu\mathrm{m}^3\,\mathrm{cm}^{-3}\,\mathrm{km}$ (for Sarychev), which results in an approximate aerosol loading of $1.8\,\mu\mathrm{m}^3\mathrm{cm}^{-3}$ and $3\,\mu\mathrm{m}^3\mathrm{cm}^{-3}$, respectively. One month after the eruptions the effective radius (R_{eff}) is below $0.2\,\mu\mathrm{m}$ (Kasatochi) and $0.1 - 0.3\,\mu\mathrm{m}$ (Sarychev).

Contents

1. Introduction

The influence of volcanic eruptions on the Earth's climate has been observed for hundreds of years. In May 1784, Benjamin Franklin mentioned fog over North America and Europe, probably from volcanic eruptions, lowering the Earth's temperature in winter $1783 - 1784$ and leading to early frost in 1784 (*Humphreys*, 1929). Sulphuric acid aerosols and small dust particles are primarily responsible for this cooling by increasing the albedo of clouds and reflecting more solar radiation to space, leading to a net cooling of the lower atmosphere (*Pollack et al.*, 1976). This effect is especially strong for volcanic eruptions whose plumes reach the stratosphere. In the last 50 years, major volcanic eruptions have increased the total optical depth in the lower stratosphere and upper troposphere (*Sato et al.*, 1993). The large eruptions of Mt. Pinatubo in 1991, for example, increased the atmospheric optical depth at 550 nm to approximately $0.15 - 0.20$ (*Sato et al.*, 1993), causing a decrease in temperature of 0.7 K in the lower troposphere of the Northern Hemisphere in September 1992 (*Dutton and Christy*, 1992). However, inside the volcanic plume a net warming is caused due to the absorption of infrared radiation by larger aerosol particles (*Pollack et al.*, 1976). Due to their longer lifetime in the stratosphere, the influence of sulphur dioxide and aerosols is enhanced, leading to a stronger and more significant effect on the scattering of solar radiation.

Typically, stratospheric aerosols have a diameter between $0.01\,\mu$m and $10\,\mu$m. As mentioned above, stratospheric aerosols have a much longer lifetime than tropospheric aerosols. Figure 1.1 illustrates the removal of stratospheric aerosol, which can take up to several years, considering the aerosol is stable and is not removed by chemical processes. Aerosols of this size are usually removed by wet deposition. The water vapour in the stratosphere is very low and, therefore, clouds do not form. Generally, stable stratospheric aerosols have to mix into the troposphere, where they can be removed from the atmosphere by wet decomposition within a few days. Other processes for the removal of aerosols from the troposphere include coagulation for a particle diameter up to $0.01\,\mu$m and sedimentation for large particles with a minimum diameter of approximately $10\,\mu$m.

Aerosol particles can act as cloud condensation nuclei (CCN) and change the properties of clouds. There are two main reaction processes, which remove SO_2 by building sulphuric acid molecules. Sulphur dioxide molecules (SO_2) are oxidised by OH radicals to sulphuric acid (H_2SO_4), this process is relatively slow and happens on a time-scale of several weeks (*Reiner and Arnold*, 1994). However, in the atmosphere between 60 % and 80 % of SO_2 is removed by an aqueous phase process, where the sulphuric acid in the atmosphere originates from aqueous oxidation of SO_2 by H_2O_2 inside clouds (*Reeves and Penkett*, 2003). A few days after the typical volcanic eruptions only aqueous H_2SO_4 aerosol particles have been observed, the ash particles did not remain (*Karagulian et al.*, 2010).

In the stratosphere, the influence of SO_2 and sulphuric acid on the climate is quite strong. The main sources of stratospheric SO_2 are large volcanic eruptions. Other anthropogenic and natural SO_2 sources, cannot reach these high altitudes. Therefore, as shown in Figure 1.1 the produced sulphate aerosols have a typical lifetime of a few days, whereas the aerosols caused by strato-volcanic eruptions can stay in the atmosphere up to a few years. Understanding of the effect of aerosols on clouds and their effect on radiative forcing due to aerosols is relatively low and the assumed effects

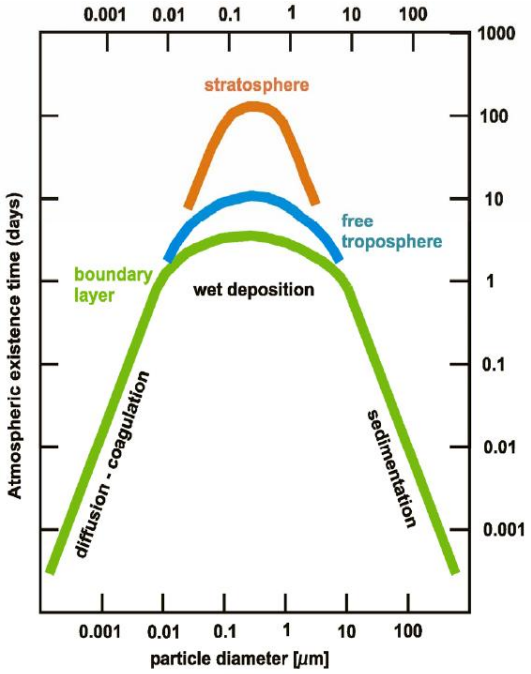

Figure 1.1: Approximate scale of the lifetime of aerosols in different layers of the atmosphere. The removal of aerosols in the stratosphere happens in a magnitude of years. Also displayed is the typical size range of the aerosols. After (*Jaenicke*, 1978)

have large uncertainties. This shows that scientific research is needed into this area to acquire a better understanding of atmospheric processes and changes. The widely discussed stratospheric geo-engineering, where SO_2 would be spread out in the stratosphere around the globe to reduce the effect of global warming, requires knowledge of the influence of stratospheric SO_2 on atmospheric chemistry.

In this study the eruptions have been observed of Sarychev (located at 48°N, 153°E) and Kasatochi (located at 52°N, 175°W). The Sarychev volcano erupted explosively between $12-17$ June 2009 with a plume height of about 9.7 km (*AURA*, 2009). During this period approximately 1.2 ± 0.2 Tg of SO_2 and ash were injected in the upper troposphere and lower stratosphere (*Haywood et al.*, 2010). The Kasatochi volcano, situated in one of the Andreanof Islands, an island group in Alaska, erupted explosively on the 7 August 2008. During these eruptions 1.7 Tg SO_2 were injected in the upper troposphere and lower stratosphere (*Karagulian et al.*, 2010). The volcanic eruptions led to twice the aerosol optical density, approximately two months after the eruptions.

The observations are made with the data from Atmospheric Chemistry Experiment (ACE), which is the mission for the first science satellite, SCISAT, from the Canadian Space Agency (CSA), launched by the National Aeronautics and Space Administration (NASA) on 12 August 2003. The satellite covers tropical, mid-latitude and polar regions between 85°S and 85°N (*Bernath et al.*, 2005). ACE is equipped with three instruments with the primary goal of a better understanding of the processes damaging the Earth's atmosphere. The primary observation technique is solar occultation at sunrise (sr) and sunset (ss) using the three different instruments: a high-resolution infrared Fourier Transform Spectrometer (FTS), which covers a range of $750-4400$ cm^{-1}

with a resolution of 0.02 cm^{-1}. MAESTRO (Measurement of Aerosol Extinction in the Stratosphere and TRoposphere by Occultation) detects the visible and near-infrared spectrum ($400 - 1030$ nm, with a resolution of $1 - 2$ nm) (*Bernath et al.*, 2005; *McElroy et al.*, 2007). And two filtered imagers monitor clouds and aerosols by measuring atmospheric extinction in the near-infrared (NIR) at 1020 nm and in the visible region (VIS) at 525 nm.

The aim of this study is to show the temporal and spatial variation of volcanic plumes with the example of Sarychev and Kasatochi using ACE data. For the first time the SO_2 volume mixing ratio, which is a clear indicator for volcanic plumes, is successfully retrieved from ACE-FTS. In this thesis it is also shown that with ACE data it is possible to analyse a volcanic plume of atmospheric and aerosol extinction, SO_2 volume mixing ratio and aerosol properties, including an aerosol density profile, aerosol composition and size distribution. A considerable aerosol layer can be seen in the upper troposphere and lower stratosphere in July 2009, the month after the Sarychev eruptions and in September 2008, the month after the Kasatochi eruptions in the Northern Hemisphere. The temporal variation is illustrated, showing that there are significantly different post-Sarychev conditions and post-Kasatochi conditions, respectively. According to the median optical depth, pre-Sarychev and pre-Kasatochi conditions are reached again several months after the eruptions. The volcanic aerosol properties for certain occultations in July 2009 and September 2008 are retrieved using a χ^2-minimizing method for a unimodal log-normal size distribution model. To estimate the vertical concentration profile, the retrieved slant columns are inverted into an aerosol loading. The wide spectral range ($800 - 4100$ cm^{-1}) with a high resolution from ACE-FTS provides some information about the aerosol size distribution and makes it possible to derive radii and effective radii of volcanic aerosols after large volcanic eruptions with the data from ACE-FTS.

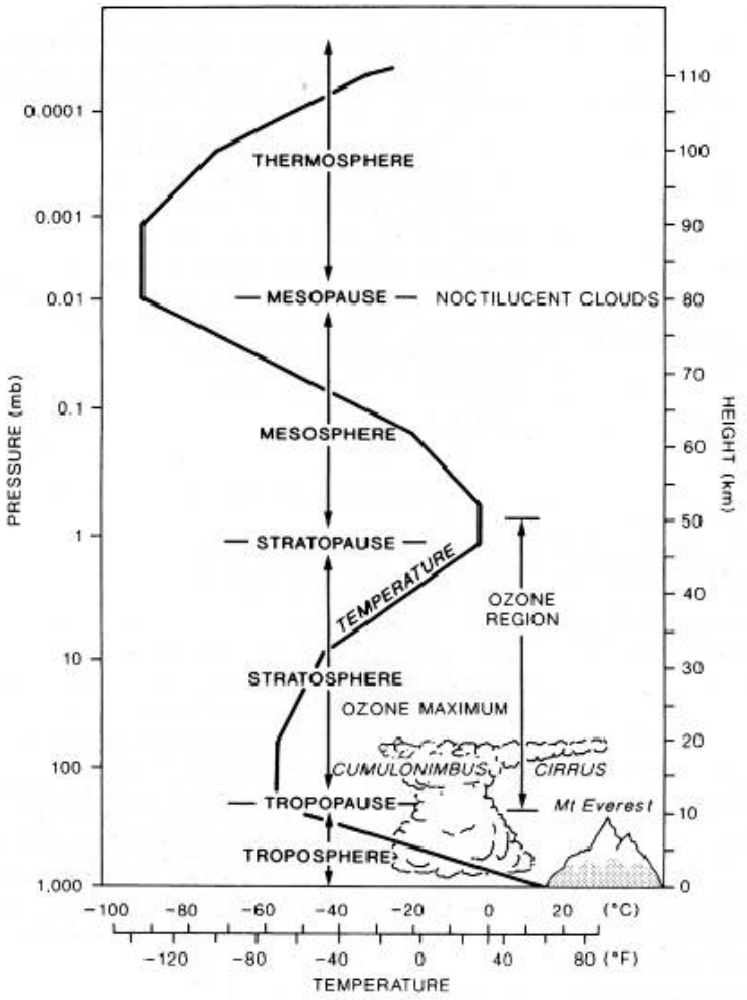

Figure 2.1: Vertical extent (at mid-latitudes) of the Earth's atmosphere, shown are the different layers of the atmosphere defined by the temperature profile (*Barry and Chorley*, 2003).

2. Atmospheric Chemistry and Volcanology

2.1. Atmospheric chemistry and transport

2.1.1. Structure and temporal scales of the atmosphere

An atmosphere is the layer of gas around a planet, affected and held together by the gravity of the body. The atmosphere of the Earth has a very important impact on life on Earth, for example gases, like diatomic oxygen (O_2) or carbon dioxide (CO_2), in the atmosphere are necessary for the aerobic metabolism of many organisms. The natural greenhouse effect, mainly because of the absorption of solar radiation from water vapour and carbon dioxide, creates a temperature on Earth (about 33 K warmer than if there would be no atmosphere), warm enough to form liquid water. Ozone (O_3) in the stratosphere is fundamental for protection of high-energetic solar radiation (UV).

The profile of the atmosphere can be defined in different ways, e.g. by the temperature profile, the mixing ratio, or electric charge in different layers. The most common classification is by the temperature profile, which is shown in Figure 2.1. It shows, the

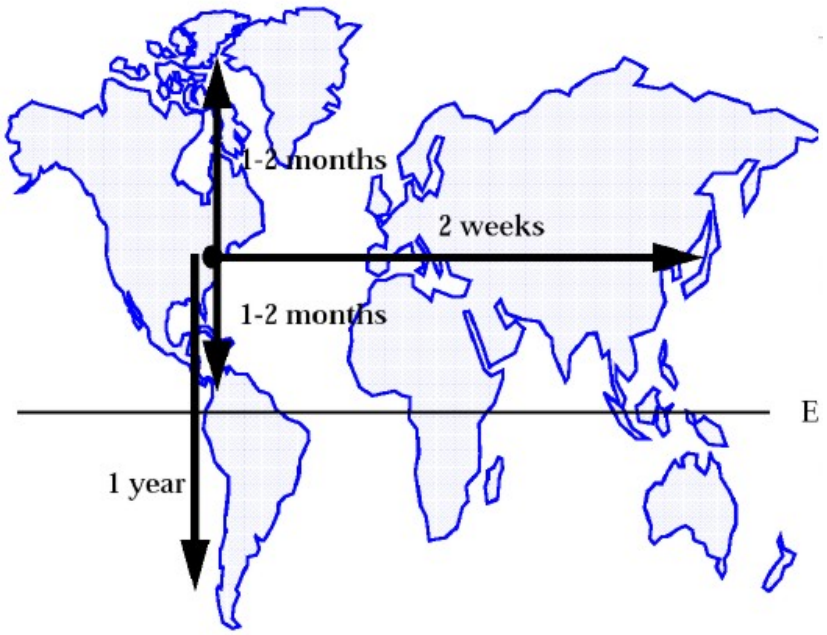

Figure 2.2: The schematic diagram shows the mean transport times intra and inter the hemispheres. (*Jacob*, 1999)

layer, the closest to the Earth's surface is the troposphere, which can reach up to 18 km in the tropics. In the troposphere, the actual temperature decreases with altitude on average by 6.5 $\mathrm{K\,km^{-1}}$. Because of the constant cold temperature in the tropopause acting like a cold trap, nearly all the water in the atmosphere is contained in the troposphere, leading to a dry stratosphere. It is also the layer dominated by convection from ascending and descending forces resulting in mostly turbulent conditions. The stratosphere reaches up to 50 km, containing most of the atmosphere's ozone. In this layer the actual temperature increases with altitude due to absorption of short wavelength solar radiation by ozone. The temperature decreases above the stratosphere, in the mesosphere, up to an altitude of 80 km. Above the mesosphere the particle density is extremely low, and contains mainly molecular and atomic oxygen and nitrogen. The absorption of solar UV radiation from oxygen molecules results in a temperature increase in the thermosphere. In the exosphere, above 500 km, hydrogen and helium can escape into outer space. (*Roedel*, 2000; *Barry and Chorley*, 2003; *Seinfeld and Pandis*, 1998; *Houghton*, 2003)

Circulation of the atmosphere around the Earth is due to the radiant energy unbalance. This unbalance leads to an atmospheric motion from high radiant energy regions (tropics) to low radiant energy regions (poles). This circulation due to the Coriolis force, resulting from the rotation of the Earth causes break-ups in the atmospheric circulation at 30° and 55° N and S.

In Figure 2.2 the mean transport time in the atmosphere of intra and inter the hemispheres is shown. It takes around two weeks to mix a species around the Earth, within the latitudinal range. The mixing throughout the whole hemisphere takes between one and two months, while it needs approximately one year for mixing throughout the whole Earth in the lower atmospheric layers.

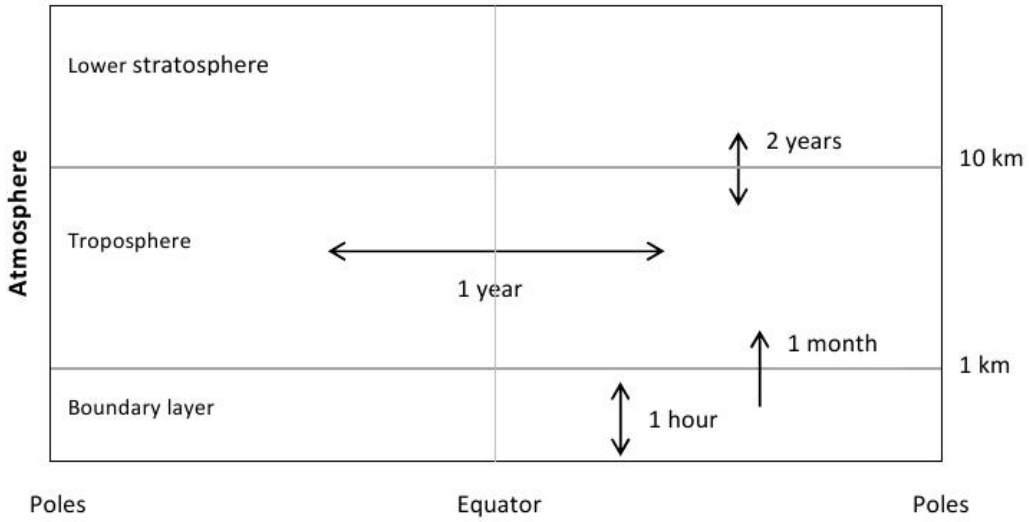

Figure 2.3: Illustration of the mean transport time between the lower layers of the atmosphere. The exchange between the troposphere and the stratosphere accounts for 2 years. It takes about one hour to mix a species from the Earth's surface to about 1 km and 1 month to leave the planetary boundary layer. After (*Jacobson*, 1999).

The transport inside low atmospheric layers is illustrated in Figure 2.3 and shows a mean transport time between the troposphere and the stratosphere of 2 years. The transfer from the troposphere to the stratosphere mostly takes place in the tropics, where a pumping from extra-tropical stratosphere causes a net flux and pushes downwards in the polar regions.

The lifetime of aerosols in the stratosphere is relatively high because of the lack of water vapour and therefore precipitation. The only limitation of the lifetime, apart from chemical reactions, is due to the mixing between the stratosphere and troposphere, where the species can rain out. Therefore, aerosols in the stratosphere can have a much stronger impact on climate change because of their long lifetime. Only very strong volcanic eruptions can inject gases and ash particles directly into the stratosphere, and in these cases, they have a very strong impact on the chemical and physical conditions of the atmosphere.

2.1.2. Absorption and scattering of solar radiation

In Figure 2.4, the spectrum of the solar radiation is shown. The dashed line symbolises the unperturbed emission spectrum of a black body at 6000 K (approximate temperature of the Sun). Below the dashed line, the actual solar spectrum above the Earth's atmosphere is shown, which is different from the black body radiation due to the Sun's atmosphere and cooler and warmer layers in the Sun. The lower solid line in Figure 2.4 shows the approximate solar spectrum on the Earth's surface after passing through the Earth's atmosphere. Four main processes influence the solar radiation reaching the Earth's surface by passing through the atmosphere: (1) the absorption because of gases, (2) the emission of radiation due to gases, (3) scattering out of the beam

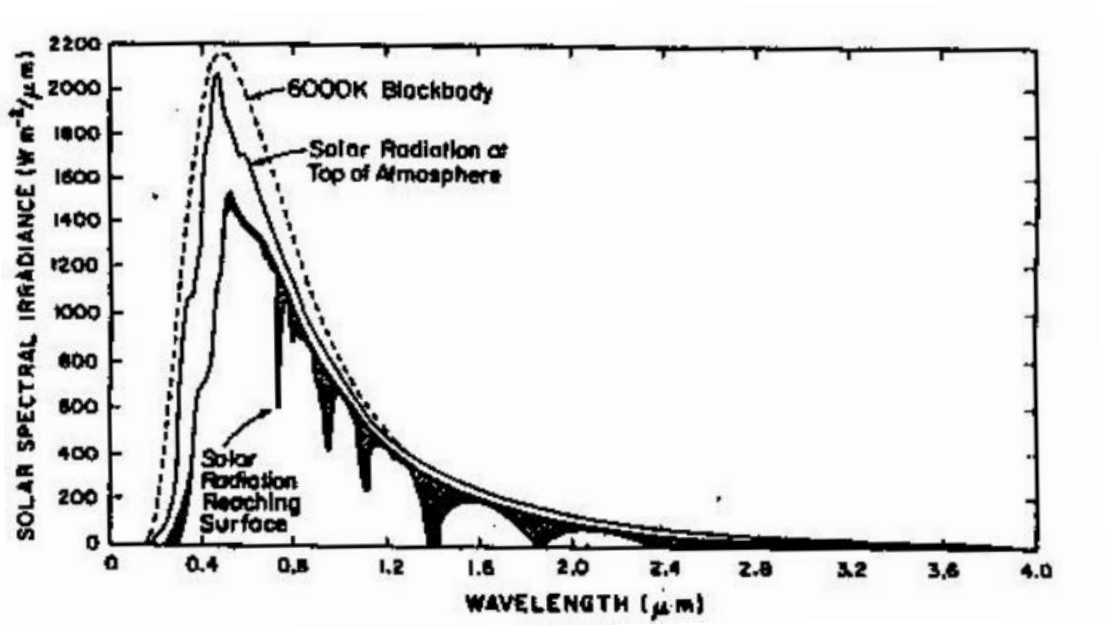

Figure 2.4: Spectrum of the solar radiation. The dashed line symbolises the unperturbed emission spectrum of a black body at 6000 K (approximate temperature of the Sun). Below the dashed line, the actual solar spectrum above the atmosphere is shown. The lower solid line shows the approximate solar spectrum on the Earth's surface after passing the Earth's atmosphere.(*Kidder and Vonder Haar*, 1995)

into other directions and (4) scattering into the beam. The shaded areas in Figure 2.4 represent the absorption due to gases in the atmosphere and the area between the spectrum above and below the atmosphere.

Absorption and emission from gases is very complex, but in general radiation interferes with gas molecules in five different ways: (1) electronic transitions, (2) vibrational transitions, (3) rotational transitions, (4) forbidden transitions and (5) ionisation-dissociation interaction (*Kidder and Vonder Haar*, 1995). The main components of the Earth's atmosphere are diatomic nitrogen (N_2) ($\sim 78\,\%$), diatomic oxygen (O_2) ($\sim 20\,\%$), water vapour (H_2O) ($\sim 1\,\%$, but highly variable) and argon (Ar) ($\sim 1\,\%$). However, mainly water (H_2O) and other gases, e.g. carbon monoxide (CO), methane (CH_4), nitrogen dioxide (N_2O), ozone (O_3), carbon dioxide (CO_2), and HDO (which is heavy water, where one hydrogen is replace with a deuterium atom), make the solar spectrum opaque (see Figure 2.5).

The scattering of radiation particles depends on several properties: the particle shape, the particle radius, the refractive index of the particle, the radiation wavelength and the viewing geometry. There are two different types of scattering based on the size of the scattering particle compared to the scattered radiation. Rayleigh scattering describes the interaction between small particles compared to the wavelength, e.g. air molecules or very small aerosols, below $0.1\,\mu$m. Mie scattering specifies the impact on the radiation of large particles (compared to the wavelength), e.g. dust particles, cloud and fog particles.

Problems in the detection and analysis as a result of the absorption lines using satellite

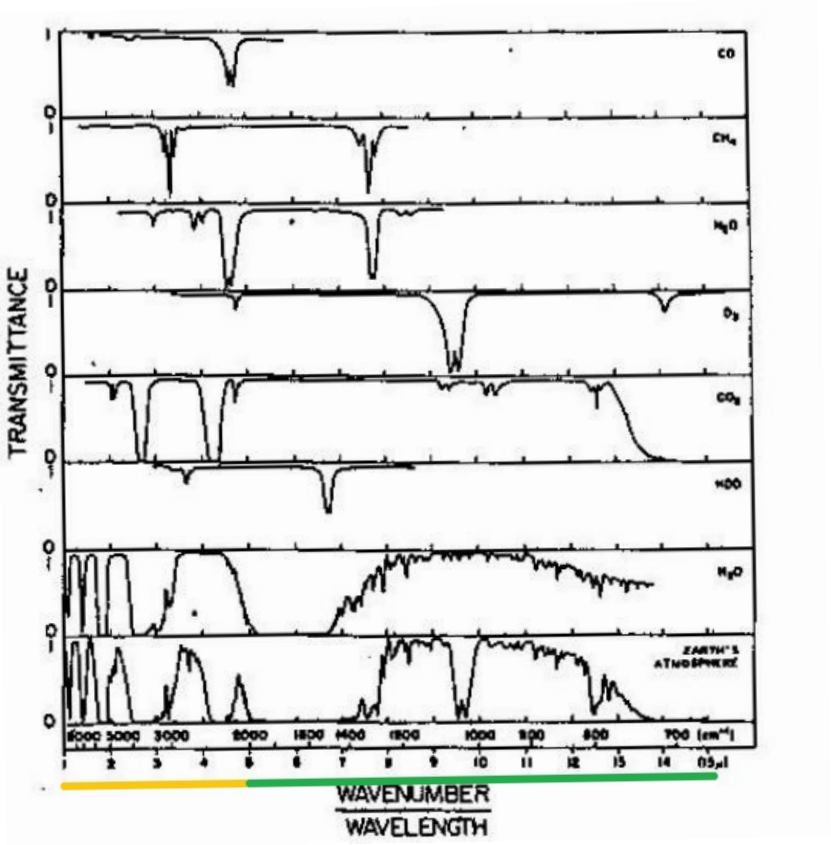

Figure 2.5: The main absorber of the solar radiation in the Earth's atmosphere. Shown are carbon monoxide CO, methane CH_4, nitrogen dioxide N_2O, ozone O_3, carbon dioxide CO_2, HDO, water vapour H_2O and the total atmospheric absorption spectra. The yellow bar underneath the graph indicates the range of the solar radiation, while the green bar represents the scale of the terrestrial radiation. (*Kidder and Vonder Haar*, 1995)

data can occur and the laboratory measurements and atmospheric transmission agree only within a 10 % error. The other limitation for most measurements is the limit in resolution. The radiative transfer is only valid in a very small microwindow, therefore, with a low resolution several lines are detected and cannot be separated. A high-resolution spectrum is necessary to get important information about the composition of atmospheric gases.

2.2. Volcanology

There have been about 380 active volcanoes in the last century and there are about 50 active volcanoes every year spread over the whole globe. This spread is linked to the actives zones of the tectonic plates, which are mainly located in the Northern Hemisphere and in the tropics, therefore, more than two thirds of the active volcanoes are located around the tropics and in the Northern Hemisphere. (*Textor et al.*, 2004)

2.2.1. Volcanic gas composition

The major gas phase component in a volcanic plume is water vapour, followed by CO_2 and SO_2 (see Table 1). Although water vapour is the most abundant component, the

global flux due to volcanoes compared to the natural global flux from evaporation from oceans or lakes is negligible. The global flux of CO_2 emitted by volcanoes of 20 Tg(C)/a (*Textor et al.*, 2004) compared to the anthropogenic emission of 8,000 Tg(C)/a (*Forster et al.*, 2007), is only a very small input of CO_2 to the atmosphere. The emission of sulphur due to volcanic eruptions is more significant and represents about 7 % of the total sulphate flux in the atmosphere. The main source of sulphate aerosol is caused by anthropogenic pollution from fossil fuel burning (approximately 72 %) and from the natural source production of dimethyl sulphide by phytoplankton (approximately 19 %) (*Forster et al.*, 2007). The impact and influence of volcanic SO_2 is very significant when the eruptions reach the stratosphere, due to a long lifetime of the sulphuric species and the change in chemical and physical processes in the stratosphere (*Jones et al.*, 2010). All the other main sulphate emitters only influence the troposphere, mostly in the planetary boundary layer.

Table 1: Typical composition of the main gaseous components of volcanic plumes at the vent, according to *Textor et al.* (2004).

Species	H_2O	CO_2	SO_2	H_2S	HCl	HF
Comp. [%/vol]	$50-90$	$1-40$	$1-25$	$1-10$	$1-10$	$>10^{-3}$
Global flux [Tg/a]	?	75	$1.5-50$	$1-2.8$	$0.4-11$	$0.06-6$

The majority of the aerosol after an eruption are ash particles and aqueous H_2SO_4, for example in the plume of the Mt. Pinatubo more than 90 % of the fine particles in collected samples were aqueous sulphuric acid (H_2SO_4) *Sheridan et al.* (1992). The ash particles are much larger and so their lifetime is usually not longer than a few weeks caused by their size and weight.

2.2.2. Aerosol size distribution

The physical and chemical properties of aerosols in the atmosphere are described by the aerosol size distribution, composition, and refractive indices (*Hansen and Travis*, 1974). The most common description of the aerosol size distribution is the unimodal log-normal distribution (*Pinnick et al.*, 1976):

$$\frac{dn(r)}{dr} = \frac{N_0}{\sqrt{2\pi}r\ln(\sigma)} exp\left(-\frac{\ln^2(r/r_g)}{2\ln^2(\sigma)}\right). \tag{1}$$

This function is semi-empirical and tries to describe the nature of the aerosol size distribution in a relatively simple mathematical equation, in a distribution shape of a bell curve with a maximum at the radius r_g. Where $dn(r)/dr$ represents the number of particles per unit radius interval, N_0 is the total number concentration, r_g is the median radius and σ is a shape parameter for aerosols, the so-called geometric standard deviation. The relationship between the aerosol extinction β at a specific wavelength and the aerosol size distribution can be described by the Mie theory:

$$\beta = \int_0^\infty Q(m,x)\pi r^2 \frac{dn(r)}{dr} dr \tag{2}$$

$Q(m,x)$ is the Mie extinction efficiency factor and depends on the refractive indices m and the size parameter $x = 2\pi r/\lambda$ (*Pinnick et al.*, 1980).

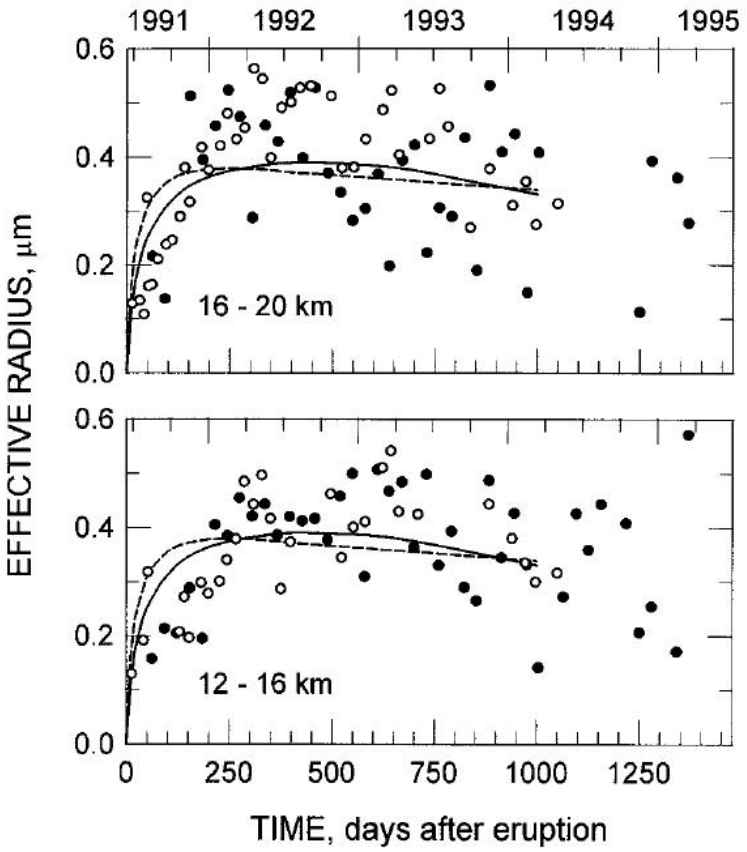

Figure 2.6: Monthly mean of the effective radius of sulphate aerosol after the eruptions of Mt. Pinatubo (15.07.1991). The lines indicate the evolution of the radius at an altitude of 17 km (solid lines) and 25 km (dashed lines). The circles show the actual measurements in Europe (black circles) and over Wyoming (open circles). (*Ansmann et al.*, 1997)

For the reason of minimizing the number of parameters for a reasonable and possible computational retrieval of aerosol size distribution parameter information, an effective radius R_{eff} can be defined with the total aerosol mixing ratio V and the total aerosol surface area density S. The effective radius R_{eff} is a first approximation of the size distribution, assuming a spherical aerosol particle. The following relationships can be applied for the effective radius R_{eff}:

$$V = \int_0^\infty \frac{4}{3}\pi r^2 \frac{dn}{dr} dr = \frac{4\pi N_0 r_g^3}{3} \exp\left(\frac{9\ln^2(\sigma)}{2}\right) \tag{3}$$

$$S = \int_0^\infty 4\pi r^2 \frac{dn}{dr} dr = 4\pi N_0 r_g^2 \exp(2\ln^2(\sigma)) \tag{4}$$

$$R_{eff} = \frac{3/4\pi V}{1/4\pi S} = r_g \exp\left(\frac{5}{2}\ln^2(\sigma)\right). \tag{5}$$

The aerosol size distribution of volcanic aerosol changes over time (*Ansmann et al.*, 1997; *Hofmann and Rosen*, 1983; *Massie et al.*, 1996; *Goodman et al.*, 1994). As shown in Figure 2.6, the effective radius R_{eff} of the aerosol particle start to grow due to condensation and coagulation. The lines indicate the evolution of the radius at an

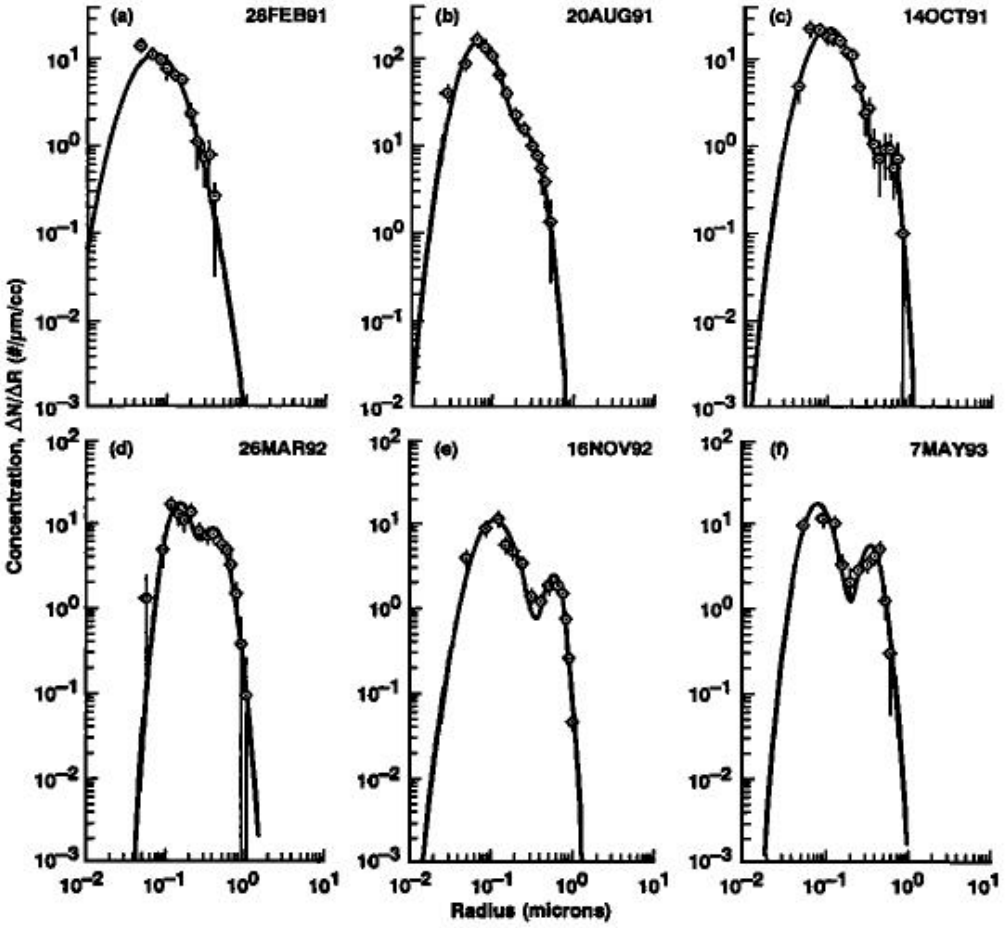

Figure 2.7: Evolution of the aerosol size distribution radius r_g after the eruptions of Mt. Pinatubo (15.07.1991). (a) is a typical background composition, (b)-(f) show the evolution of the aerosol. (*Goodman et al.*, 1994)

altitude of 17 km (solid lines) and 25 km (dashed lines), showing an increase for the first three months, followed by a stabilisation at $R_{eff} \approx 0.4\,\mu$m. The circles show the actual measurements in Europe (black circles) and over Wyoming (open circles). Both observations show the same trend of the effective radius R_{eff}. After a period of three months the growth is very slow because of the reduced amount of acid vapour (*Ansmann et al.*, 1997).

The evolution of the aerosol median radius r_g can be seen in Figure 2.7. While in Figure 2.7 (a) a typical background composition is shown, with a median radius of $r_g \approx 0.08\,\mu$m. After the volcanic eruptions on 15 June 1991, a second radius mode starts to grow over several weeks, as shown in Figure 2.7 (b) - (f). The typical background stratospheric aerosol size distribution is unimodal, while the volcanic aerosol size distribution becomes bimodal several months after the volcanic eruptions. Here the second radius mode can clearly be seen after approximately six months at $r_g \approx 0.4\,\mu$m. In the first few months after the eruptions the concentration of the aerosols is enhanced (about one order of magnitude after the Mt. Pinatubo eruption), but a second mode can barely be seen.

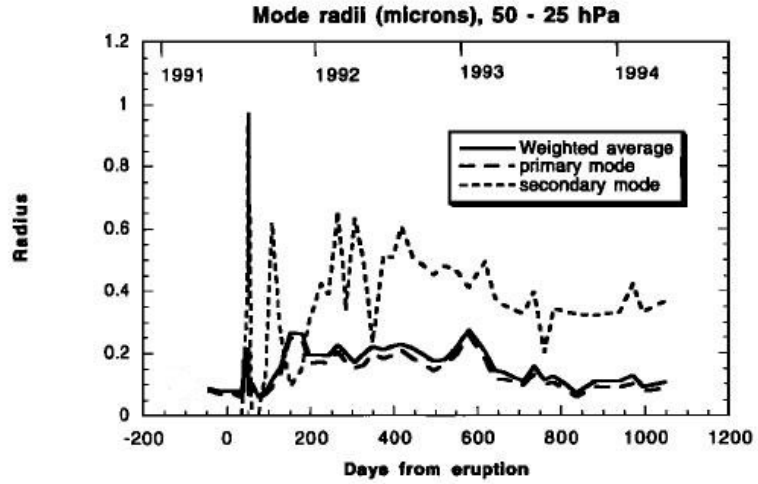

(a) Time evolution of the geometric standard deviation σ.

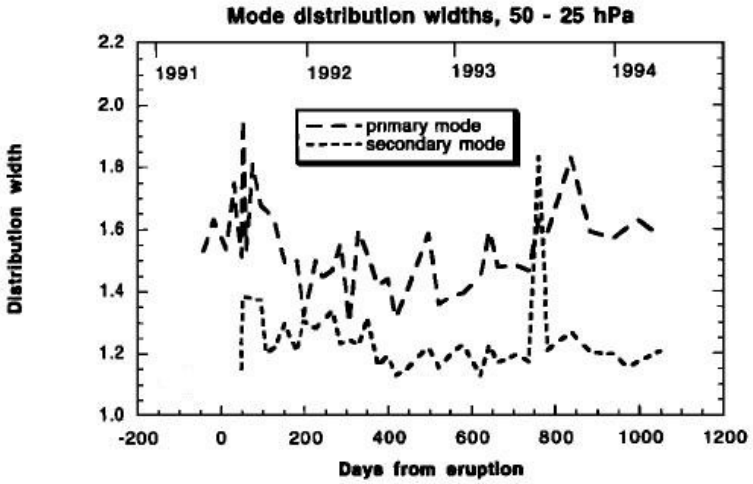

(b) Time evolution of the radius r_g.

Figure 2.8: Aerosol distribution parameter (σ and r_g) after the eruptions of the Mt. Pinatubo (15.07.1991), averaged over $50 - 25$ hPa for the primary and secondary mode. (*Massie et al.*, 1996)

In Figure 2.8 the evolution of the aerosol size distribution parameters r_g and σ is illustrated for the primary and secondary mode. In Figure 2.8 (a) the median radius r_g for the two different modes and the averaged radius can be seen. The average of the radius was weighted by the number density of the modes and therefore has a similar evolution as the radius of the primary mode. In Figure 2.8 (b) the evolution of the geometric standard deviation σ is shown; here the primary geometric standard deviation σ varies between 1.6 and 1.8, while the secondary σ is near 1.2 (*Massie et al.*, 1996).

For other volcanic eruptions, e.g. the eruptions of El Chichón (1982) a similar behaviour of the aerosol size distribution was observed by *Hofmann and Rosen* (1983).

For this thesis and the analysis of volcanic aerosol with satellite data, especially the stratospheric aerosol is important. The solution or composition of stratospheric aerosol is composed of aqueous sulphuric acid of $60 - 80\,\%$ (i.e. $60\,\%$ or $80\,\%$ sulphuric acid (H_2SO_4) and $40\,\%$ or $20\,\%$ water, respectively). (*Shen et al.*, 1995)

2.2.3. Influence on atmospheric chemistry and climate

Many reactive gases are abundant in volcanic plumes, *inter alia* sulphuric components and highly reactive halogen species which can have a great impact on the atmospheric chemistry (*Bobrowski et al.*, 2003).

The most important oxidant in the atmosphere is the hydroxyl radical (OH), because it is the so called detergent in the Earth's atmosphere, as it removes many gases, such as sulphates. The hydroxyl (OH) radical is formed, *inter alia* by photolysis of ozone (O_3) and the reaction of the excited oxygen (O) atom with water vapour (H_2O):

$$O_3 + h\nu \rightarrow O_2 + O \tag{6}$$

$$O\ (^1D) + H_2O \rightarrow 2\,OH \tag{7}$$

The oxidation of sulphur dioxide (SO_2) to sulphuric acid (H_2SO_4) is slow and can take several weeks (*Reiner and Arnold*, 1994). First, SO_2 reacts under tropospheric conditions with the OH radical:

$$SO_2 + OH + M \rightarrow HOSO_2 + M. \tag{8}$$

The regeneration of the HO_2 radical and SO_3 molecule is followed:

$$HOSO_2 + O_2 \rightarrow HO_2 + SO_3. \tag{9}$$

In the final step the sulphuric acid is generated in the presence of water vapour:

$$SO_3 + H_2O + M \rightarrow H_2SO_4 + M. \tag{10}$$

However, the sulphuric acid in the atmosphere also originates from aqueous oxidation of SO_2 by H_2O_2 in cloud droplets (*Reeves and Penkett*, 2003):

$$SO_2 + H_2O \rightleftharpoons H^+ + SO_2OH^- \tag{11}$$

$$SO_2OH^- + H_2O_2 \rightleftharpoons SO_2OOH^- + H_2O \tag{12}$$

$$SO_2OOH^- + H^+(HA) \rightarrow H_2SO_4 + (A^-) \tag{13}$$

$$\Rightarrow SO_2 + H_2O_2 \rightarrow H_2SO_4 \tag{14}$$

where HA is an acid molecule and A^- a base molecule. The reactions shown (8 - 14) are the main oxidation reactions for the removal of SO_2 and building of H_2SO_4 in the atmosphere. It is believed that $60 - 80\,\%$ are removed by the aqueous phase process (*Reeves and Penkett*, 2003).

The emission of sulphuric components can effect the radiation scattering of sun light or the climate due to the conversion to sulphuric acid. Because of the lifetime of several weeks, a volcanic eruption can have an influence over the whole hemisphere due to the median transport time of two weeks. The back-scattering of the solar radiation has a cooling effect to the Earth's surface temperature because less radiation can reach the Earth. After the volcanic eruptions of Mt. Pinatubo the Earth's global surface temperature was reduced by 0.4°C in the year after the eruptions, while at the same time the stratospheric temperature caused by absorption of aerosols was increased by approximately 1.5°C (*Parker et al.*, 1996). H_2SO_4 is an efficient cloud condensation nuclei (CCN), effecting the climate indirectly due to perturbation of clouds. The change of perturbed clouds compared to unperturbed clouds is described in Figure 2.9.

The illustration in Figure 2.9 shows the effect of aerosols on the climate. The direct effect describes the scattering of solar radiation (black arrows) on sulphate particles or other aerosols. Next, an unperturbed cloud is shown, while the white circles display the cloud condensation nuclei (CCN), the unperturbed CCN are larger with a lower concentration which means that the coalescence is reduced. This reduced coalescence leads to a reduced auto-conversion and less rain, and therefore the lifetime is potentially increased. Also, the perturbed CCN, which are smaller with a higher concentration, lead to a "whitening" of the cloud due to a stronger back-scattering of the solar radiation. Aerosol particle in the stratosphere can also affect ice and cirrus clouds. There is a higher probability of a cloud burn-off, the so called semi-direct effect, caused by the heating of the clouds absorbing solar radiation. (*Forster et al.*, 2007; *Haywood and Boucher*, 2000)

Figure 2.10 illustrates the time series of the total optical depth of volcanic aerosol in the visible at $0.55\,\mu$m. A very strong recent event can be seen in 1991, the eruption of Mount Pinatubo, which led to a change in the visible depth of almost 0.2. This eruption caused a change in the radiative forcing of about $-3\,\mathrm{W\,m^{-2}}$. (*Forster et al.*, 2007)

Apart from the influence of the radiative forcing, the sulphuric acid can lead to acid rain, which can have adverse or fatal effects on forests. The acid components can be deposited at ground level, representing a health hazard for humans and animals.

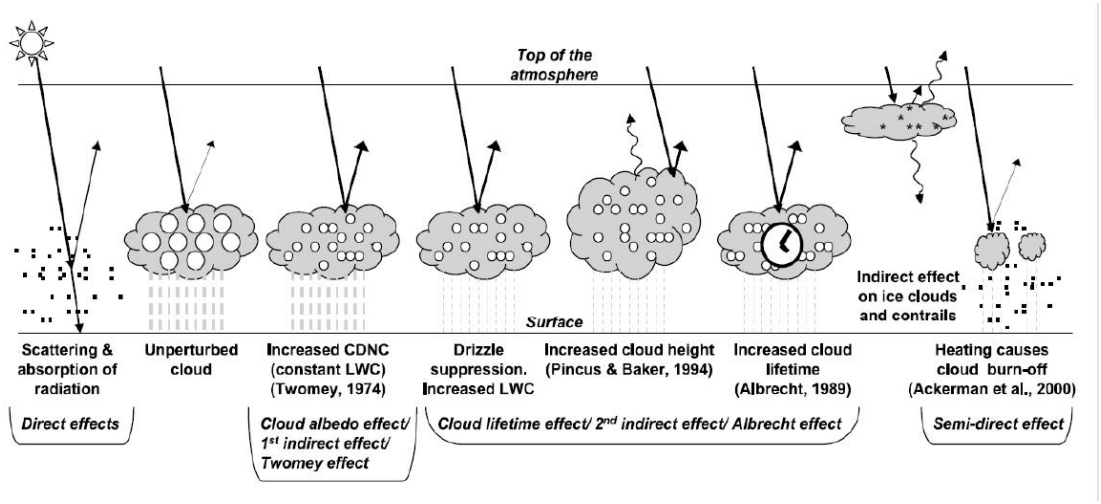

Figure 2.9: The illustration illustrates the effect of aerosols on clouds (indirect aerosol effect). The black dots represent aerosol particles, the straight black lines are the incoming and reflected solar radiation and the wavy lines represent the terrestrial radiation. The white circles display the cloud condensation nuclei (CCN), the unperturbed CCN are larger with a lower concentration, while the perturbed CCN are smaller with a higher concentration. (*Forster et al.*, 2007) after (*Haywood and Boucher*, 2000)

3. Atmospheric Chemistry Experiment (ACE)

The Atmospheric Chemistry Experiment (ACE) mission, also known as SCISAT, of the Canadian Space Agency (CSA) was launched on 12 August 2003 for a planned 2 year mission by the National Aeronautics and Space Administration (NASA). A picture of the satellite bus, built by Bristol Aerospace in Winnipeg can be seen in Figure 3.1. Due to an orbital inclination of 74° and a low circular Earth orbit (650 km), the satellite can cover tropical, mid-latitude and polar regions (*Bernath et al.*, 2005), but primarily focusses on good polar coverage. ACE retrieves the volume mixing ratio (VMR) of many species, as well as determining a temperature and pressure profile, between approximately $10-100$ km in a latitude range of 85°N and 85°S. ACE is equipped with three instruments with the four original science goals. These are (1) improving our understanding of polar ozone chemistry, (2) understanding the relationship between atmospheric chemistry and climate change, (3) the effect of biomass burning and (4) analysing the effect of aerosol and clouds for a better understanding of their influence on the global energy balance.

ACE takes observations by solar occultation technique at sunrise (sr) and sunset (ss) using primarily a high-resolution infrared Fourier transform spectrometer (FTS). ACE-FTS covers the $750-4400$ cm^{-1} spectral region with a resolution of 0.02 cm^{-1}. The satellite has a vertical resolution of about $3-4$ km as set by the field-of-view from the top of the clouds to 150 km. A large number of profiles of atmospheric trace gases (see `http://www.ace.uwaterloo.ca/`) as well as the meteorological variables of temperature and pressure, are determined by ACE-FTS. The near infrared and visible ($400-1030$ nm) spectrometer MAESTRO (Measurement of Aerosol Extinction in the Stratosphere and TRoposphere by Occultation) with a spectral resolution of $1-2$ nm, obtains profiles of atmospheric extinction, nitrogen dioxide and ozone (*Bernath et al.*, 2005; *McElroy et al.*, 2007). There are also two filtered imagers, which monitor clouds

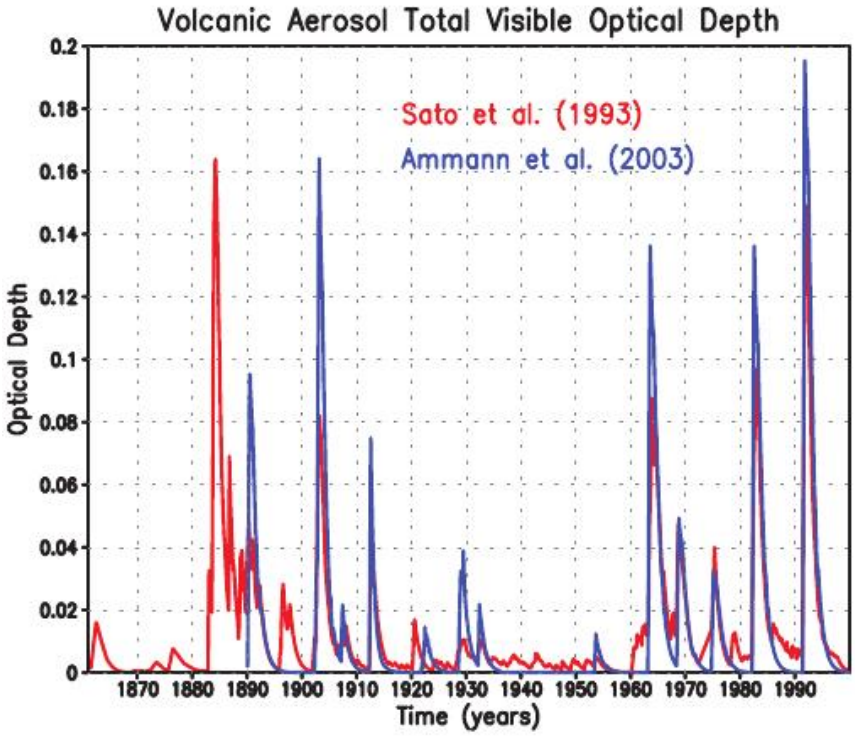

Figure 2.10: Time series of the total visible optical depth of volcanic aerosol (at 0.55 μm). (*Forster et al.*, 2007) and references therein

and aerosols by measuring atmospheric extinction in the visible region (VIS) at 525 nm and in the near-infrared region (NIR) at 1020 nm. These wavelength are chosen because for these wavelengths the spectrum is dominated by Rayleigh, aerosol and cloud scattering, and match two of the SAGE II imagers for a better comparison. (*Bernath et al.*, 2005).

The principle measurement technique for the detection of spectra is shown in Figure 3.2. In a limb viewing geometry at sunrise and sunset, several layers with different slant paths and tangent heights are almost contemporaneously scanned. The vertical concentration profile of atmospheric components can be estimated from the slant path through the different layers in the atmosphere. Exo-atmospheric measurements are taken for the purpose of reference spectra of the Sun (I_0), having the advantage of self-calibration of ACE instruments for the analysis of the transmission spectra (I/I_0). The first measurement is taken of the exo-atmosphere, the second measurement only shows absorption by the molecules of the first layer, the next layer contains information of the first and second layer, while the concentration in the first layer is already retrieved and the concentration in the second layer can be determined and so on.

The orbit of the satellite, which was selected so it repeats every year, can be seen in Figure 3.3. One line in Figure 3.3 represents the measurement during sunrise and the other during sunset. The measurements of the ACE satellite do not cover the whole globe at all times. There is a period in every year, in June (around day 175) and December (around day 350), when the satellite cannot take any measurements. For this period, because of the angle of the satellite to the Sun, the satellite orbits only in sunlight, therefore, sunrise and sunset measurements cannot be taken.

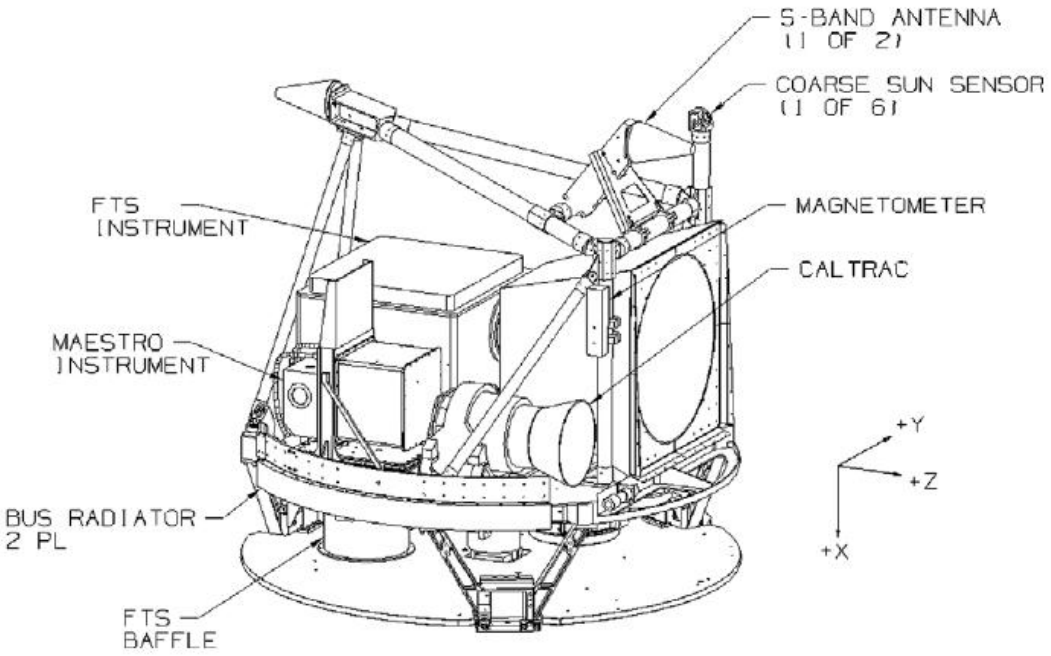

Figure 3.1: The ACE satellite with a diameter of about 1 m and a weight of 250 kg (*Bernath*, 2006).

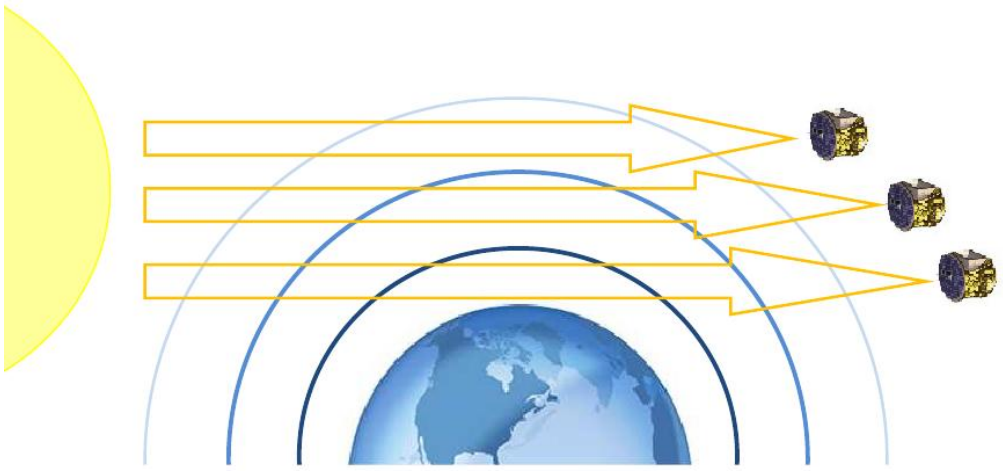

Figure 3.2: Illustration of the ACE profile measurement technique. By scanning layers of the atmosphere at approximately 1 km difference the profile of certain gases can be retrieved.

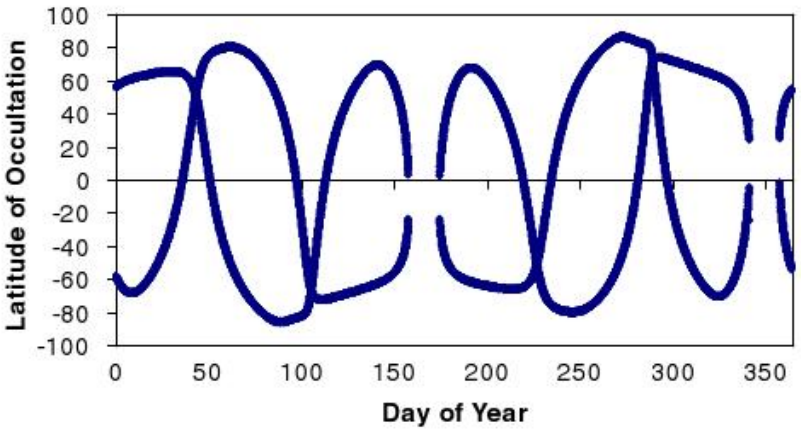

Figure 3.3: Cover of the latitudes from ACE in one year (*Bernath*, 2006).

3.1. Instrumentation

For this thesis the data from ACE-FTS and ACE-imagers have been used, therefore a more specific explanation of these instruments is provided in the following section.

3.1.1. Fourier transform spectrometer

The main instrument (ACE-FTS) on the ACE satellite is a Michelson interferometer. ACE-FTS as well as the imagers were built by ABB-Bomen in Quebec City, Canada with a mass of approximately 41 kg, an average power of 37 W and an achieved signal-to-noise ratio (SNR) better than 100 for some wavelength ranges (see Figure 3.5). A simplified illustration of the layout of the FTS is shown in Figure 3.4. Two photovoltaic detectors are used (InSb and HgCdTe) with a field of view (FOV) of 1.25 mrad. (*Bernath et al.*, 2005; *Bernath*, 2006; *Soucy et al.*, 2002)

The instrument has a suntracker (see Figure 3.4) ensuring a pointing view towards the Sun with an approximate stability better than 15 μrad. To assure the good resolution of 0.02 cm^{-1}, a very large optical path difference is needed, which is produced by the two corner-cube rotating mirrors and an "end" mirror to double pass the radiation. For a good SNR the detectors are cooled down and stabilised at a temperature between 60 and 80 K by a passive cryo-cooler pointing towards deep space, provided by Ball Aerospace (*Soucy et al.*, 2002). The photovoltaic detectors have an improved detector linearity compared to those from the ATMOS mission, giving the potential of detecting and analysing aerosols and clouds (*Boone et al.*, 2005).

Figure 3.5 shows the SNR over the wavenumber range for the ACE-FTS, which is not stable over all wavenumbers. The overlap between the two detectors can be seen in the sharp drop at 1810 cm^{-1}. At 3250 cm^{-1} is another drop of the SNR due to ice contamination. For high wavenumbers ($> 3000\,cm^{-1}$) the SNR is reduced caused by a problem with the beam-splitter transmission. (*Boone et al.*, 2005)

3.1.2. Imager

The two identical imagers on the ACE-satellite are centred (1) in the visible spectrum (VIS) at 527.11 nm with a full width half maximum (FWHM) of 13.28 nm and (2) in the near infrared spectrum (NIR) at 1020.55 nm with a FWHM bandwidth of 19.44 nm.

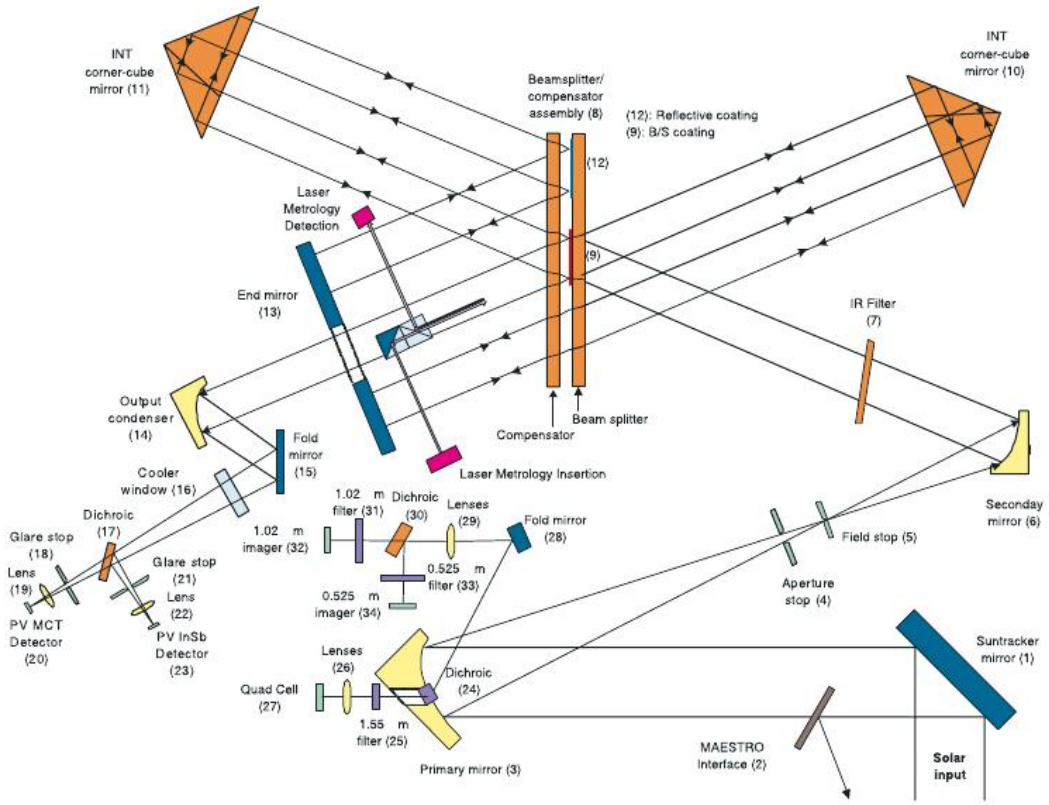

Figure 3.4: Schematic illustration of the ACE-FTS and imagers designed by ABB-Bomen (*Bernath et al.*, 2005).

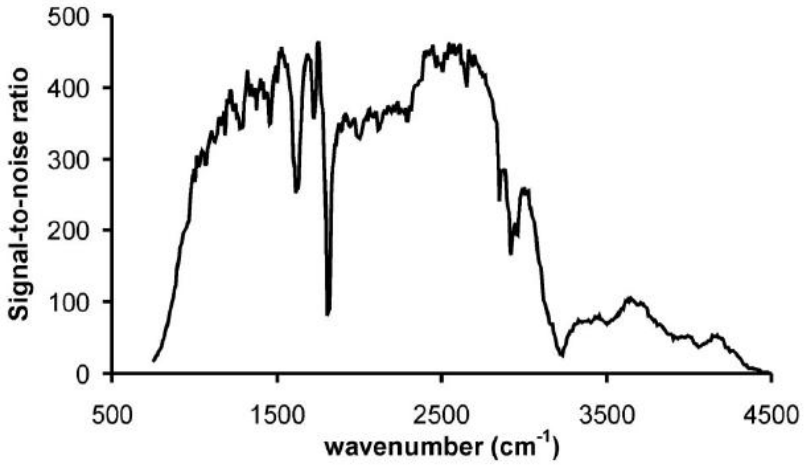

Figure 3.5: Signal-to-noise ratio for ACE-FTS as a function of the wavenumber. The overlap between the two detectors can be seen in the sharp drop at 1810 cm^{-1}. Another drop of the SNR can be seen at 3250 cm^{-1} due to ice contamination. (*Boone et al.*, 2005)

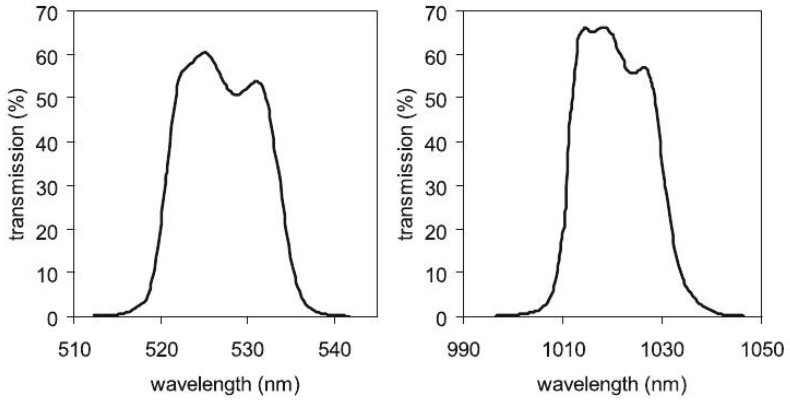

Figure 3.6: Illustration of the transmission as a function of the wavelength for the VIS-imager (left) and for the NIR-imager (right) (*Gilbert et al.*, 2007).

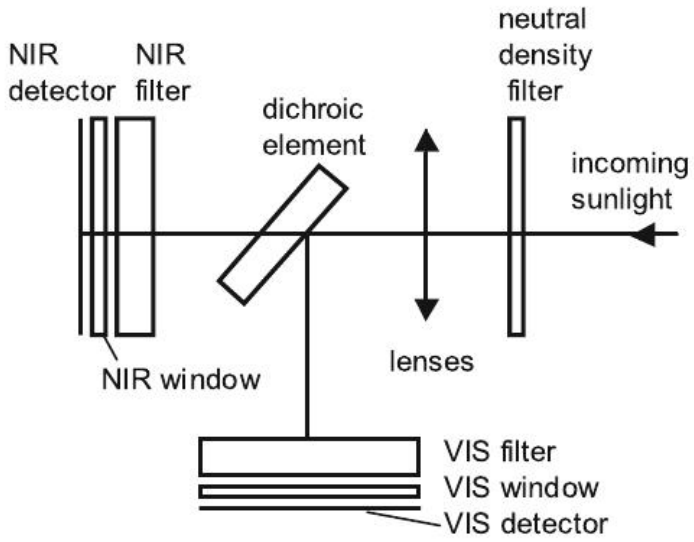

Figure 3.7: Schematic illustration of the built-up of the imagers on the ACE-satellite (*Gilbert et al.*, 2007).

The transmission of the imagers is shown in Figure 3.6. The centre of the wavelength were chosen to match two of the seven channels of the Stratospheric Aerosol and Gas Experiment (SAGE) II. (*Gilbert et al.*, 2007)

Figure 3.7 is an illustration of the schematic layout of the two identical imagers (except for the different wavelength filter) on ACE. The incoming light, after passing a number of lenses, is split up into two beams by a dichroic element. One beam is directed to the NIR and the other one to the VIS detector. Both of these detectors are made out of a complementary metal oxide semiconductor (CMOS) active pixel detector array by Fill Factory of Mechelen (Belgium) with a detecting area of 256×256 pixels. An effective image of 128×128 pixels is produced, while only about 64×64 pixels contain the image of the Sun, reducing the telemetry data. (*Gilbert et al.*, 2007)

3.2. Data retrieval, analysis and validation

The raw data from ACE are sent to two Canadian ground stations at St. Hubert (near Montreal, Quebec) and at Sakatoon (Saskatchewan), to an American station in Fairbanks (Alaska) and to a Swedish station in Kiruna (Sweden). ACE data are achieved and processed at the University of Waterloo (Ontario, Canada). On average 30 occultations are taken by ACE per day (24 h), this is a relatively low rate, resulting from the nature of solar occultation measurements. (*Bernath*, 2006)

3.2.1. ACE-FTS

To determine the VMR of a species, the temperature and pressure as a function of altitude is needed, which is determined from ACE-FTS data. The retrievals of the pressure and temperature profiles are separated into three different altitude regions, high altitude ($>$ 43 km), low altitudes ($>$12 km) and altitudes below 12 km. At high altitudes, the tangent height is calculated from geometry of the Sun, Earth and satellite. At low altitudes, a fixed CO_2 VMR is assumed between 10 km and 70 km. The relative CO_2 line intensity is used for the determination of the temperature, where as a first guess, meteorological data from the Canadian Meteorological Centre (CMC) are taken, and the pressure is retrieved with the absolute CO_2 line. The resulting temperature as a function of pressure can be converted into a function of altitude. Below 12 km, temperature and pressure are fixed to the meteorological data. The systematic error of the temperature is in general between $1-2\,\mathrm{K}$ and the systematic error for the pressure about $1-2\,\%$. (*Boone et al.*, 2005; *Bernath*, 2006)

For the retrieval of the VMR, small microwindows containing spectral features of the analysed molecule, are employed instead of the whole ACE spectrum. These microwindows are in general $0.3-1\,\mathrm{cm}^{-1}$ wide. Usually it is not possible to find such a microwindow without other molecules interfering, which will effect the VMR obtained. Therefore, more than one molecule feature can simultaneously be employed in the VMR retrieval, to avoid an inaccurate residuum with a wrongly determined VMR. The VMRs are determined simultaneously with a Levenberg-Marquardt non-linear least-squares algorithm. The retrieved errors of the VMRs are the statistical fitting errors from the least-squares process. This error does not contain any systematic errors from temperature, pressure, tangent height and spectroscopic data uncertainties. The spectroscopic data used for the retrievals are from the HITRAN 2004 (*Rothman et al.*, 2005) spectroscopic database and updates. The latest version is version 3.0 and is used for this study. (*Boone et al.*, 2005)

Validations of ACE-FTS retrieval of different molecules have been analysed in several publications in the past (see e.g. *Mahieu et al.* (2005); *Petelina et al.* (2005)).

3.2.2. ACE-imagers

The imagers on the ACE mission have three significant problems. (1) There is a linear increase in the response of the detectors from the operation of the detector itself. A correction is applied, but there is still the uncertainty of how accurate the correction is. (2) Due to reflections of the neutral density filter the images are overlapped by other images. (3) For unexplained reasons the NIR imager is out of focus. However, the retrieval of the extinction profile for the two ACE-imagers is possible and have been validated by *Vanhellemont et al.* (2008), by a comparison with the extinction profiles of GOMOS, SAGE II, SAGE III, POAM III and OSIRIS. The extinction profiles have

been found to be in good agreement, within a few percent, up to an altitude of 25 km (*Vanhellemont et al.*, 2008).

For the calculation of the extinction profile, all images are at first corrected for the dark current and the intensity increase of the detectors. 144 high Sun images are used to reproduce one high signal-to-noise reference image. This image is used as the reference image (I_0) for the transmission calculation. Then, only three pixels are analysed, centred on the co-registered ACE-FTS FOV. The transmittance (I/I_0) of each image is calculated and the results inverted in an extinction profile with an altitude grid of 1 km, while the tangent height for the analysis of the images is taken from the FTS measurements. For the spatial inversion into an actual extinction profile the same procedure as for the analysis of the FTS data is used. (*Gilbert et al.*, 2007; *Vanhellemont et al.*, 2008)

The data used in this study are the retrievals of version 2.2 because the data processing for version 3.0 is currently still in process. Validation of the extinction profiles processed with ACE imager data can be found in several publications, e.g. in *Vanhellemont et al.* (2008); *Sioris et al.* (2010).

4. Methodology

4.1. Sulphur dioxide

The VMRs of sulphur dioxide (SO_2) have been derived for the first time with the data of ACE-FTS in an altitude range between 12 km and 25 km. This altitude range of the retrievals covers the lower stratosphere and the upper troposphere. In this chapter the retrieval of the VMR, as well as the statistical and systematic error of the VMRs, are discussed because the retrievals of SO_2 are a research version which has not been validated. All the retrievals of the VMR of SO_2 have been made at the University of Waterloo (Ontario, Canada).

The SO_2 retrieval is a research version, based on the same global-fit with a Levenberg-Marquardt non-linear least-squares fitting algorithm used in ACE-FTS version 2.2 dataset (*Boone et al.*, 2005). The pressures and the temperatures used are from ACE-FTS version 3.0, while the spectroscopic data for SO_2 are from HITRAN 2004 (*Rothman et al.*, 2005). Four microwindows have been used to retrieve the SO_2 VMR: (1) centred at 1367.80 cm^{-1} with a width of 1.0 cm^{-1}, (2) centred at 1370.25 cm^{-1} with a width of 0.7 cm^{-1}, (3) centred at 1371.55 cm^{-1} with a width of 0.8 cm^{-1}, and (4) centred at 1376.30 cm^{-1} with a width of 0.6 cm^{-1}. Interferers in these microwindows are H_2O, $H_2{}^{18}O$, $H_2{}^{17}O$, HDO, CO_2, $CO^{18}O$, $CO^{17}O$, O_3, CH_4, $^{13}CH_4$, CH_3D, HCN, CH_3Cl and C_2H_2. In addition two microwindows without SO_2 information are employed, to improve the fitting results for two interferers (HDO and C_2H_2).

An example of an occultation spectrum (ss31868) with clear SO_2 signature is shown in Figure 4.1. The measured spectrum, the calculated contribution of SO_2 to the spectrum and the residuals in the calculated spectrum, both with and without SO_2 are shown to illustrate the presence of SO_2 in the spectrum. It can easily be seen that the residuals of the the retrieval without the SO_2 absorption bands included, shows the shape of the SO_2 calculated spectrum. When SO_2 is included in the calculation, the residuals improve from a deviation of approximately 25 % to a deviation of 5 %. This shows that the SO_2 VMR can be successfully retrieved by ACE-FTS, where the signature of SO_2 can be seen in the measured occultation due to the absorption spectrum and a significantly improved residuum.

The retrieved SO_2 concentrations are dominated by noise, meaning that the statistical error is larger or in the same magnitude as the derived concentration. As explained by *Boone et al.* (2005) the error of the retrieval results from two components; the statistical fitting error or random error, and a systematic error. The statistical error for the retrievals is, on average about 0.01 ppb and results from the statistical fitting error in the least-squares process in a Levenberg-Marquardt fitting algorithm (*Boone et al.*, 2005). The 1σ error of the variable x_j is defined as:

$$\sigma_m(x_j) = \sqrt{\left(\mathbf{K}^T \mathbf{S}_y^{-1} \mathbf{K}\right)^{-1}_{jj}} \tag{15}$$

where $\mathbf{K}$ is the Jacobian of the model and $\mathbf{S}_y$ is the diagonal covariance matrix of the measurements.

When concentrations are enhanced to about 0.1 ppb, the retrieval is reliable. The

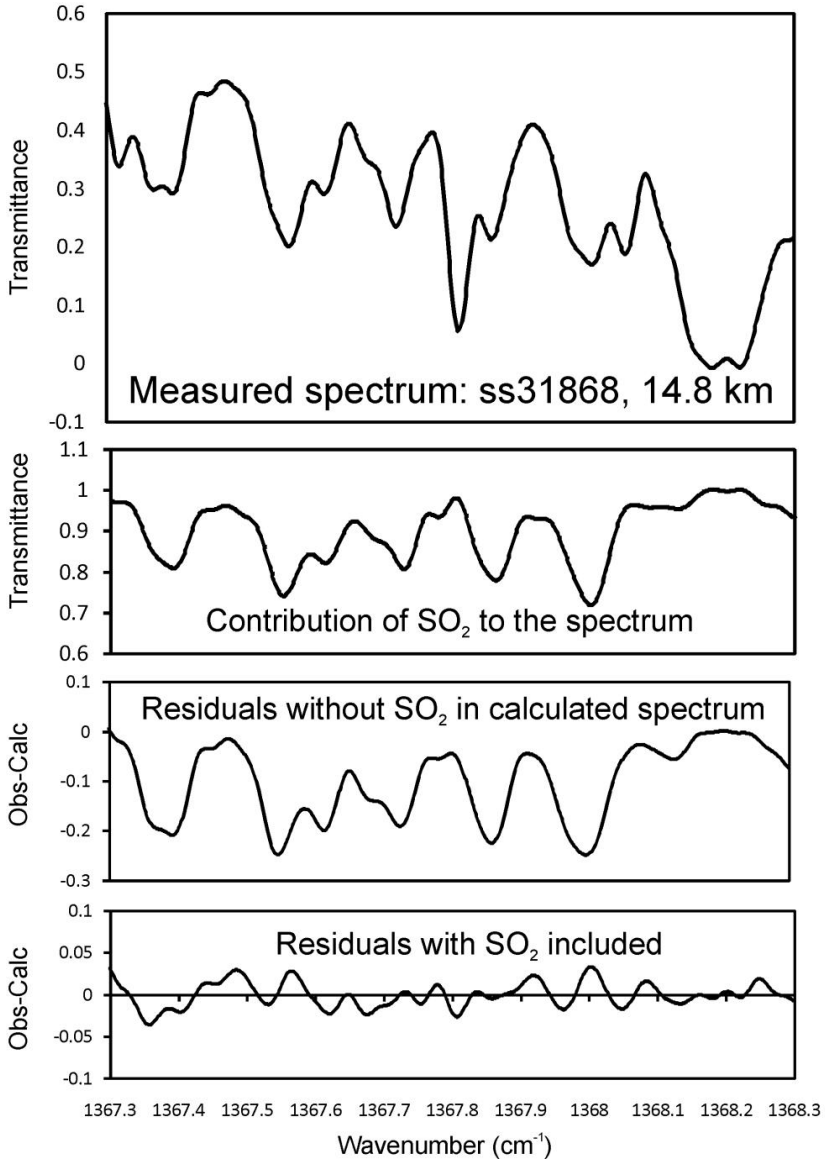

Figure 4.1: Illustration of an occultation spectrum (ss31868) with a clear SO_2 signature. The measured spectrum at 14.8 km (top panel), the contribution of SO_2 (second panel), the residuals without the contribution of SO_2 in the forward model (third panel) and the residuals with SO_2 included in the forward model (bottom panel) are displayed.

systematic error in the retrieval results from the uncertainties of relevant parameters in the fitting process. The effects of the error Δx_j on these parameters j has been analysed in a similar way to *González Abad et al.* (2011), using:

$$\Delta x_j = \sqrt{|x(b_j) - x(b_j + \Delta b_j)|^2}. \tag{16}$$

The whole systematic error can be calculated by summation over all the single uncertainties j, using:

$$\Delta x_{syst} = \sqrt{\sum_j |x(b_j) - x(b_j + \Delta b_j)|^2}. \tag{17}$$

The systematic error Δx_{syst} in the VMR is calculated as the difference of the unperturbed $x(b_j)$ and perturbed $x(b_j + \Delta b_j)$ retrieved VMR. Each parameter (b_j) is perturbed using 1σ of its assumed uncertainty (Δb_j). The relevant parameters b_j (and their 1σ uncertainty) were considered to be the temperature (2 K), the tangent height (150 m), the instrumental line shape ILS (5 % of field of view) (*Dufour et al.*, 2009), the uncertainties of the spectroscopic data (15 % for SO_2) (*Rothman et al.*, 2005) and the mixing ratio of the main interferes H_2O (10 %), CO_2 (1 %), CH_4 (5 %) and O_3 (5 %) (*McHugh et al.*, 2005).

For the analysis of the systematic error of the SO_2 retrieval, 15 occultations with a clear SO_2 signature of at least 1 ppb have been selected from July 2009. These occultations are namely ss31679, ss31741, ss31752, ss31769, ss31781, ss31798, ss31827, ss31839, ss31868, ss31903, ss31960, ss31976, ss32018, ss32041 and ss32116. Figure 4.2 (a) and (b) show the error resulting from the uncertainty of different parameters and the statistical error. In Figure 4.2 (a), the mean VMR of SO_2 (black) is plotted with the systematic and statistical errors. The retrieval has a high sensitivity to the uncertainty of the tangent height, resulting in a more significant error, about 0.1 ppb at a VMR of 1 ppb, than the statistical error. The uncertainty of the other parameters does not influence the systematic error considerably. The relative error is shown in Figure 4.2 (b), where the error due to the uncertainty of the tangent height results in a systematic error between 5 % and 10 % relative to the VMR of SO_2 at an altitude, where a clear signal of SO_2 is present (between 12.5 km and 17.5 km). The statistical error for VMR is about 0.01 ppb, resulting in approximately 1 % of the VMR (between 12.5 km and 17.5 km) because of the very low atmospheric concentration above 18 km the relative errors increase sharply above this altitude.

Because the systematic error due to the uncertainty in the tangent height is about 0.1 ppb the analysis has been repeated for occultations with a maximum SO_2 concentration of 0.5 ppb, to observe if these measurements are still reliable. For this observation 9 occultations from July 2009 have been used, namely ss31897, ss31912, ss31932, ss31941, ss31957, ss32030, ss32040, ss32059 and ss32109. The results of this analysis can be seen in Figure 4.3. Again, in Figure 4.3 (a) the mean SO_2 VMR (black) is plotted with the errors in the unit of "ppb", showing a relatively small systematic and statistical error. The size of the errors becomes clearer in Figure 4.3 (b), where the errors are plotted relative to the mean VMR. Here, it can be seen that the statistical and the systematic error almost have the same influence. The error resulting from the uncertainty of the tangent height is between 5 % and 25 % of the actual VMR retrieval at the height of the plume – between 15 and 20 km. The maximum error for these retrievals would be a combination of the statistical and systematic error, resulting in

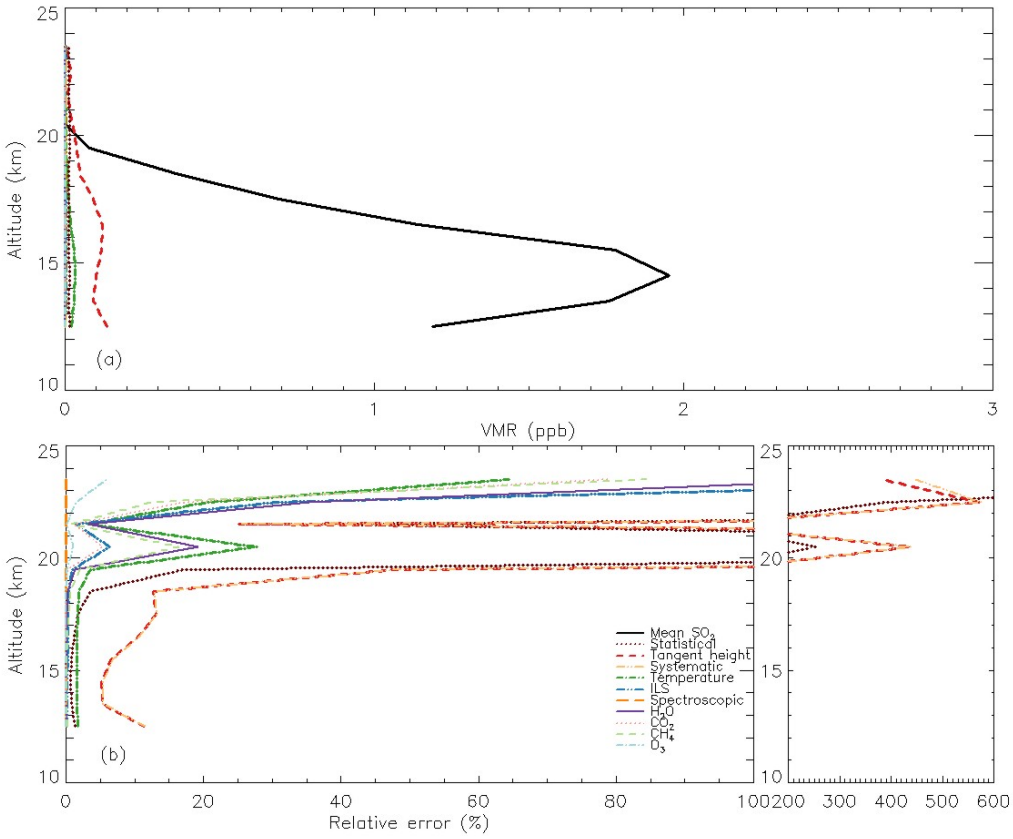

Figure 4.2: The mean error of 15 selected occultations in July 2009 due to the uncertainty of different parameters and the statistical error is shown. The top panel illustrates the error (ppb) in comparison to the VMR of the retrieval (black line) and the lower panel displays the errors relative to the VMR. The retrieval shows a high sensitivity to the uncertainty of the tangent height, resulting in a greater error than the statistical error. The systematic error, dominated by the uncertainty of the tangent height is about 0.1 ppb and, therefore, is between 5 % and 10 % of the VMR of SO_2 (between 12.5 km and 17.5 km). The uncertainty in the other parameters does not have a significant influence on the systematic error.

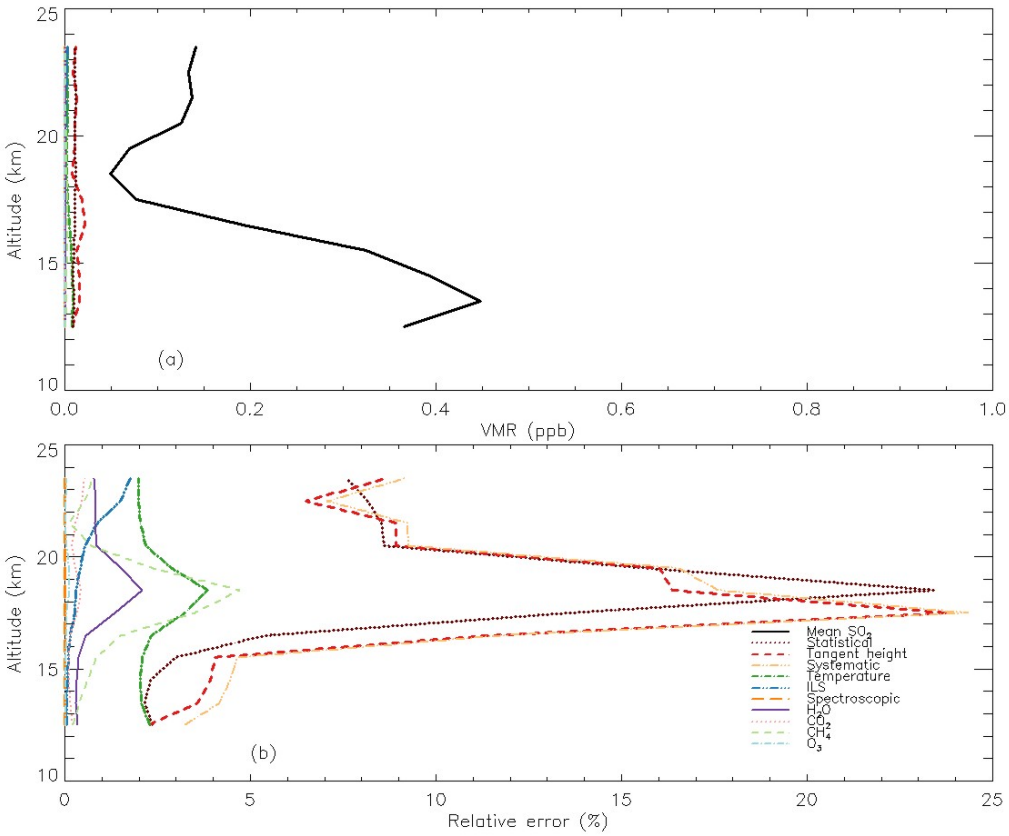

Figure 4.3: The mean error of 9 selected occultations in July 2009 with SO_2 concentrations of about 0.1 ppb caused by the uncertainty of different parameters and the statistical error is shown. The top panel illustrates the error (ppb) in comparison to the VMR of the retrieval (black line) and the lower panel displays the errors relative to the VMR. The retrieval shows a high sensitivity to the uncertainty of the tangent height, resulting in an error as significant as the statistical error. The systematic error, dominated by the uncertainty of the tangent height is about 0.01 ppb and, therefore, is between 5 % and 25 % of the VMR of SO_2 (between 12.5 km and 17.5 km). The uncertainty in the other parameters does not have a strong influence on the systematic error.

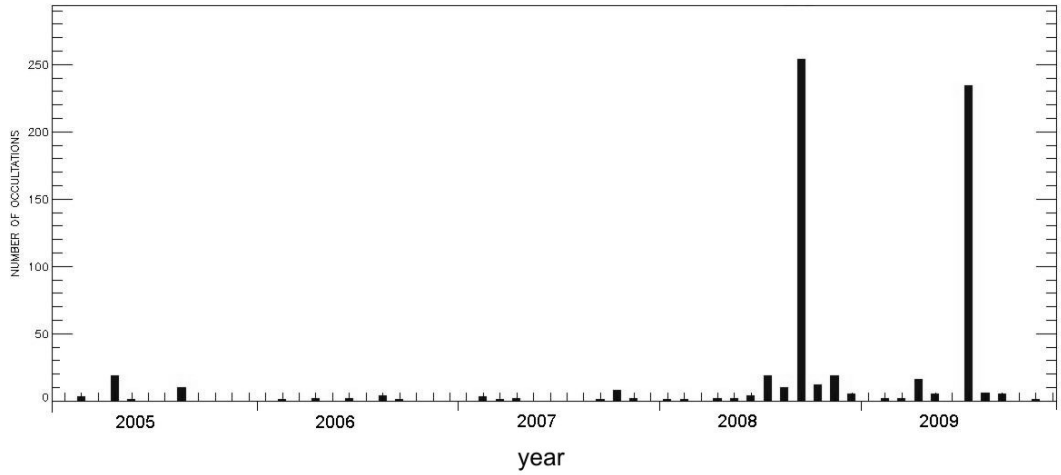

Figure 4.4: Number of occultations with a maximum SO_2 concentration $\geq$ 0.1 ppb between 2005 and 2009 from ACE-FTS data.

$\Delta x_{err} = \sqrt{\Delta x_{stat}^2 + \Delta x_{sys}^2} \approx 35\,\%$. Therefore, SO_2 VMRs of about 0.1 ppb can still be measured reliably, even when the systematic error is taken into account.

As SO_2 in the stratosphere is a clear indicator for volcanic plumes, in this thesis, measurable sulphur dioxide concentrations are used as a verification of the existence of volcanic presence in occultations. Figure 4.4 shows the number of occultations with reliable and measurable SO_2 concentrations from the beginning of 2005 to the end of 2009. It can be seen that ACE-FTS observes a large amount of reliable and enhanced SO_2 concentrations ($\geq$ 0.1 ppb, with an approximate error of 0.035 ppb) after a major volcanic event. Accordingly, sulphur dioxide was measured in 2008 after the eruptions of Kasatochi (August 2008) and in 2009 after the eruptions of Sarychev (July 2009). In further analysis it can be seen that occultations with an SO_2 concentration of $\geq$ 1 ppb only occur in September 2008 and July 2009, i.e. only in the month after a major volcanic eruption.

4.2. Atmospheric extinction

A peak in the SO_2 concentration only occurs for a few months after the eruptions, and as such for older volcanic plumes a different method to locate those plumes must be applied. Atmospheric extinction can be used to locate volcanic plumes, for several months after the eruptions of a volcano.

Atmospheric extinction is a term to describe the loss of solar radiation due to scattering and absorption in units of m^{-1}. The extinction coefficient b_{ext} is applied in the Lambert-Beer law, describing radiation through an absorbing and scattering medium:

$$I_\lambda(z) = I_{\lambda,0} \cdot exp(-b_{\lambda,ext} z), \tag{18}$$

while the I_λ describes the wavelength dependent intensity after passing a path of length z with an initial intensity I_0. The modelled extinction β_{model} (lognormal) of a sulphuric acid particle with a radius $r_g = 0.08\,\mu$m and a geometric standard deviation of $\sigma = 1.8$, is shown as a function of the wavenumber in Figure 4.5. The optical depth τ is the integral of atmospheric extinction b_{ext} over the path (here altitude):

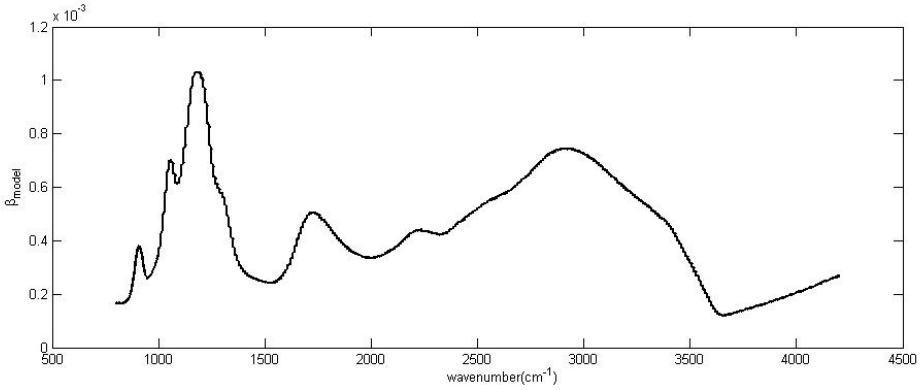

Figure 4.5: Modelled extinction β_{model} ($10^{12}\mathrm{km}^{-1}$), as a function of the wavenumber (cm^{-1}), for a sulphuric acid aerosol with a radius $r_g = 0.08\,\mu$m, a geometric standard deviation $\sigma = 1.8$ and a composition of 75 % sulphuric acid-water solution.

$$\tau_\lambda = \int_z b_{\lambda,ext}(z)\,dz. \tag{19}$$

The Angström exponent α describes the relation between the optical thickness τ_λ and the wavelength λ:

$$\frac{\tau_{lambda,1}}{\tau_{\lambda,2}} = \left(\frac{\lambda_1}{\lambda_2}\right)^{-\alpha} \tag{20}$$

The Angström exponent is related to the size of the particles, the larger the particles, the smaller the exponent α.

The atmospheric extinctions reported in this study are the standard version 2.2, derived from the imager data in the NIR or VIS region. The optical depth τ is the integral of the extinction b_{ext} over the path (see Equation 19). Because the major absorption and scattering takes place in the lower atmosphere, the upper limit of the integral was chosen to be 25.5 km and the lower limit 5.5 km, connected to the detective limit of ACE-imagers. For the determination of the clouds' height, a "clear-sky" profile has to be retrieved to discriminate between clouds or volcanic plumes and background aerosol. The method used in this study is based on the method from *Fromm et al.* (2003) and *Sioris et al.* (2010). First, the data from ACE-imagers are separated by each month and "clear" sky profiles are derived for each month individually. For a "clear" sky the atmospheric extinction increases monotonically. These monotonically increasing profiles below an altitude of 30 km are separated for each month and the median and standard deviation is determined at each altitude of those "clear" sky profiles. If any of these "clear" extinctions is now greater than the median $+4\sigma$, this occultation is filtered out and a new median and standard deviation is derived, until no occultation lies outside the 4σ limit. Clouds (in all occultations of the month) are reliably present when the profile extinction is higher than the median $+\,4\sigma$ of the "clear" sky profile for that month. If this cloud profile is above the tropopause, it can be assumed that it has volcanic origin because water vapour is not present (or very low) in the stratosphere. Figure 4.6 shows the cloud free global median atmospheric extinction at a wavelength of 1020 nm, derived from ACE-imager with the method described above. Enhanced atmospheric extinctions in February (2007 and 2008) and August (2004, 2006 and 2008) between 17.5 km and 18.5 km are caused by thin cirrus clouds and PSCs near the

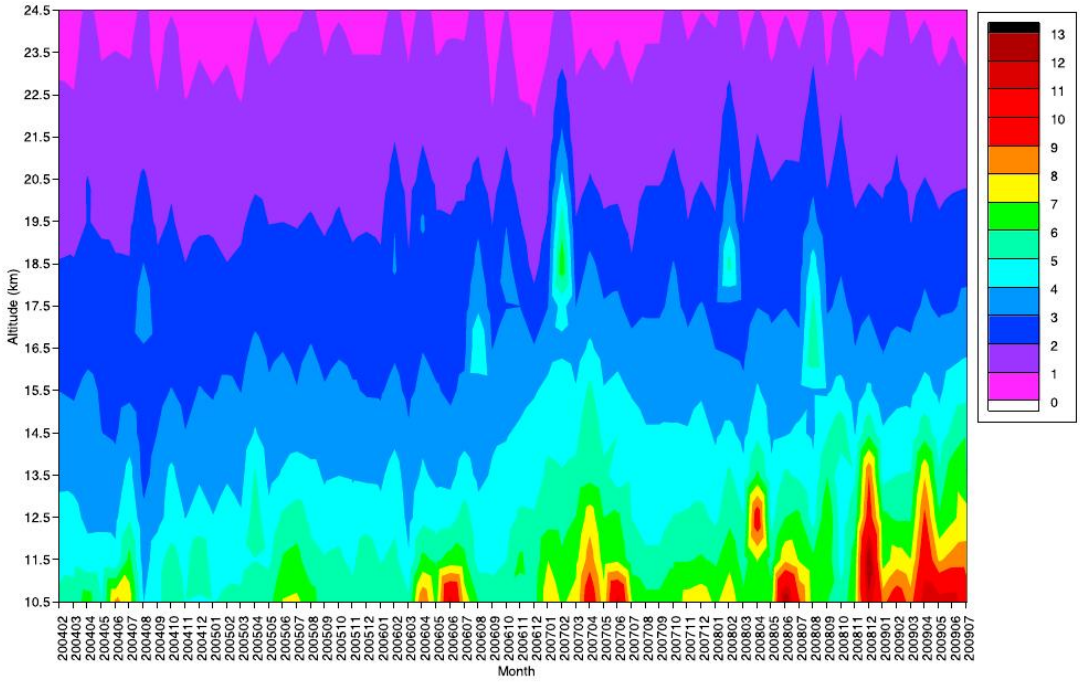

Figure 4.6: Cloud-free global median of atmospheric extinction ($\times 10^{-4}\,\mathrm{km}^{-1}$) at 1020 nm between 2004 and 2009 for each month (YYYYMM), derived from ACE-imager data. PSCs and thin cirrus clouds are not exactly filtered, leading to an enhanced atmospheric extinction in February and August between $17.5 - 18.5\,\mathrm{km}$. (*Sioris et al.*, 2010)

tropopause, which are not perfectly filtered. It is not possible to derive a monthly median profile throughout the year in a specific latitude range due to the limited spatial sampling of ACE. (*Sioris et al.*, 2010)

Figure 4.7 shows the median, the average and the standard deviation of atmospheric extinction for (a) 1020 nm (NIR) and (b) 530 nm (VIS) in July 2009 (one month after the Sarychev eruption). The solid lines show these values for the filtered "clear-sky" profiles and the dashed lines represent the values for the whole detected occultations. Significant differences can be seen in the average (mean) and standard deviation (SD) between the "clear-sky" profiles and all occultations. These differences, caused by a few very high or low VMRs, do not input upon the median significantly, despite considerably influencing the mean. The standard deviation is also very sensitive towards these high or low VMR values. A high influence of single odd occultations is bad for an analysis like this because various retrievals can fail and give very large or negative VMRs. By calculating the median, the value is more stable and a few failed retrievals do not have a considerable influence on the value. For high altitudes, above 20 km, the median and standard deviation is very close to $0\,\mathrm{km}^{-1}$. For various occultations showing an enhancement at higher altitudes, where small anomalies are possibly outside the 4σ limit, where no plumes or clouds are actually present.

July 2009 was only one month after the volcanic eruptions of Sarychev, therefore, the average value of all occultations should be significantly greater than the average of the monotonic profiles. This can clearly be seen for the NIR observations in Figure 4.7,

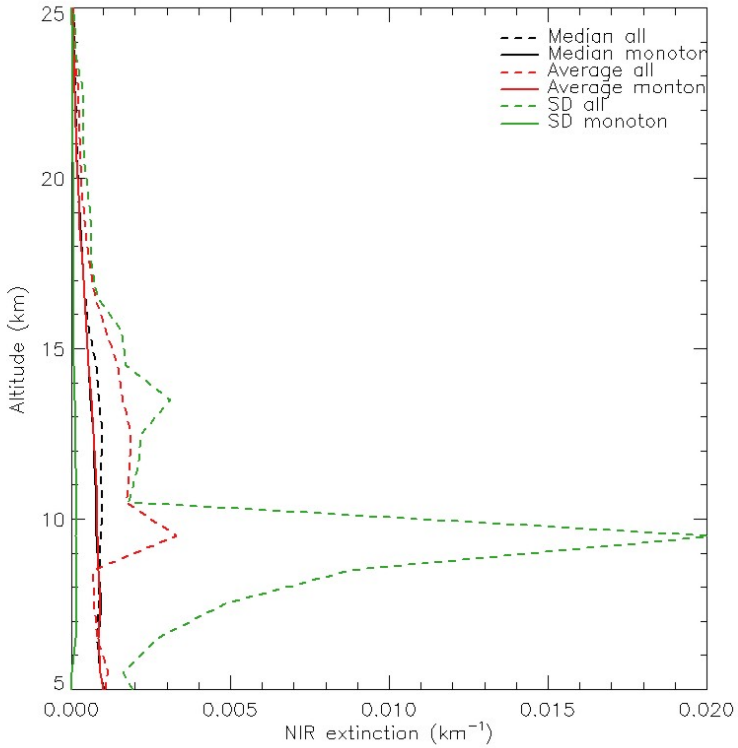

(a) Atmospheric extinction NIR

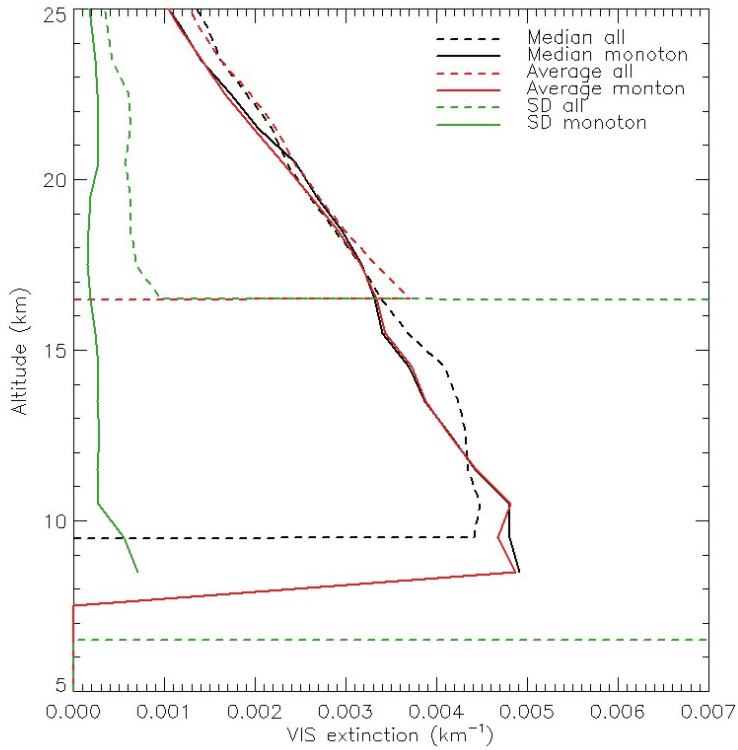

(b) Atmospheric extinction VIS

Figure 4.7: Atmospheric extinction for NIR and VIS in July 2009. Shown is the median, the average and the standard deviation (SD) for all occultations (dashed lines) of the month and for the filtered "clear-sky", monotone occultations (solid lines).

but only a small difference can be seen for the VIS (Figure 4.7) observations (above 16 km). The imager data at 1020 nm (NIR) appear to be more suitable for observation of volcanic aerosols. It is also recommended by *Vanhellemont et al.* (2008) to use the NIR atmospheric extinction because of optical problems of the VIS imager.

In version 3.0 of the retrieval of the extinction from ACE-imagers, an aerosol extinction is calculated in addition to the atmospheric extinction, which does not include the absorption due to atmospheric trace gases. A comparison between atmospheric and aerosol extinction can be seen in Figure 4.8. Atmospheric and aerosol extinctions (v.3.0) are displayed for a random occultation (sr27216), with volcanic influence from the eruptions of Kasatochi. The solid lines represent atmospheric extinction and the dashed lines show aerosol extinction, without the influence of trace gases. Red indicates the retrieval for the NIR-imager and blue the retrieval for the VIS-imager. The retrievals for the NIR-imager do not show a significant difference between atmospheric and aerosol extinctions, compared to the actual extinction values, including the absorption from trace gases. For the retrievals for the VIS-imager, a considerable difference can be seen between atmospheric and aerosol extinction of about $0.002\,\mathrm{km}^{-1}$, which equates to about $30-50\,\%$ of the atmospheric extinction. The region of 530 nm is a lot more disturbed by the absorption of trace gases and Rayleigh scattering, than the NIR region at 1020 nm. As a consequence of this interference, the signal of the VIS-imager is often cut-off at low altitudes of the troposphere or lower stratosphere. The accuracy of the calculation of the aerosol extinction is unknown, therefore an analysis of volcanic plumes with the the retrievals of the NIR-imager is more reliable.

In Figure 4.9 (a) and (b) the location of the enhanced atmospheric extinctions (NIR, v.2.2) and the height of the enhancement is shown, indicated by a colour scheme. Usually, one occultation does not just have enhanced atmospheric extinction at one altitude, therefore, Figure 4.9 shows the lowest altitude with enhancement above the tropopause. For high altitudes the median atmospheric extinction and the standard deviation is quite low, it is easy to measure enhanced extinction without a plume being present. Figure 4.9 (a) shows the enhanced atmospheric extinctions between October 2008 and March 2009, after the eruptions of Kasatochi, August 2008 and in Figure 4.9 (b) between September 2009 and February 2010. For these months, as shown in Figure 4.4, SO_2 concentration is too low for a detection by ACE-FTS, however, evidence of the presence of the volcanic plume can still be shown with enhanced atmospheric extinctions. High concentrations of occultations with enhanced atmospheric extinctions can be seen in both cases between 60°N and 70°N, in the latitude range, where the volcanoes are located.

This method, however, is not as exact as the localisation with high SO_2 concentrations because it is not possible to distinguish between a high extinction caused by water vapour or volcanic ash, aerosol particles and gases. As shown in Figure 4.9, there are occultations with enhanced SO_2 detected in the Southern Hemisphere (SH), but the volcanic plume cannot reach the SH a few months after the eruptions. The mean transport time between SH and NH accounts for approximately one year. Furthermore, it can be seen that for every occultation, in September 2008 and July 2009, with a heightened SO_2 concentration the atmospheric extinction was enhanced, but for every atmospheric extinction enhancement, the SO_2 concentration was not necessarily increased.

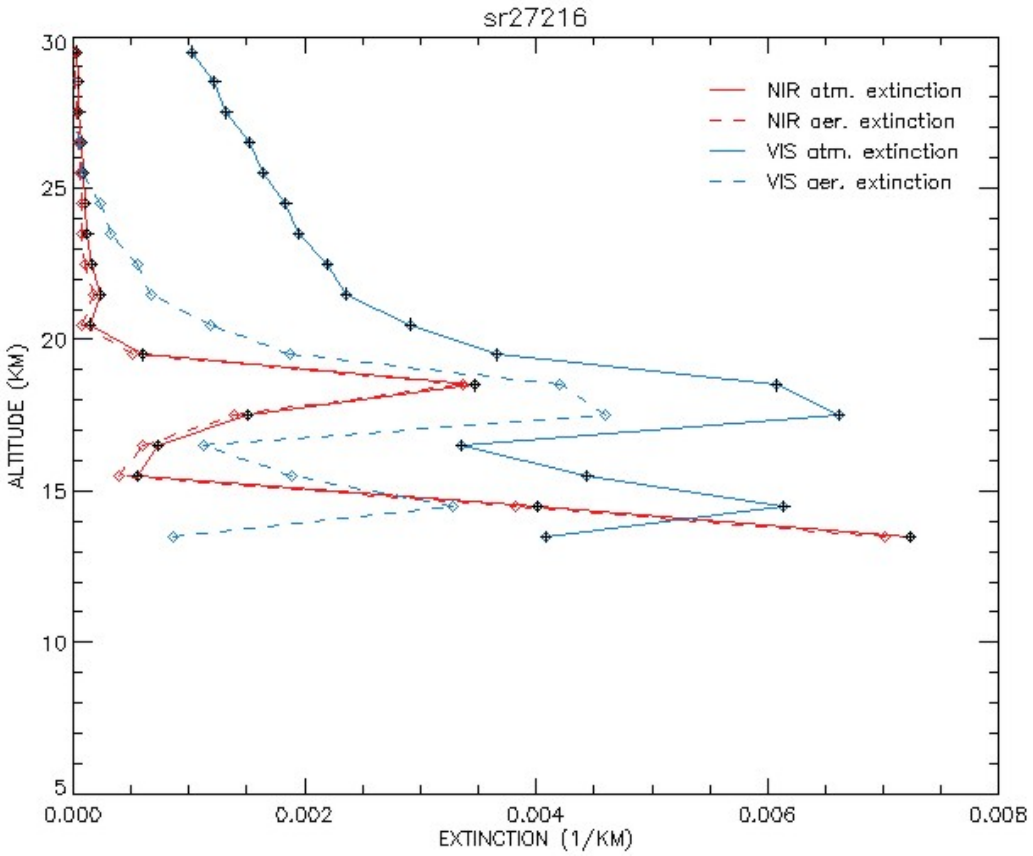

Figure 4.8: Atmospheric and aerosol extinction (v.3.0) for a random occultation (sr27216), with volcanic influence from Kasatochi's eruptions. The solid lines represent the atmospheric extinction and the dashed lines show the aerosol extinction, without the influence of trace gases. The red lines indicate the retrieval for the NIR imager, while the blue lines represent the retrievals of the VIS imager.

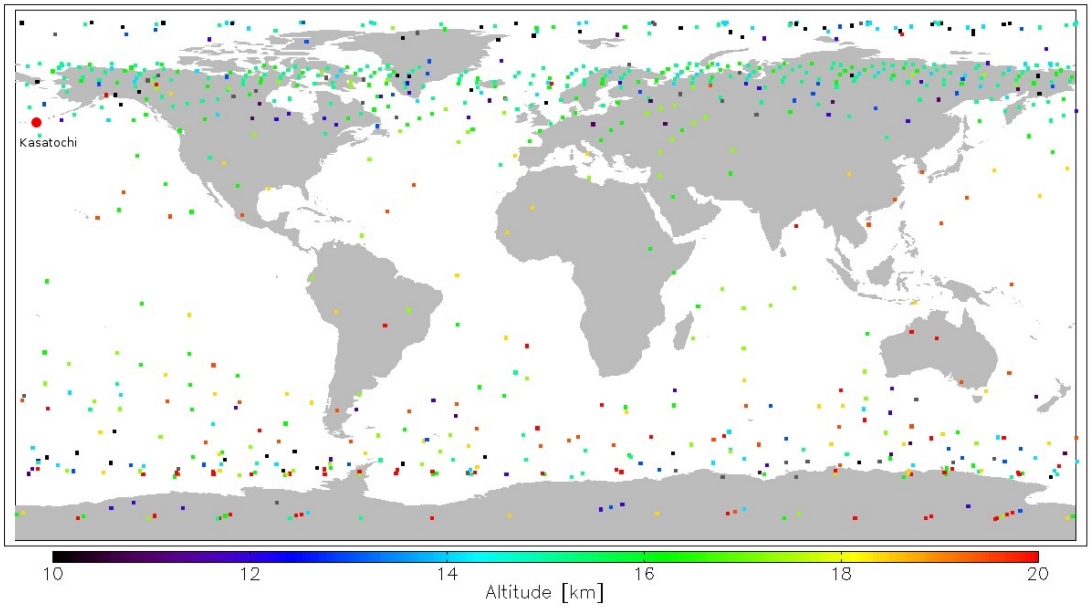

(a) Measurements between October 2008 and March 2009

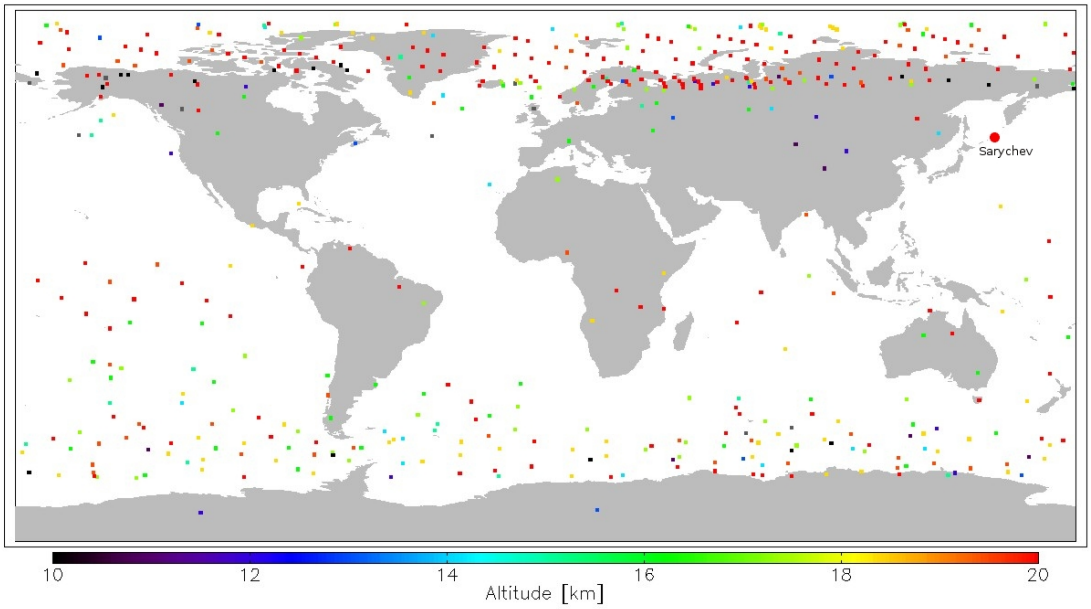

(b) Measurements between September 2009 and February 2010

Figure 4.9: Location of measurements of enhanced atmospheric extinction (NIR) v.2.2 above the tropopause. The colour scheme represents the lowest height (above the tropopause) of the enhancement. The large red dot displays the location of the volcanoes.

4.3. Aerosol properties

4.3.1. Fitting procedure

In order to derive aerosol properties from ACE-FTS spectra, "continuum" spectra are used. From the raw ACE-FTS spectra at each observed tangent altitude all known molecules are removed using the version 3.0 forward model (see `http://ace.uwaterloo.ca/` for a list of species). Residual spectra are calculated by ratioing the observed spectra with the calculated spectra. After some averaging, these resulting "continuum" or "baseline" spectra are used in our analyses. In each residual spectrum 500 points are averaged on the interpolated wavenumber grid (with a point spacing of $0.02/16\,\mathrm{cm}^{-1}$) to give a spectrum with a point spacing of $0.625\ \mathrm{cm}^{-1}$ and the resulting standard deviation is used as an estimate of the observational error. To exclude the regions of strong absorption, only points with a transmission in the calculated spectrum less than 0.5 were included. The points were then linear interpolated on a $2\,\mathrm{cm}^{-1}$ grid to give a K_{meas} and ΔK_{meas} for use with the computer code developed by *Eldering et al.* (2001), shown in Figure 4.10. The full spectrum method (black) and the window method (red) are displayed in Figure 4.10, of ss31868, as an example, at an altitude of approximately 15 km. The smoothness of the spectrum is improved for the window method, but due to the very good signal-to-noise ratio of ACE-FTS, it only makes a difference for large wavenumbers ($> 3500\,\mathrm{cm}^{-1}$), where the noise is enhanced. However, this interpolation has the advantage of a greater simplicity in the computational fitting procedure. The spectrum of the atmosphere is dominated by absorption lines of several trace gases, such as water vapour, ozone, and carbon dioxide. It is difficult to separate the broad aerosol absorption bands from sharper molecular lines and this is best accomplished using high resolution spectra. Fourier transform spectrometers (e.g., ACE (*Bernath et al.*, 2005), Atmospheric Trace Molecule Spectroscopy (ATMOS) (*Gunson et al.*, 1996)) have the required combination of high resolution, high signal-to-noise ratio and broad spectral bandwidth for the analysis method used in this paper (*Eldering et al.*, 2001, 2004; *Steele et al.*, 2003).

Figure 4.11 shows the continuum spectrum for a random occultation ss31868 for 7 different tangent heights between approximately 10 and 27 km. This occultation contains SO_2 and sulphuric acid as shown in following analysis, but in the continuum spectrum itself, it can be seen that particles or gases absorb at an altitude of about 15 km leading to a lowered transmission value.

For the determination of the aerosol properties, namely the volume slant column SC, the weight percent W, the radius r_g and the geometric standard deviation σ, six selected wavenumber ranges between $800\,\mathrm{cm}^{-1}$ and $4100\,\mathrm{cm}^{-1}$ are used. Certain wavenumber ranges cannot be used due to total absorption or strong interference of trace gases and the presence of nitrogen, oxygen, water and carbon dioxide continua not included in the ACE forward model. The region around $1040\ \mathrm{cm}^{-1}$ due to the ozone absorption band, from 1600 to $1800\,\mathrm{cm}^{-1}$, $3500 - 3900\,\mathrm{cm}^{-1}$ and $4050 - 4200\,\mathrm{cm}^{-1}$ because of H_2O absorption, $2200 - 2400\,\mathrm{cm}^{-1}$ due to N_2, CO_2 and N_2O absorption. Therefore, the six wavenumber ranges employed are: (1) a range between 820 and 920 cm^{-1}, (2) $1072 - 1240\ \mathrm{cm}^{-1}$, (3) $1850 - 2040\ \mathrm{cm}^{-1}$, (4) between 2680 and 2880 cm^{-1}, (5) $3230 - 3480\ \mathrm{cm}^{-1}$ and (6) $3900 - 4050\ \mathrm{cm}^{-1}$. The regions (1) and (2) contain significant H_2SO_4 absorption features and a minimum interference from other trace gases (*Eldering et al.*, 2001), however, these low wavenumber ranges (region (1) and region

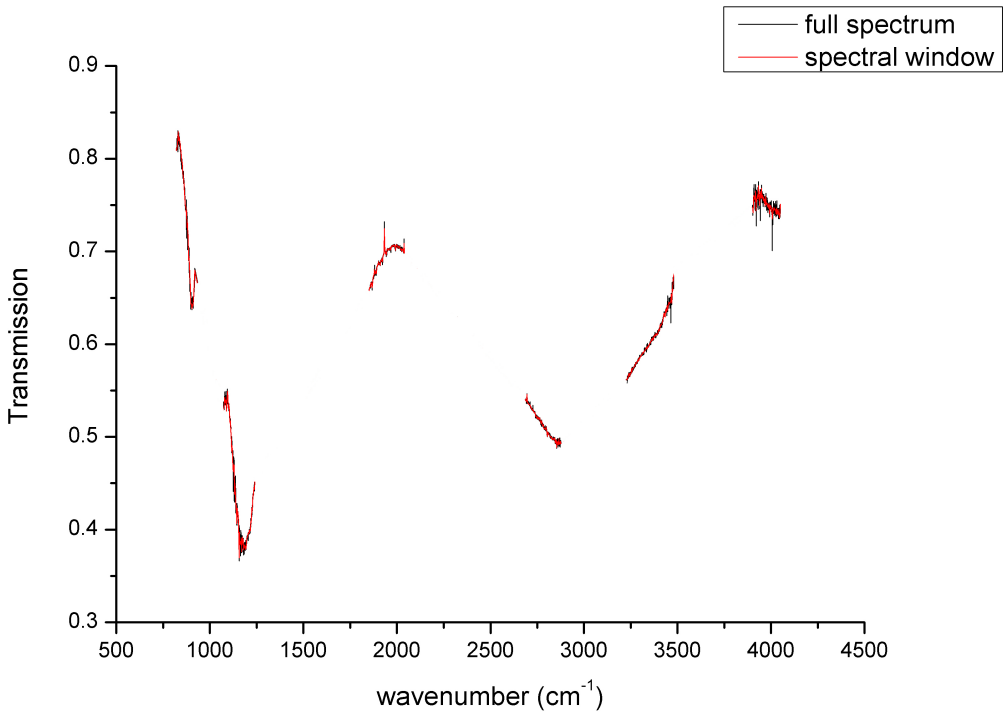

Figure 4.10: Displayed is the full spectrum method (black) and the window method (red) of ss31868 at an altitude of approximately 15 km. It can be seen that the smoothness of the spectrum is improved for the window method, but because of the very good signal-to-noise ratio, only makes a significant difference for large wavenumbers ($> 3500\,\mathrm{cm}^{-1}$).

(2)) do not provide information about the aerosol size distribution (r_g and σ) (*Eldering et al.*, 2001). Only the wide spectral range in the IR covering the NIR to the far-IR, like ACE-FTS spectra, is it possible to estimate this information. In our analyses, three or four free parameters were fitted (depending on the retrieval), including the volume slant column SC of the aerosol, the composition W, an offset α, and depending on the analysis the aerosol radius r_g to a set of 571 data points on a continuum spectrum of an ACE occultation. The inclusion of the offset α in the fitting procedure is useful if there are non-linearities in the detector or if there is extinction from a high concentration of particles which results in changes to the overall signal level.

An iterative algorithm has been employed for the retrieval of the parameters. Using a non-linear least-squares fitting algorithm, a modelled aerosol spectrum K_{model} has been fitted on the observed continuum spectrum K_{meas}. In each iteration the parameters have been modified. The modelled aerosol spectrum K_{model}, depending on a modelled extinction spectrum β_{model} and SC, expressed by:

$$K_{model}(\nu) = \alpha \cdot \prod_i \exp(-\int_x \beta_{model,i}(\nu, x) \cdot SC_i(x)dx) \tag{21}$$

$$= \alpha \cdot \prod_i \exp(-\beta_{model,i}(\nu) \cdot SC_i), \tag{22}$$

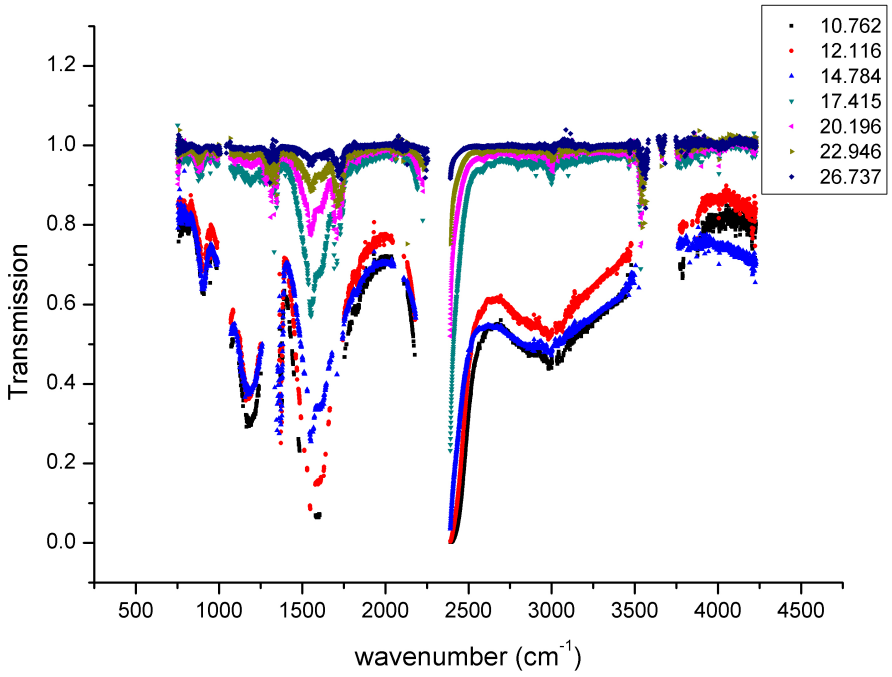

Figure 4.11: Shown are the "continuum" spectra (residuals of observed spectrum reduced by all the known molecules (v.3.0)) of the occultation ss31868. Seven different tangent heights (in km) are displayed in the graph, indicated by a colour scheme. For lower heights a strong absorption can be seen on the basis of the low transmission number and change of the shape of the transmission spectra.

with i representing a wide variety of aerosols which could be included. Figure 4.12 shows how the modelled transmission K_{model} changes for different input volume slant columns SC between 100 and 700 $\mu m^3\,cm^{-3}\,km$, representing typical values in the low stratosphere (background and volcanic), which occurred in our analyses. For this plot the modelled extinction β_{ext} was held constant, for aerosols with a radius $r_g = 0.08\,\mu m$, a geometric standard deviation $\sigma = 1.8$ and a weight percent of 65 % sulphuric acid and 35 % water. With an increasing aerosol volume the absorption is strengthened and, therefore, the transmission value decreases. The absorption lines also have a stronger shape and the absorption spectrum of sulphuric acid aerosol becomes more distinct with an increasing volume of particles.

To determine β_{model}, the Aerosol Extinction Estimation Program (AXE) (*Eldering et al.*, 2001) is used to calculate Mie extinctions between 800 and 4200 cm^{-1} in 2 cm^{-1} microwindows using refractive index data. In our analysis the extinction of H_2SO_4 aerosols were used, since volcanic aerosols are dominated by aqueous H_2SO_4 droplets (*Sheridan et al.*, 1992). The refractive indices for the modelled extinction β_{ext} are taken from *Tisdale et al.* (1998) at a temperature $T = 215\,K$ and a unimodal log-normal size distribution is employed. Apart from the optical constants of the aerosol particles, the extinction model β_{ext} is also influenced by changes of the radius r_g, the width σ and the composition W.

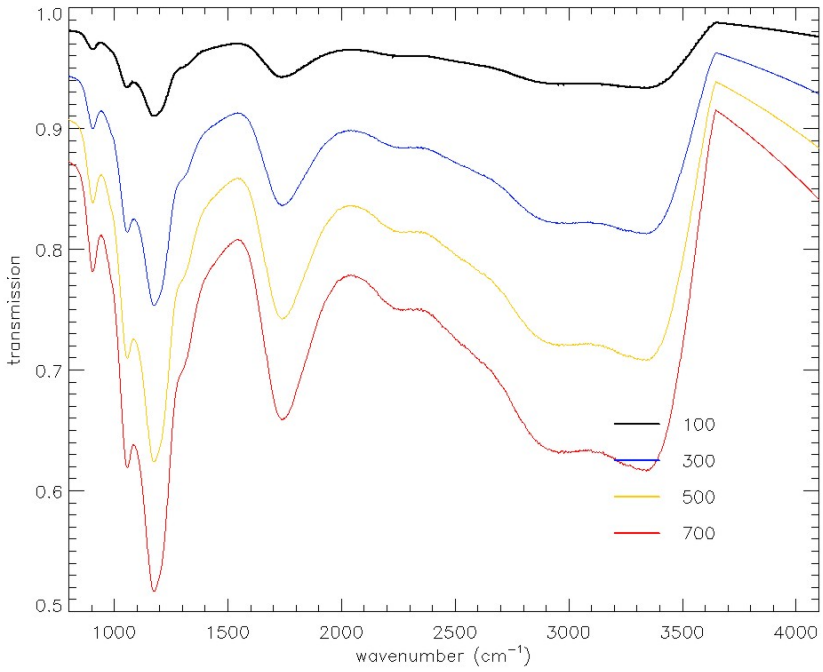

Figure 4.12: Shown is the transmission K_{model} against the wavenumber (cm^{-1}), for a constant radius $r_g = 0.08\,\mu\mathrm{m}$, width $\sigma = 1.8$ and weight percent $W = 65\,\%$. The colour scheme indicates the change of the the volume slant column SC in $\mu\mathrm{m}^3\,\mathrm{cm}^{-3}\,\mathrm{km}$.

Figure 4.13 demonstrates, how the transmission changes for five different compositions W between 60 % and 80 % for sulphuric acid aerosol with an equal aerosol volume slant column $SC = 500\,\mu\mathrm{m}^3\,\mathrm{cm}^{-3}\,\mathrm{km}$, equal radius $r_g = 0.08\,\mu\mathrm{m}$ and equal width $\sigma = 1.8$. The weight percent W is chosen to match a typical composition of sulphuric acid aerosol in the low stratosphere (*Shen et al.*, 1995). The results in Figure 4.13 show a high sensitivity for the aerosol composition at approximately $1200\,\mathrm{cm}^{-1}$ and especially for the region from $2500\,\mathrm{cm}^{-1}$ to $3500\,\mathrm{cm}^{-1}$.

Figure 4.14 shows the transmission for an equal aerosol volume slant column $SC = 500\,\mu\mathrm{m}^3\,\mathrm{cm}^{-3}\,\mathrm{km}$ of sulphuric acid aerosol for four different radii r_g between $0.01\,\mu\mathrm{m}$ and $0.64\,\mu\mathrm{m}$, with a constant composition of 65 % sulphuric acid and 35 % water and a geometric standard deviation of $\sigma = 1.8$. The result from Figure 4.14 shows a very low sensitivity of the radius for low wavenumbers, but a strong sensitivity for a wavenumber region above $3000\,\mathrm{cm}^{-1}$, towards the visible region.

In Figure 4.15 the results of the effect on the transmission due to a changing aerosol width σ, between 1.2 and 2.4, are presented for a constant aerosol volume slant column $SC = 500\,\mu\mathrm{m}^3\,\mathrm{cm}^{-3}\,\mathrm{km}$, for a 65 % sulphuric acid and 35 % water aerosol with a radius $r_g = 0.08\,\mu\mathrm{m}$. The transmission is sensible mainly for higher wavenumbers, above $3000\,\mathrm{cm}^{-1}$, towards the visible spectrum. The change of the transmission resulting from a changing width σ looks quite similar to the change of the radius r_g. Unfortunately, this means that it is not possible to retrieve the radius r_g and the width σ at the same time with the presented method. There are too many possible combinations of the radius r_g and the width σ, which result in the same transmission spectrum. Upon further analysis, it appears that the χ^2-value is flat for a wide range of size distribu-

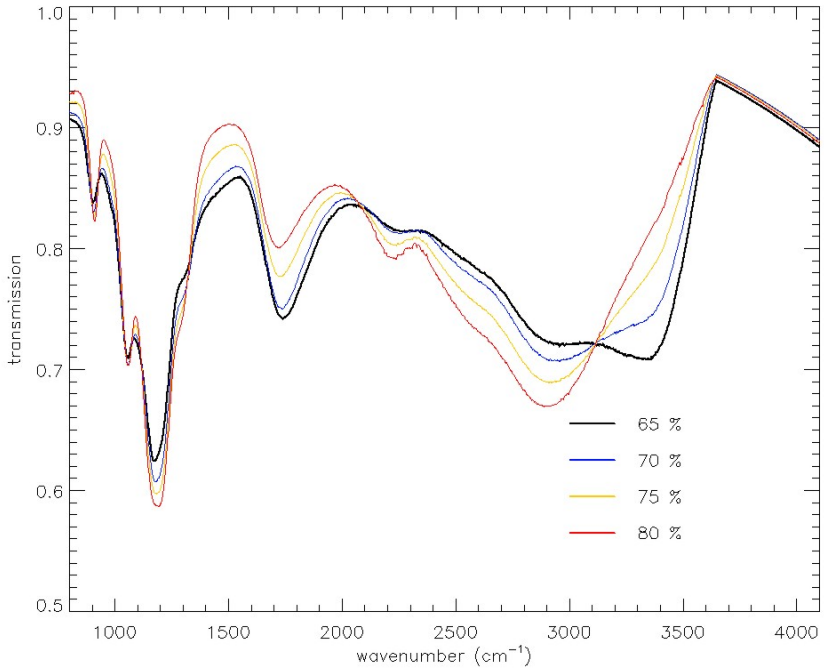

Figure 4.13: Shown is the transmission K_{model} against the wavenumber (cm^{-1}), for a constant geometric standard deviation $\sigma = 1.8$, volume slant column of aerosol $SC = 500\,\mu\mathrm{m}^3\,\mathrm{cm}^{-3}\,\mathrm{km}$ and radius $r_g = 0.08\,\mu\mathrm{m}$. The colour scheme indicates the change of the weight percent W in % of sulphuric acid.

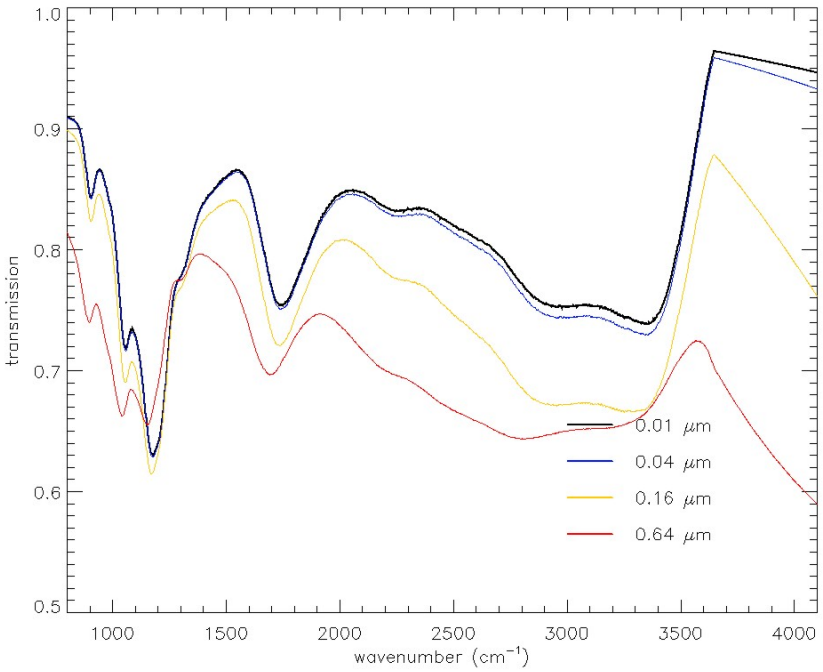

Figure 4.14: Shown is the transmission K_{model} against the wavenumber (cm^{-1}), for a constant geometric standard deviation $\sigma = 1.8$, volume slant column of aerosol $SC = 500\,\mu\mathrm{m}^3\,\mathrm{cm}^{-3}\,\mathrm{km}$ and weight percent $W = 65\,\%$. The colour scheme indicates the change of the radius r_g in μm.

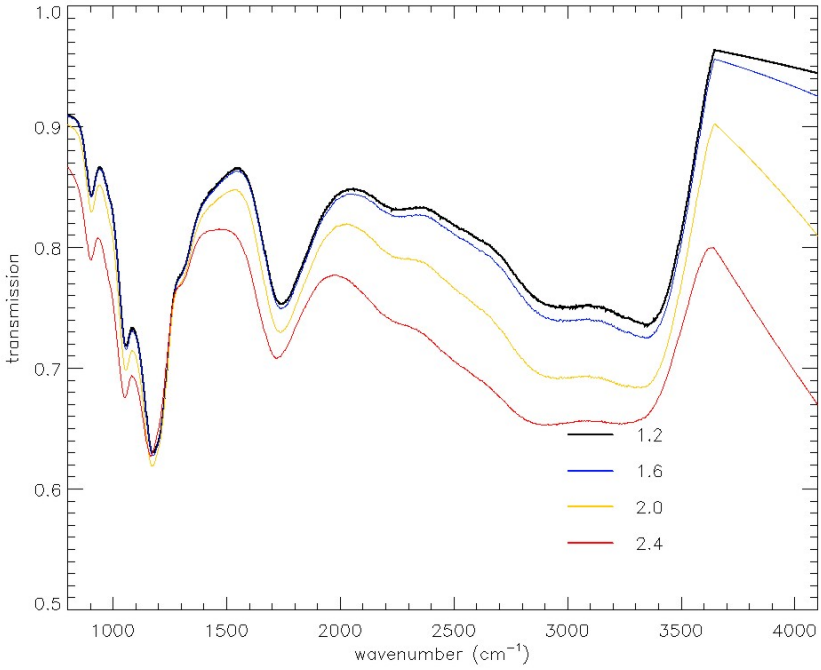

Figure 4.15: Shown is the transmission K_{model} against the wavenumber (cm^{-1}), for a constant radius $r_g = 0.08\,\mu\mathrm{m}$, volume slant column of aerosol $SC = 500\,\mu\mathrm{m}^3\,\mathrm{cm}^{-3}\,\mathrm{km}$ and weight percent $W = 65\,\%$. The colour scheme indicates the change of the width σ.

tions. A modelled extinction for a small radius r_g and a large σ has a similar shape to that of a large radius r_g and a small σ. Therefore, both parameters of the aerosol size distribution cannot be predicated at the same time and an estimated σ-value is needed to get a best fit radius r_g.

The χ^2 value is calculated to determine the quality of the sulphate aerosol retrieval. This parameter indicates how well the modelled spectrum K_{model} reproduces the observed spectrum K_{meas}, and defined as:

$$\chi^2 = \frac{1}{N} \cdot \sum_{k=1}^{N} \left[\frac{K_{meas}(\nu_k) - K_{model}(\nu_k)}{\Delta K_{meas}(\nu_k)} \right]^2, \tag{23}$$

in which N are the degrees of freedom, which is the difference between the number of points (571) and the number of free parameters (3 or 4) in the least-squares fitting. When the observed spectrum is divided by the calculated spectrum, a few hundred points are averaged, the error of the continuum spectrum ΔK_{meas} equates to the standard deviation of the mean for this calculation.

Figure 4.16 (a) and (b) are examples for two occultations with (a) Kasatochi volcanic aerosol signal and (b) Sarychev volcanic aerosol signal. These spectra (sr27216 and ss31868) were measured on 1 September 2008 (35.27°N, 84.07°W) and 14 July 2009 (68.31°N, 18.86°W), respectively and displaying sulphate aerosol extinction. Volcanic influence in these occultations has been found through a very high SO_2 concentration, with maximum SO_2 concentration of $[SO_2] = 2.56 \pm 0.04\,\mathrm{ppb}$ (sr27216) and $[SO_2] = 4.73 \pm 0.07\,\mathrm{ppb}$ (ss31868), respectively. Figure 4.16 shows that the modelled

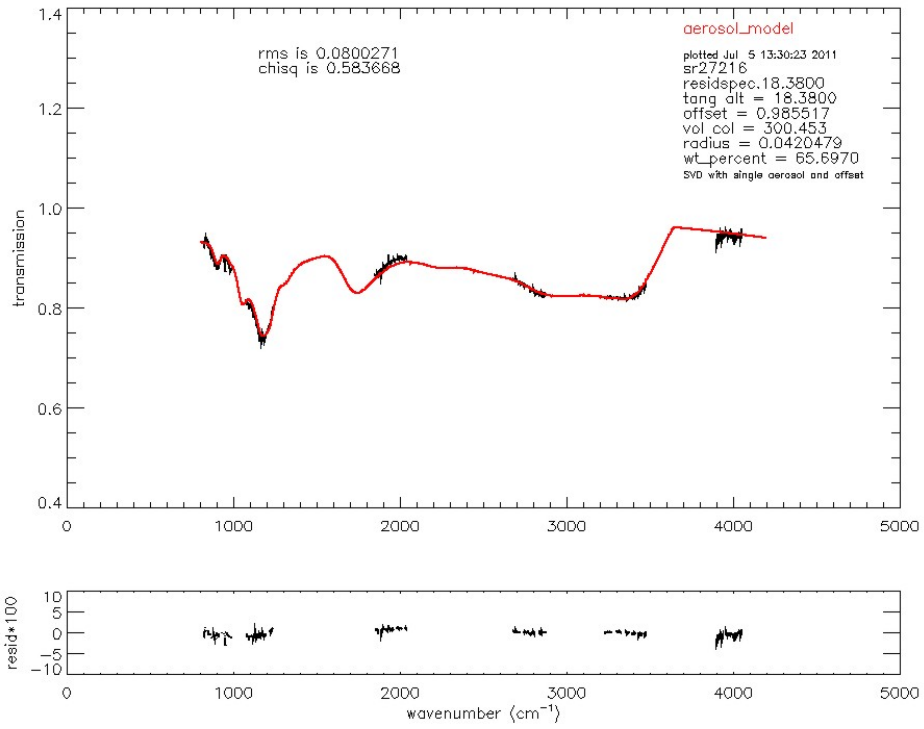

(a) sr27216 (01.09.2008, 35.27°N, 84.07°W) at 18.4 km

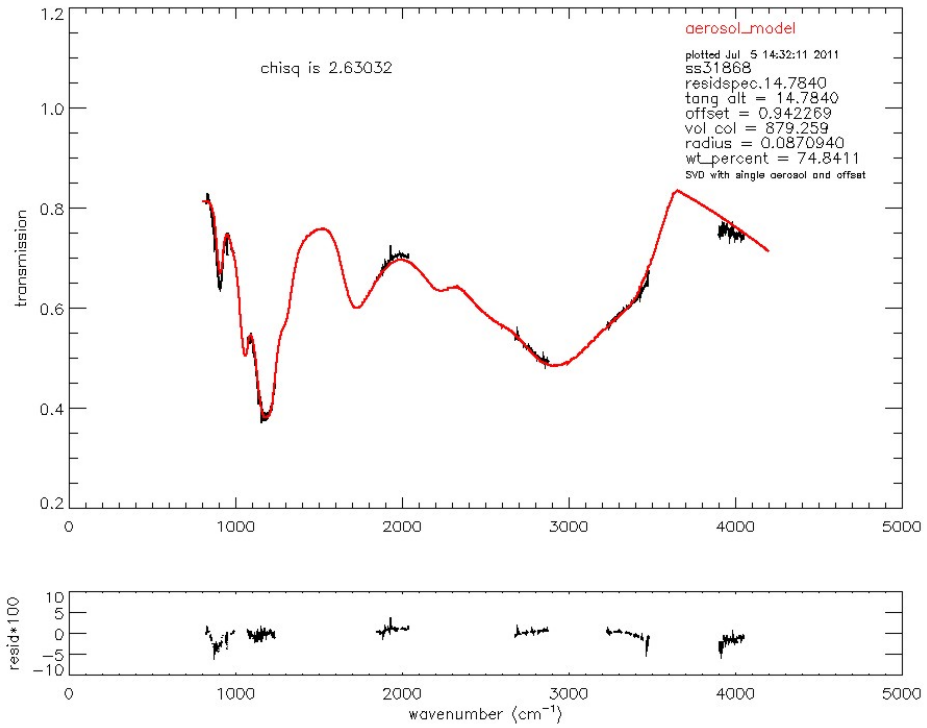

(b) ss31868 (14.07.2009, 68.31°N, 18.86°W) at 14.8 km

Figure 4.16: K_{meas} (black) and K_{model} (red) against the wavenumber (cm^{-1}) between 800 and 4200 cm^{-1}, are shown for two different occultations at the tangent height with the maximum aerosol signal. The residuals are displayed in the lower graph showing the precision of the fitting.

spectrum (red) follows the shape of the observed continuum spectrum (black) quite well with a $\chi^2 \approx 0.6$ and $\chi^2 \approx 1.4$, respectively for a fixed $\sigma = 1.8$ and floated values SC, W and r_g at a tangent height of about 18 km and 15 km (height of the maximum SO_2 concentration). The reason for the unrealistically small χ^2-value ($\chi^2 < 1$) is due to an overestimated error ΔK_{meas} of the observed spectrum K_{meas}.

The retrieved SC can be inverted into an actual vertical profile of aerosol loading by assuming a homogeneous cloud with 1 km layers. This assumption is not very realistic because the horizontal extent of the cloud is unknown; however,the assumption allows the cloud height to be estimated and an approximate image of the cloud can be produced in many cases.

Depending upon the interest of parameters from the aerosol size distribution, different programmes are run with a different amount of free parameters. If a radius r_g should be retrieved, Program (1) is employed, the geometric standard deviation σ must be fixed (to a value between 1.2 and 2.5), while the radius r_g can be derived for $0.01\,\mu\text{m} \leq r_g \leq 1.28\,\mu\text{m}$. If a radius cannot be found in this range or the intensity is too low to retrieve the radius r_g, the radius is set to $r_g = 0.011\,\mu\text{m}$. For each individual tangent height, the free parameters are retrieved with a non-linear least-squares fitting algorithm, starting at the highest available altitude (approximately 28 km). For the retrieval of the effective radius R_{eff}, Program (2) is employed, where the radius r_g and the width σ are fixed inside the least-squares fitting, but varied for each tangent height between a radius of $0.01\,\mu\text{m}$ and $1.28\,\mu\text{m}$ in steps of $0.01\,\mu\text{m}$ and between a width σ of 1.2 and 2.5 in steps of 0.1. The retrieved values of the aerosol volume slant column SC, the weight percent W, the offset α, as well as the χ^2 are saved and analysed, for all retrievals in each tangent height.

4.3.2. Error retrieval

The method used for the retrieval of the errors in the free parameters was used by *Steele et al.* (2006) in a similar context. Here, the error Δx_j of the derived parameters j (SC, W, α and r_g in some cases) results from the non-linear least-squares fitting matrix $D_{j,i}$, sometimes called design matrix and the difference between the modelled and the observed spectrum ΔK_i for each wavelength microwindow i (total 571).

$$\mathbf{D}_{i,j} = \frac{X_j(x_i)}{\Delta K_{meas,i}} \tag{24}$$

$X_j(x_i)$ are the so called basis functions of x, while the design matrix $\mathbf{D}_{i,j}$ is the matrix of the fitting problem. (*Press et al.*, 1992)

The quotient of the square of the difference between the spectra ΔK and the square of the matrix $\mathbf{D}$ leads to the square of the error for each parameter. The error Δx_j is therefore defined as:

$$\Delta x_j = \sqrt{\sum_{i}^{571} \frac{\Delta K_i^2}{\mathbf{D}_{j,i}^2}}. \tag{25}$$

4.3.3. Analysis of background concentrations

A background concentration of sulphate aerosol was retrieved in order to compare these results with retrievals after a major volcanic eruption. The occultation (ss26502:

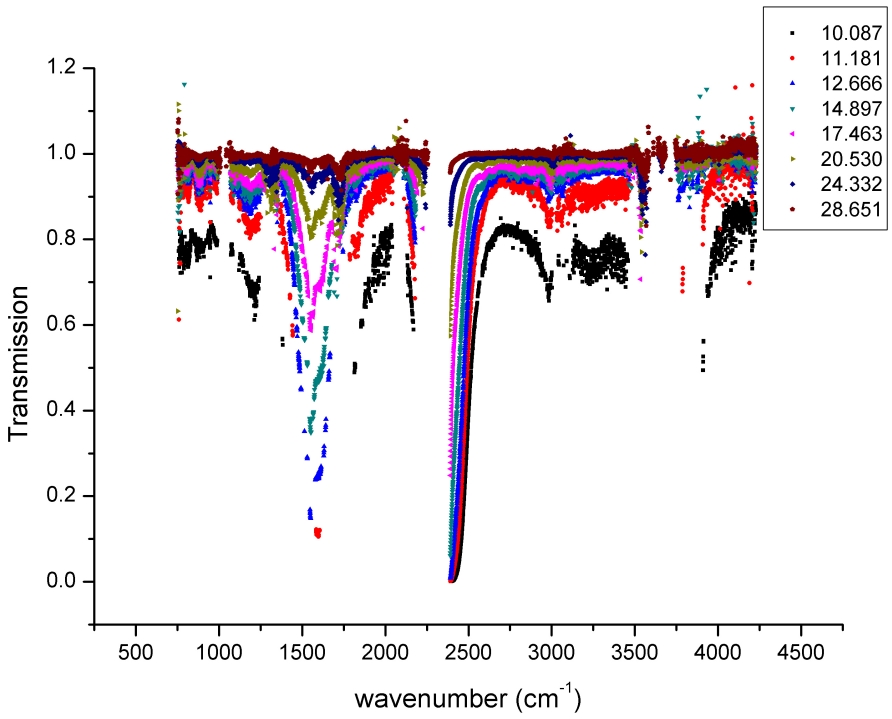

Figure 4.17: Shown are the "continuum" spectra (residuals of observed spectrum reduced by all the known molecules (v.3.0)) of the occultation ss26502 (15.07.2008, 67.97°N, 31.12°W), representing a background, without any volcanic influence. Eight different tangent heights (in km) are displayed in the graph, indicated by a colour scheme. The transmission value is much higher compared to a spectrum, influenced by a volcano (see Figure 4.11).

15.07.2008, 67.97°N, 31.12°W) used for this purpose, was chosen to match the location and date (from another year) of one of the analysed occultations, influenced by the Sarychev volcano (ss31868: 14.07.2009, 68.31°N, 18.86°W). Figure 4.17 shows the measured continuum spectrum K_{meas} of this background occultation for eight different tangent heights (in km). Compared to the continuum spectrum influenced by the Sarychev volcano (Figure 4.11), the transmission of the background occultation does not represent strong absorption lines, resulting in a much higher transmission value, even for low altitudes. The plotted spectrum in Figure 4.17 also demonstrates that for very low tangent heights (10 km and 11 km) the continuum spectrum is not well obtained, leading to high noise and many missing data points. Therefore, the spectra at 10 km and 11 km are not included in further analysis.

The results of the sulphate aerosol retrieval are illustrated in Figure 4.18, showing the aerosol slant column SC, the aerosol volume density, the offset α and the χ^2-value. These values were retrieved, by floating the aerosol volume slant column SC and the offset α, for a typical background sulphate aerosol (70 % sulphuric acid and 30 % water) with a radius of $r_g = 0.08\,\mu$m, $\sigma = 2.0$ (*Oberbeck et al.*, 1983). The aerosol volume density shows an aerosol loading between 0.05 and 0.13 $\mu m^3\,cm^{-3}$ for a tangent height between 29 and 15 km. These values are realistic for a background retrieval, as typical retrieved values are 0.15 $\mu m^3\,cm^{-3}$ at 15 km and decreasing with altitude to 0.01 $\mu m^3\,cm^{-3}$ at 25 km (*Steele et al.*, 1999). The χ^2-value indicates a quite good

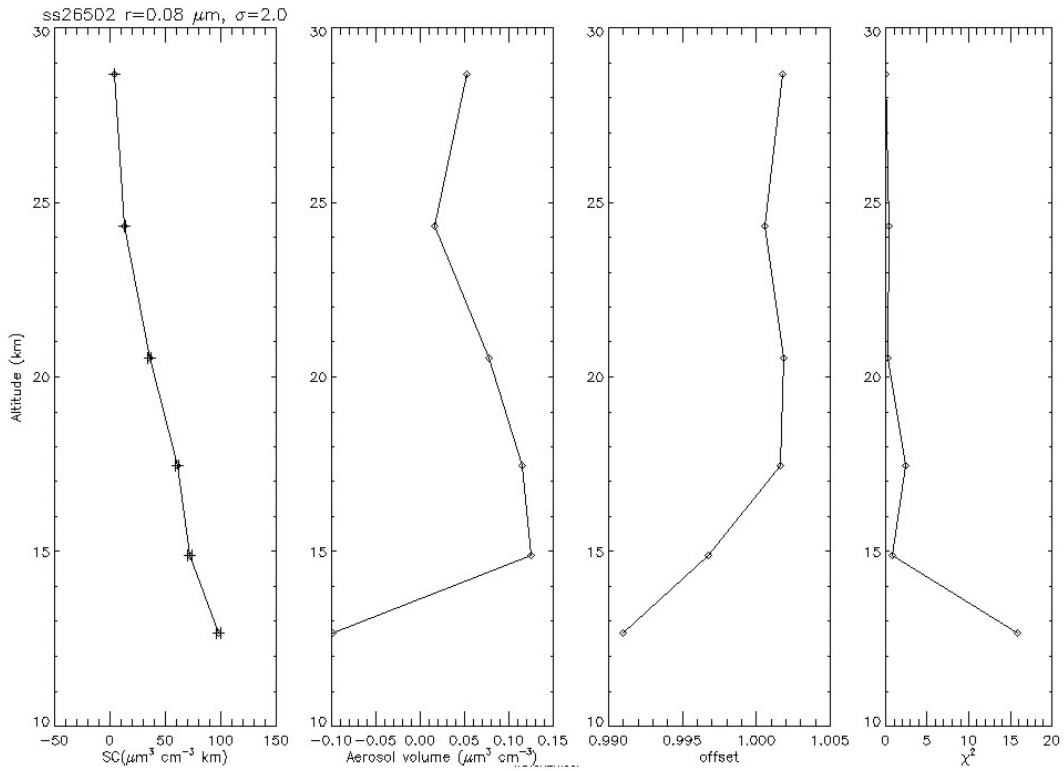

Figure 4.18: Retrieved aerosol properties for the occultation ss26502 (15.07.2008, 67.97°N, 31.12°W). Shown is the aerosol SC, the aerosol loading, the offset α and χ^2. No strong aerosol loading can be detected for the background retrieval.

retrieval of the aerosol properties, as the value is close to 1, meaning that the modelled spectrum follows the observed spectrum very well. Only at the tangent height of approximately 12 km the retrieval is not successful, as the aerosol volume slant column is negative and the χ^2-value is approximately 15, an indicator of a poor retrieval. The offset α is almost 1 for each tangent height, showing that the detector of ACE-FTS is linear. When the offset α occurs to be $\alpha \neq 1$ in further analysis, this is likely due to extinction of other aerosol particles or trace gases, reducing the transmission value.

The modelled and observed continuum spectra (K_{model} and K_{meas}) of the background occultation ss26502 in Figure 4.19, show a weak absorption bands from sulphate aerosol with a volume slant column $SC \approx 72\,\mu\text{m}^3\,\text{cm}^{-3}\,\text{km}$ at approximately 15 km. This absorption can be seen best at low wavenumbers between 800 and 1200 cm^{-1}. The uncertainty parameter χ^2 shows a very good agreement with the modelled spectrum, but also for this case the error of the observed spectrum is slightly overestimated, resulting in a χ^2-value less than 1.

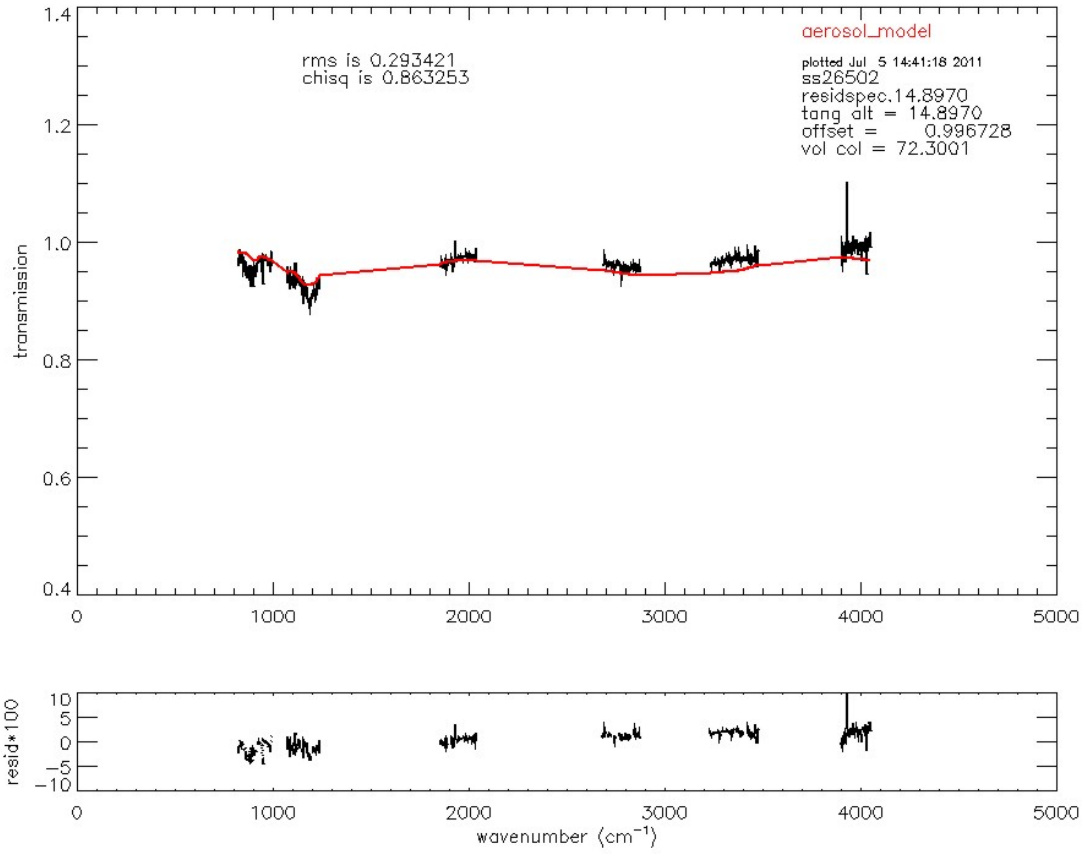

Figure 4.19: K_{meas} (black) and K_{model} against the wavenumber (cm^{-1}) between 800 and 4200 cm^{-1} is shown for the occultation ss26502 (15.07.2008, 67.97°N, 31.12°W) for the tangent height at approximately 15 km. No strong absorption lines due to sulphate aerosols can be seen, resulting in a very low volume slant column $SC \approx 72\,\mu m^3\,cm^{-3}\,km$. The residuals are displayed in the lower panel showing the precision of the fitting.

5. Data analysis and discussion

5.1. Volcanic plume detection

5.1.1. On the example of Kasatochi

Evidence of the Kasatochi eruptions using ACE-FTS data first occurred in September 2008. The volcano erupted at the beginning of August, the month that ACE orbits around the equator (with a latitudinal coverage of less than 15°N), therefore, the eruptions have first been detected in September 2008 and at the very end of August 2008. The first occultation with an enhanced SO_2 concentration was sr27199 (31.08.2008, 30.41°N, 27.79°W), measuring $[SO_2] = 0.48 \pm 0.02$ ppb. In September 2008, where ACE orbits around a latitude between 30° and 85° in the Northern Hemisphere, 258 occultations have been detected with enhanced SO_2 concentrations.

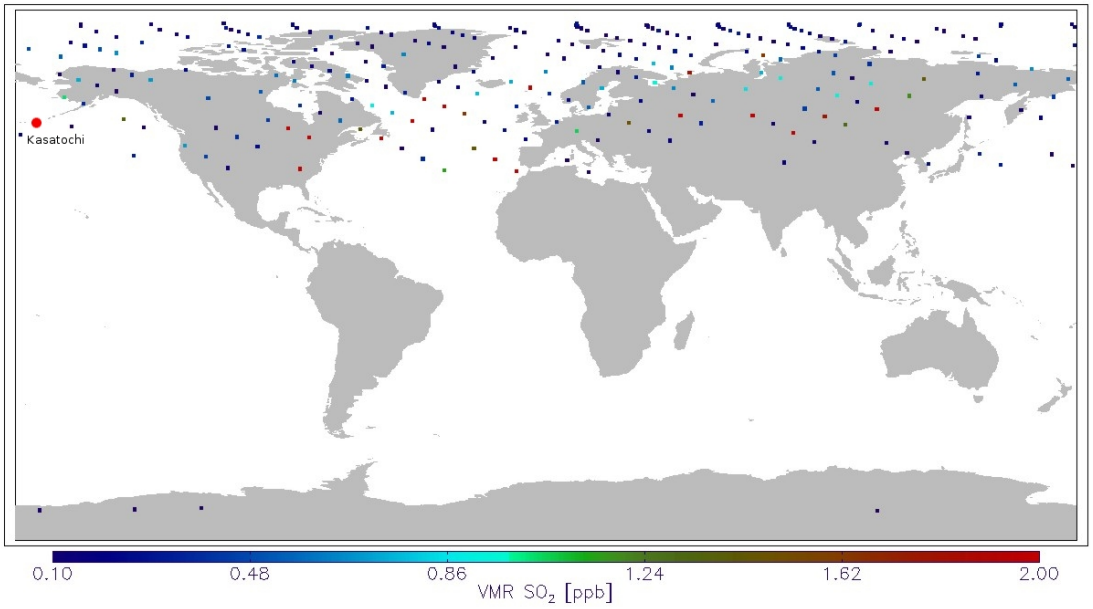

Figure 5.1: Map of occultation locations with an SO_2 concentration greater than 0.1 ppb for September 2008. There are in total 258 occultations with enhanced SO_2. The colour scheme indicates the maximum concentration for each occultation. The large red dot displays the location of Kasatochi.

One month after the eruptions of Kasatochi, the volcanic plume spread over most of the Northern Hemisphere (NH) ($90-30$°N), which can be seen in Figure 5.1 for September 2008. In this Figure the occultations with an enhanced SO_2 concentration, which are in total 258 occultations, are plotted, while the colour scheme indicates the maximum SO_2 concentration (in ppb) of the occultation profile (between 12 and 25 km). There are four occultations with enhanced SO_2 in the Southern Hemisphere (SH) which are not related to the Kasatochi eruptions. These can be discounted because the mean transport time within the Hemispheres is approximately 1 year, therefore, the volcanic plume cannot reach the SH one month after the eruptions. These enhanced SO_2 concentrations are most likely related to volcanic activity in the SH, for example Chaiten (Chile) erupted in August and September 2008 with a strato-volcanic plume height of approximately 12 km (*AURA*, 2009), which would be detectable by ACE.

5.1.2. On the example of Sarychev

The first evidence of the eruptions of the Sarychev volcano in ACE profiles occurred in July 2009 because the satellite cannot take any measurements between the 10 and 29 June because the satellite is always in sunlight, when sunset and sunrise observations cannot be taken. The first occultation (ss31667: 35.41°N, 78.75°W) with enhanced SO_2 of $[SO_2] = 0.130 \pm 0.032$ ppb was detected on 30 June 2009, indicating the volcanic plume. In July 2009, 235 occultations with enhanced SO_2 were observed by ACE-FTS, orbiting between 35° and 65° in the NH.

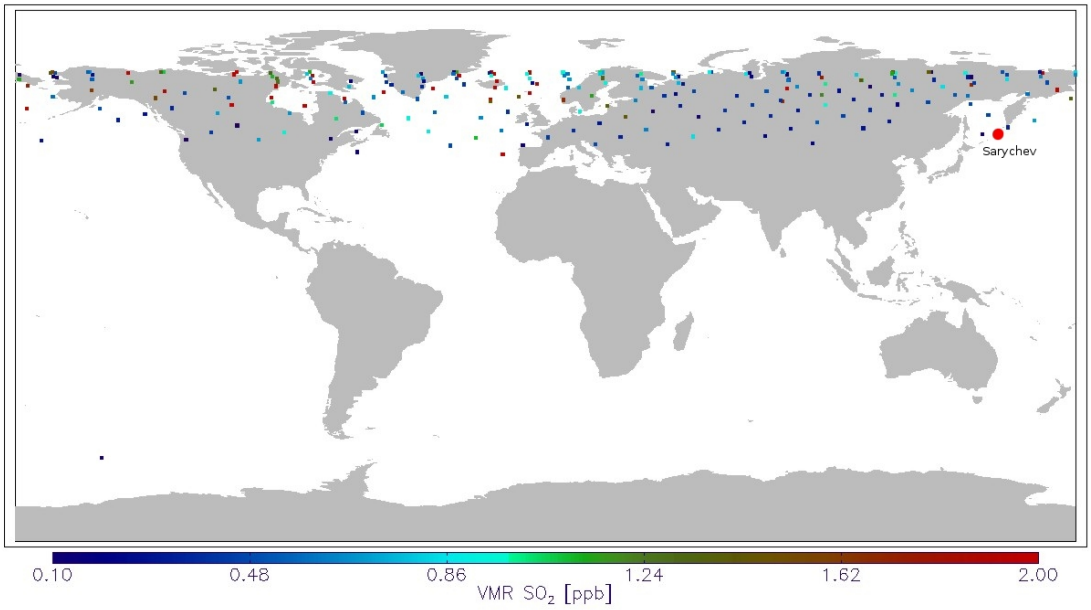

Figure 5.2: Map occultation locations with an SO_2 concentration greater than 0.1 ppb for July 2009. There are in total 235 occultations with enhanced SO_2. The colour scheme indicates the maximum concentration for each occultation. The large red dot displays the location of Sarychev.

Figure 5.2 shows the location of sulphur dioxide above 0.1 ppb for July 2009, which represents the presence of a volcanic plume. The colour scheme in Figure 5.2 indicates the highest concentration of the observed profile within one measurement. The volcanic plume spread over almost the entire NH in the month just after the eruptions, while the Southern Hemisphere is unaffected by the Sarychev volcano because of a long transportation time between the Hemispheres. One occultation was found in the Southern Hemisphere (see Figure 5.2) with SO_2 concentrations of about 0.1 ppb, but this is likely related to other volcanic activity in the Southern Hemisphere (e.g. Chaiten (Chile) or Ubinas (Peru) (*AURA*, 2009)).

5.2. Observed properties of the aerosol layer

5.2.1. On the example of Kasatochi

A significantly enhanced atmospheric extinction can be seen in Figure 5.3 for September 2008, just after the eruptions of Kasatochi. In Figure 5.3, the median atmospheric extinction (NIR) is displayed for September between 2004 and 2010 in the Northern

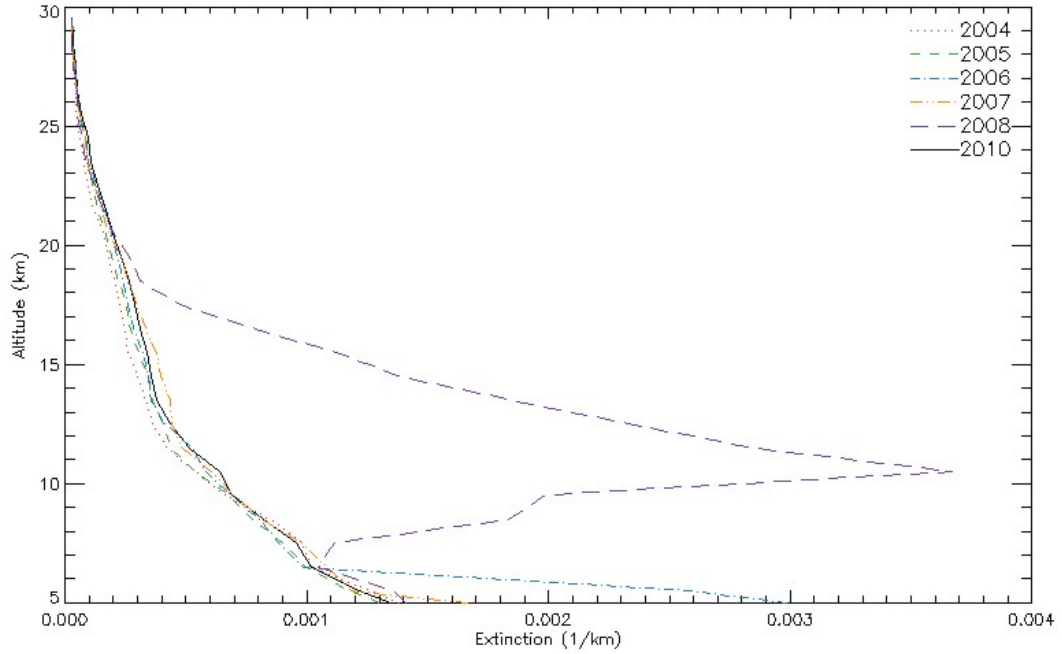

Figure 5.3: Median atmospheric extinction (NIR, v.2.2) in September from 2004 to 2010 in the NH. An enhanced layer can be seen in September 2008 between 6.5 km and 17.5 km, with a maximum of $b_{ext} = 0.0037\,\mathrm{km}^{-1}$ at almost 11 km.

Hemisphere, using an analysis method similar to that of *Sioris et al.* (2010). For 2008 an enhanced extinction layer has a maximum of $b_{ext} = 0.0037\,\mathrm{km}^{-1}$ at almost 11 km, the enhancement spans from 6.5 km to 17.5 km altitude. This enhancement only occurs in September 2008, while the usual atmospheric extinction in September at 13 km is approximately $b_{ext} \approx 0.0004\,\mathrm{km}^{-1}$, which is almost one order of magnitude smaller than in 2008. This indicates a clear layer of absorbing and scattering particles in the higher troposphere and lower stratosphere, which is caused by the volcanic eruptions.

The Figures from 5.4 to 5.7 show the retrieved profiles of the SO_2 concentration (ppb), the atmospheric extinction b_{ext} (NIR, v.2.2, in km^{-1}) and the sulphate aerosol volume density ($\mu\mathrm{m}^3\,\mathrm{cm}^{-3}$) for four different occultations detected in September 2008 in the NH. The results in Figure 5.4 show that the retrievals of the occultation sr27216 (01.09.2008, 35.27°N, 84.07°W) have a maximum at approximately 18.5 km in all three cases. The height and the approximate shape of the plume on the 1 September 2008 is in very good agreement between the three different retrievals. The maximum SO_2 concentration reaches $[SO_2] = 2.57 \pm 0.04\,\mathrm{ppb}$, while the atmospheric extinction and the sulphate aerosol loading are approximately one order of magnitude higher than the background. Figure 5.5, 5.6 and 5.7 show the sulphuric dioxide concentration (ppb), the atmospheric extinction b_{ext} (NIR, v.2.2, in km^{-1}) and the aerosol loading ($\mu\mathrm{m}^3\,\mathrm{cm}^{-3}$) profiles for the occultations sr27268 (04.09.2008, 47.58°N, 83.30°E), sr27288 (06.09.2008, 51.48°N, 45.92°W) and sr27317 (08.09.2008, 56.51°N, 35.07°W), respectively. For these cases the results also are in very good agreement, showing a plume at approximately 18.5 km for all analyses. Certain results even show a second plume at approximately 8.5 km, depending on if there are successful retrievals at this low altitude. The SO_2 concentration has a maximum between 4 and 2 ppb, however,

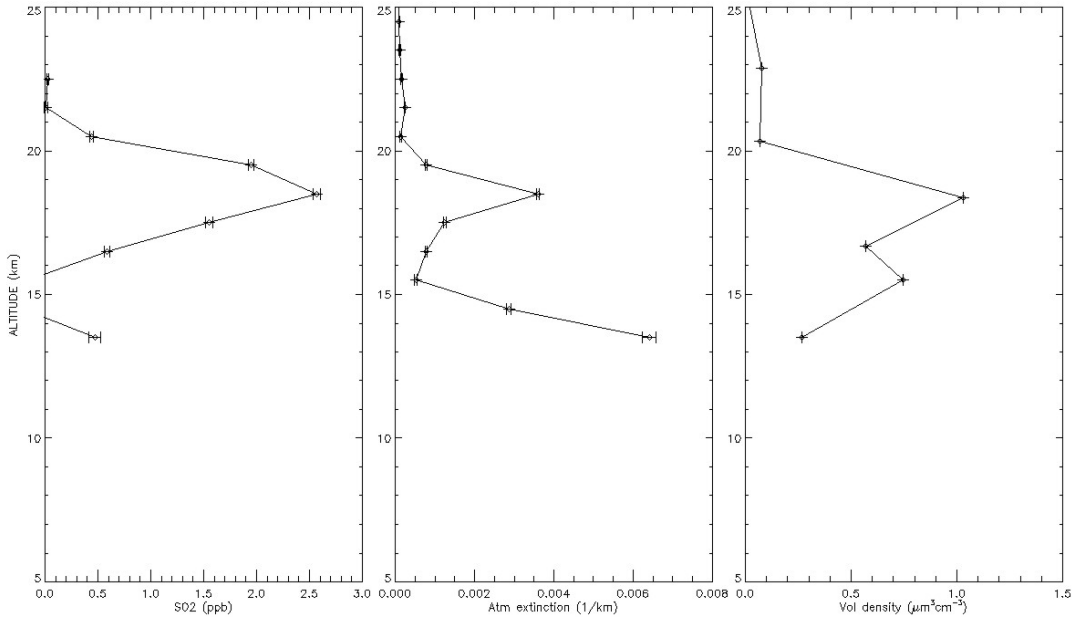

Figure 5.4: The SO_2 concentration profile in ppb, atmospheric extinction b_{ext} in km^{-1} (NIR, v.2.2) and the aerosol loading ($\mu m^3 cm^{-3}$) are illustrated for ss27216, which was detected on 1 September 2008 (35.27°N, 84.07°W). Note that the SO_2 and atmospheric extinction are on a 1 km altitude grid, but the aerosol retrieval is carried out for the spectra at the observed tangent height.

a dilution over time cannot be seen, the concentration most likely depends on where the plume was detected and how concentrated the plume was at this location. The maximum sulphate aerosol density is between 1 $\mu m^3\,cm^{-3}$ and 1.5 $\mu m^3\,cm^{-3}$ and seems to be proportional with the concentration of SO_2. The atmospheric extinction is in all four examples approximately 0.004 km^{-1} and does not show a strong coherence to the sulphate and sulphur dioxide loading. The results of the Figures 5.4 - 5.7 prove reliability in the consistency and agreement of the different instruments and retrievals from ACE data and the retrieval of the aerosol loading using the previously described method.

The median atmospheric extinction (NIR, v.2.2) over an interval of 5° in latitude for September 2008 is displayed in Figure 5.8. The results in Figure 5.8 show an enhanced layer (red) between 55°N and 70°N, partly below and partly above the tropopause (black solid line) between an altitude of 8 km and 11 km. Between 35°N and 45°N no influence from the volcano can be detected, showing background atmospheric extinction. A small enhancement between 45°N and 55°N can be seen, showing a slightly larger atmospheric extinction than the background.

A similar graph shows the median sulphuric dioxide VMR for September 2008, displayed in Figure 5.9, with a resolution of 5° in latitude. Here the layer of the volcanic plume is not as well defined as for the atmospheric extinction, a possible reason for that could be the relatively low number of occultations detecting sulphur dioxide and the limit of minimum altitude of 12.5 km. However, strongly enhanced layers of SO_2 occur between 50°N and 70°N and between 12.5 km and 18.5 km.

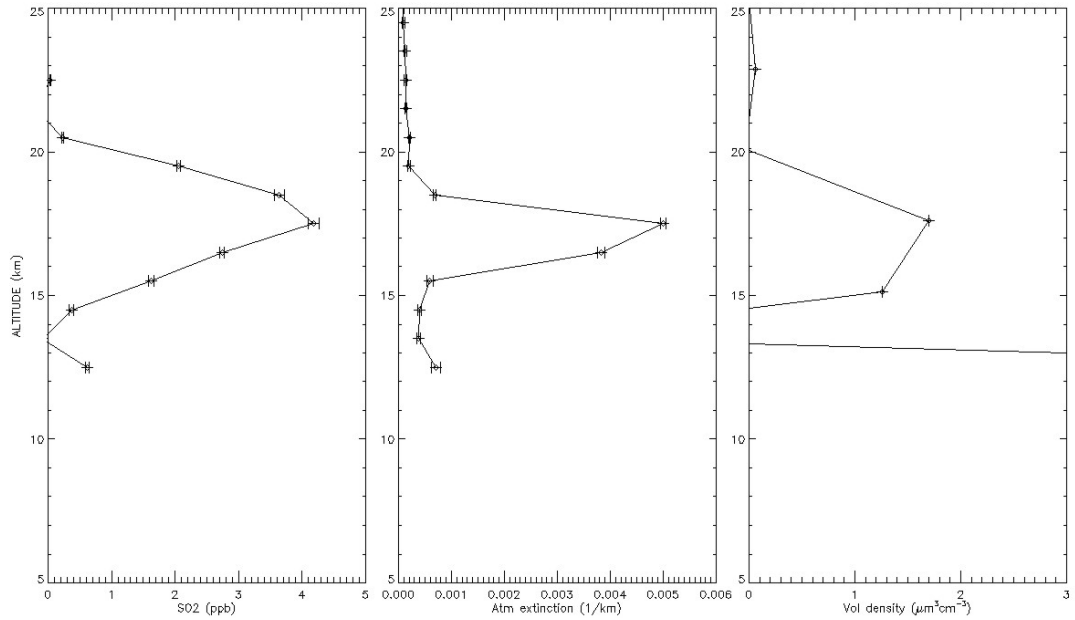

Figure 5.5: The SO_2 concentration profile in ppb, atmospheric extinction b_{ext} in km^{-1} (NIR, v.2.2) and the aerosol loading ($\mu m^3 cm^{-3}$) are illustrated for ss27268, which was detected on 4 September 2008 (47.58°N, 83.30°E). Note that the SO_2 and atmospheric extinction are on a 1 km altitude grid, but the aerosol retrieval is carried out for the spectra at the observed tangent height.

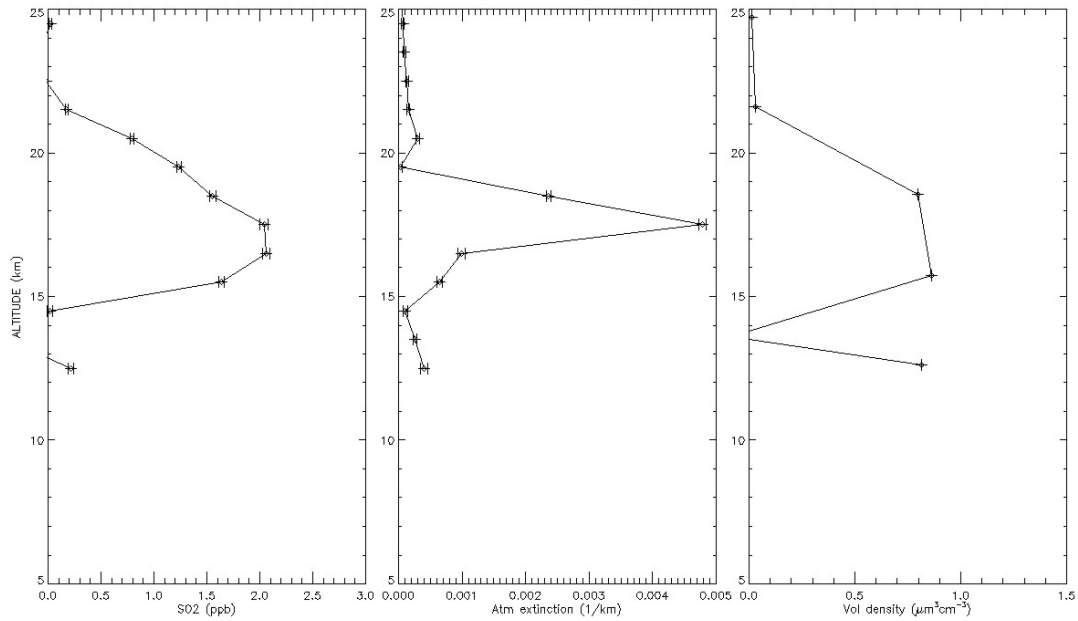

Figure 5.6: The SO_2 concentration profile in ppb, atmospheric extinction b_{ext} in km^{-1} (NIR, v.2.2) and the aerosol loading ($\mu m^3 cm^{-3}$) are illustrated for ss27288, which was detected on 6 September 2008 (51.48°N, 45.92°W). Note that the SO_2 and atmospheric extinction are on a 1 km altitude grid, but the aerosol retrieval is carried out for the spectra at the observed tangent height.

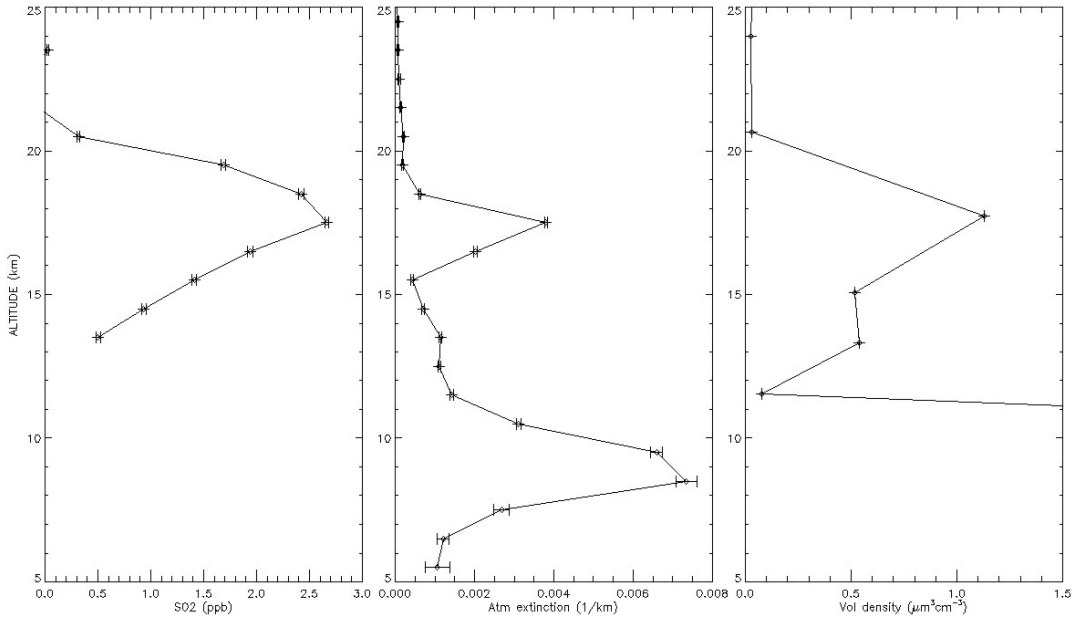

Figure 5.7: The SO_2 concentration profile in ppb, atmospheric extinction b_{ext} in km^{-1} (NIR, v.2.2) and the aerosol loading ($\mu m^3 cm^{-3}$) are illustrated for ss27317, which was detected on 8 September 2008 (56.51°N, 35.07°W). Note that the SO_2 and atmospheric extinction are on a 1 km altitude grid, but the aerosol retrieval is carried out for the spectra at the observed tangent height.

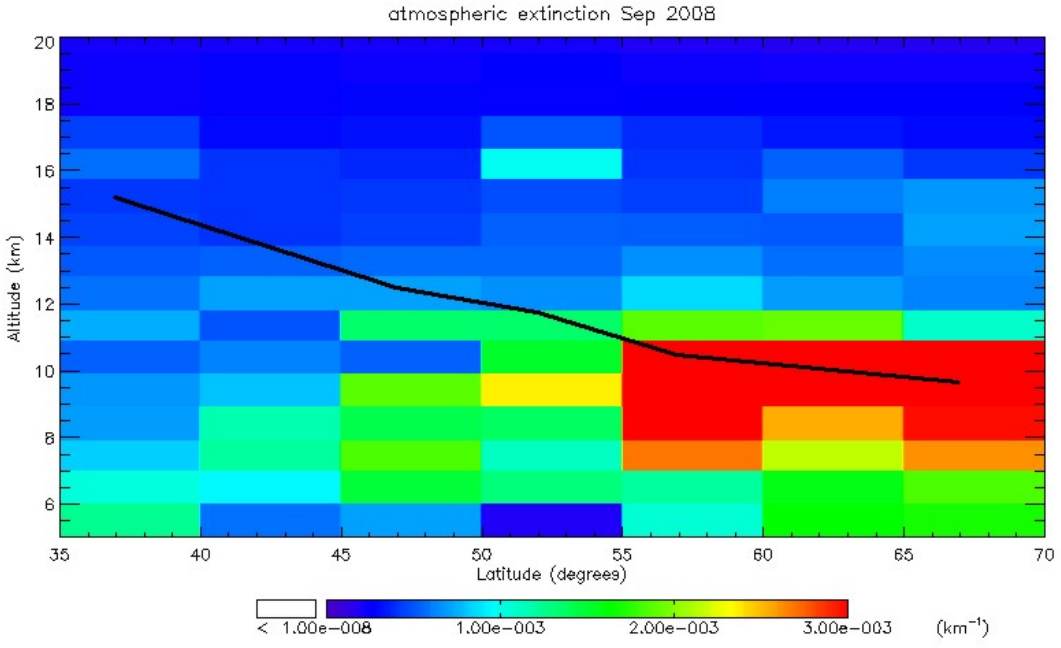

Figure 5.8: Profile of the median atmospheric extinction b_{ext} (km^{-1}) (NIR, v.2.2) in September 2008 in the Northern Hemisphere. The colour scheme indicates the strength of the atmospheric extinction, while a clear, enhanced layer (red) is between 55°N and 70°N. The median tropopause is shown as a black line.

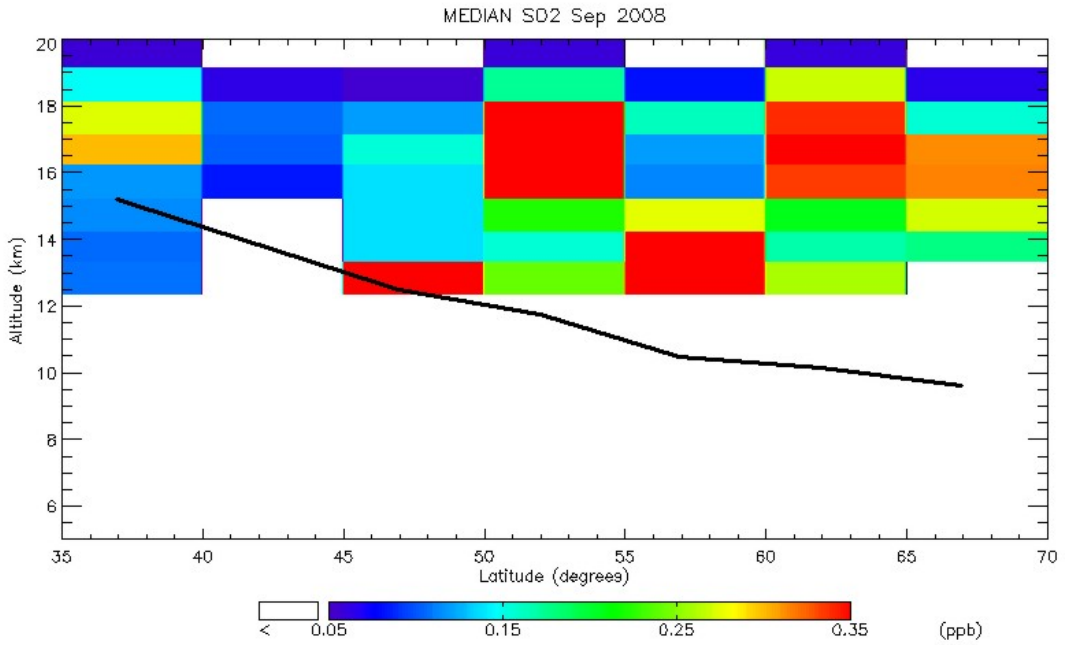

Figure 5.9: Profile of the median SO_2 concentration (ppb) in September 2008 in the Northern Hemisphere, showing an enhanced layer (red) between 50°N and 70°N. The median tropopause is shown as a black line.

5.2.2. On the example of Sarychev

A strong aerosol layer, according to enhanced atmospheric extinction (NIR-Imager) can be seen in July 2009 in the Northern Hemisphere. Figure 5.10 shows the median atmospheric extinction (NIR) in July between 2004 and 2009 (there was no successfully retrieved atmospheric extinction in July 2007). Only in July 2009 can an enhancement be seen with the usual atmospheric extinction at this altitude being approximately 0.0004 km^{-1}, which is almost one order of magnitude smaller than the enhancement. The aerosol layer spans from approximately 8.5 km to 17.5 km with a maximum extinction of 0.0028 km^{-1} at an altitude of 13 km.

Figure 5.11 illustrates the profile of the SO_2 concentration, the atmospheric extinction and the aerosol loading from 14 July 2009 (68.31°N, 18.86°W), showing a clear layer in the lower stratosphere and a possible second peak below 10.5 km. These three profiles are in very good agreement, since the plume height is at approximately 15 km in all three cases and the profiles have a similar shape. The atmospheric extinction has a maximum of almost an order of magnitude greater than the average monthly median. The SO_2 concentration reaches 5 ppb, the aerosol volume slant column $SC = 900\,\mu m^3\,cm^{-3}$ km and for a homogeneous cloud an aerosol loading of almost 3 $\mu m\,cm^{-3}$ is achieved.

Figure 5.12 shows another example for an occultation on the 21 July 2009 (63.51°N, 176.37°W), showing a clear layer also at an altitude of 15 km. The profile of the aerosol loading does not show the same shape like the SO_2 concentration and atmospheric extinction. The reason could be the wrong assumption of 1 km cloud layers for the retrieval of the aerosol volume density from the slant column SC, the unknown path-length and the second lower plume layer at approximately 11.5 km. The signal of volcanic aerosol is less than in the previous occultation, probably due to dilution of the

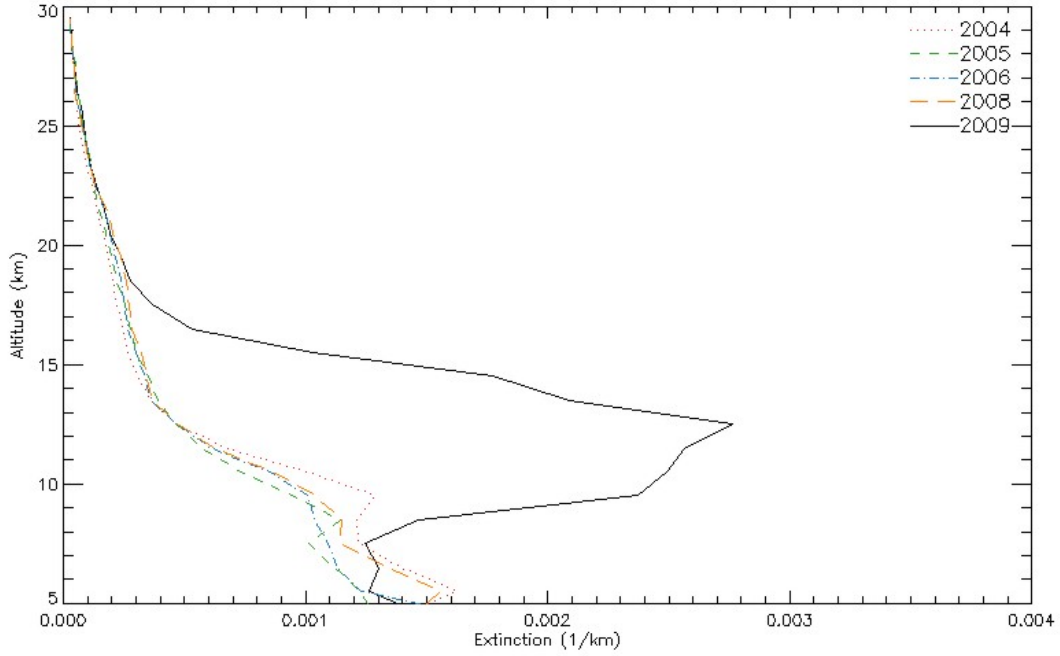

Figure 5.10: Median atmospheric extinction (NIR, v.2.2) in July from 2004 to 2009 in the NH. An enhanced layer can be seen in July 2009 between 8.5 km and 17.5 km, with maximum extinction of $b_{ext} = 0.0027\,\mathrm{km}^{-1}$ at approximately 13 km. July 2007 is excluded because the retrievals failed for this month.

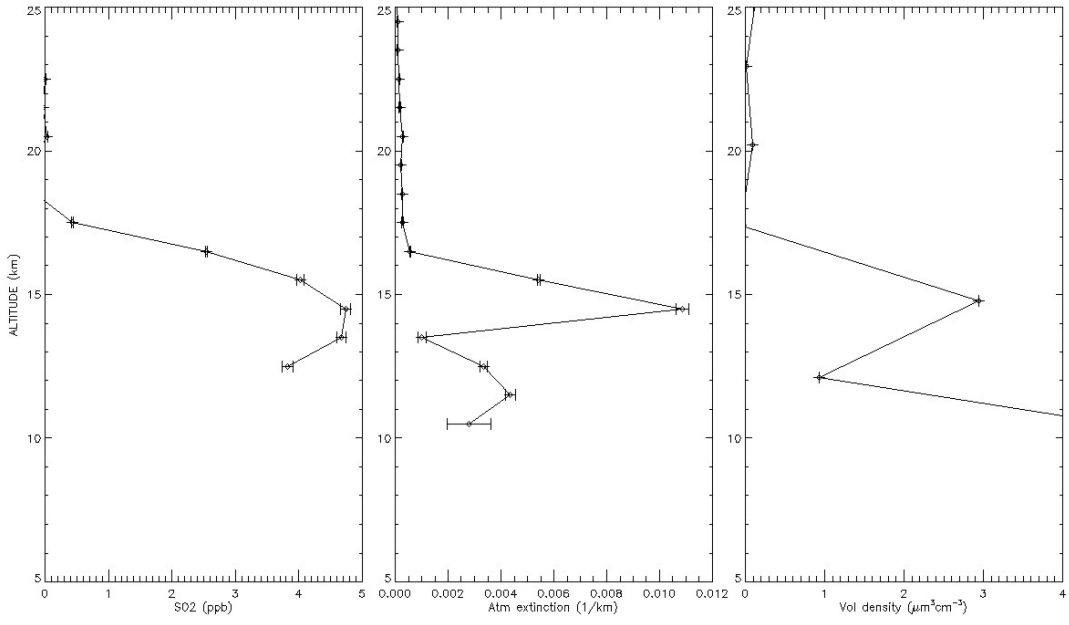

Figure 5.11: The SO_2 concentration profile in ppb, atmospheric extinction b_{ext} in km^{-1} (NIR, v.2.2) and the aerosol loading (in $\mu\mathrm{m}^3\mathrm{cm}^{-3}$) are illustrated for ss31868, which was detected on 14 July 2009 (68.31°N, 18.86°W). Note that the SO_2 and atmospheric extinction are on a 1 km altitude grid, but the aerosol retrieval is carried out for the spectra at the observed tangent height.

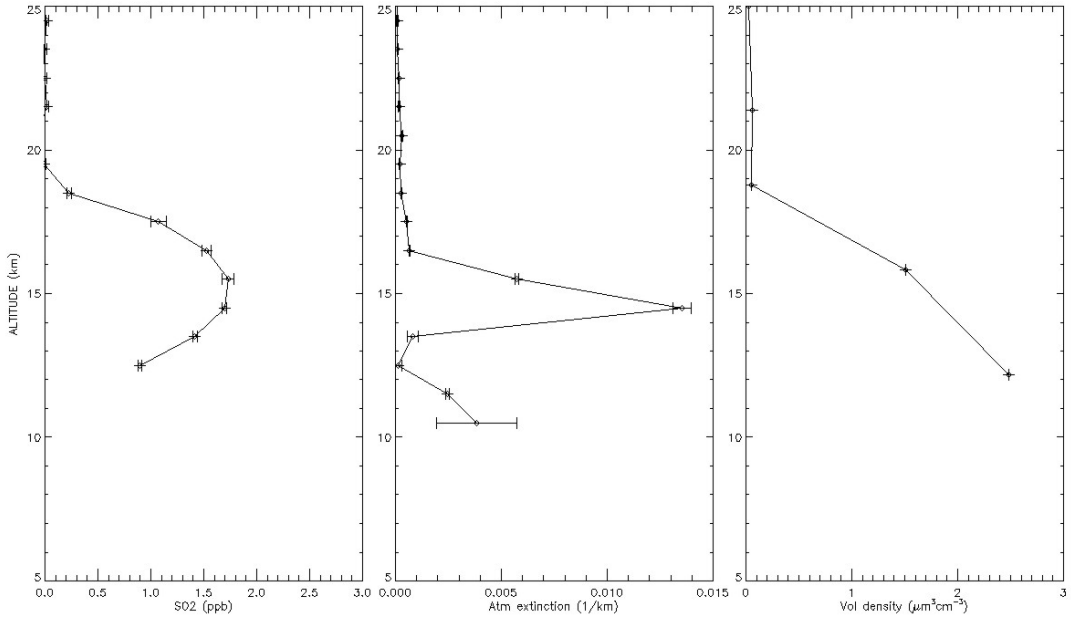

Figure 5.12: The SO_2 concentration profile in ppb, atmospheric extinction b_{ext} in km^{-1} (NIR, v.2.2) and the aerosol loading (in $\mu m^3 cm^{-3}$) are illustrated for ss31976, which was detected on 21 July 2009 (63.51°N, 176.37°W). Note that the SO_2 and atmospheric extinction are on a 1 km altitude grid, but the aerosol retrieval is carried out for the spectra at the observed tangent height.

plume. For ss31976 at 15 km, the maximum SO_2 concentration is almost 2 ppb, the maximum atmospheric extinction is 0.01 km^{-1} and an aerosol loading is 1.5 $\mu m\, cm^{-3}$. A very good agreement and consistency within the different retrievals from ACE data can be seen in these results for the analysis of the Sarychev volcanic eruptions.

In Figure 5.13 a profile of the atmospheric extinction (NIR) from an altitude of 5 km to 20 km for the Northern Hemisphere is illustrated for July 2009 with a resolution of 5° in latitude. A layer of enhanced atmospheric extinction is between 9.5 km and 17.5 km for latitudes between 50°N and 70°N with a median atmospheric extinction greater than 0.003 km^{-1}. A large enhancement of the extinction can be seen above the tropopause, which is symbolized by the black line. No influence of the volcanic plume can be seen for a latitude below 40°N and a small influence with an average atmospheric extinction of 0.002 km^{-1} occurs for a range between 40°N and 50°N.

A similar shape can be seen in Figure 5.14, which demonstrates the allocation of the median SO_2 concentration in the Northern Hemisphere in July 2009. A well-defined SO_2 layer is found between 12.5 km and 16.5 km from 55°N to 70°N. These two Figures (5.13 and 5.14) show the consist pattern of enhanced SO_2 and enhanced atmospheric extinction from the Sarychev volcanic plume.

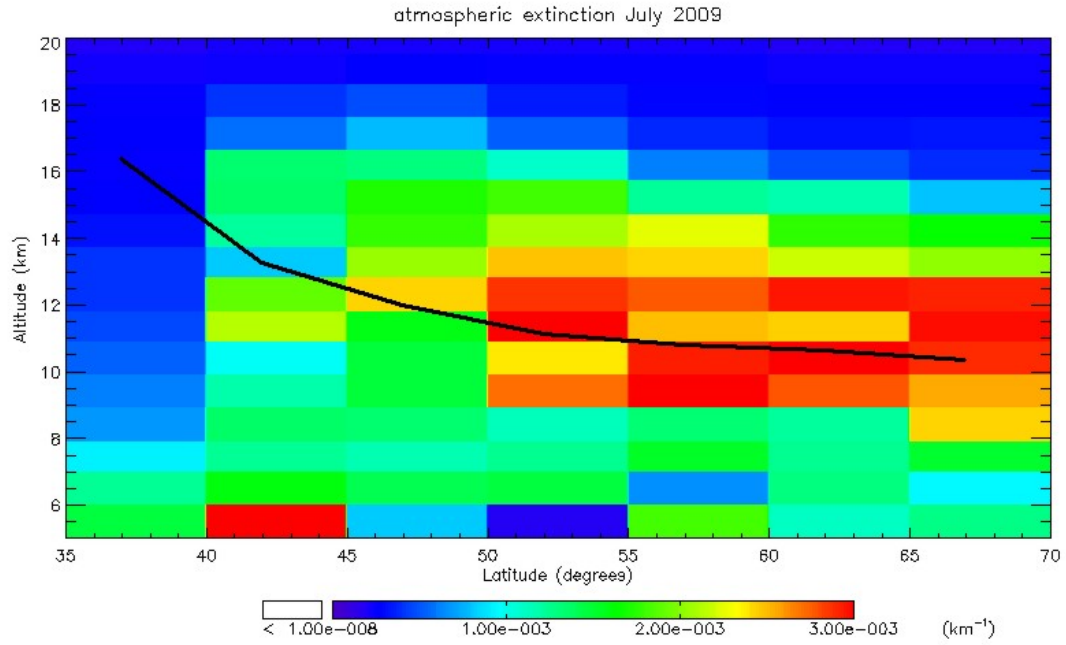

Figure 5.13: Profile of the median atmospheric extinction b_{ext} (km^{-1}) (NIR, v.2.2) in July 2009 in the NH, showing as clear, enhanced layer (red) between 55°N and 70°N. The median tropopause is shown as a black line.

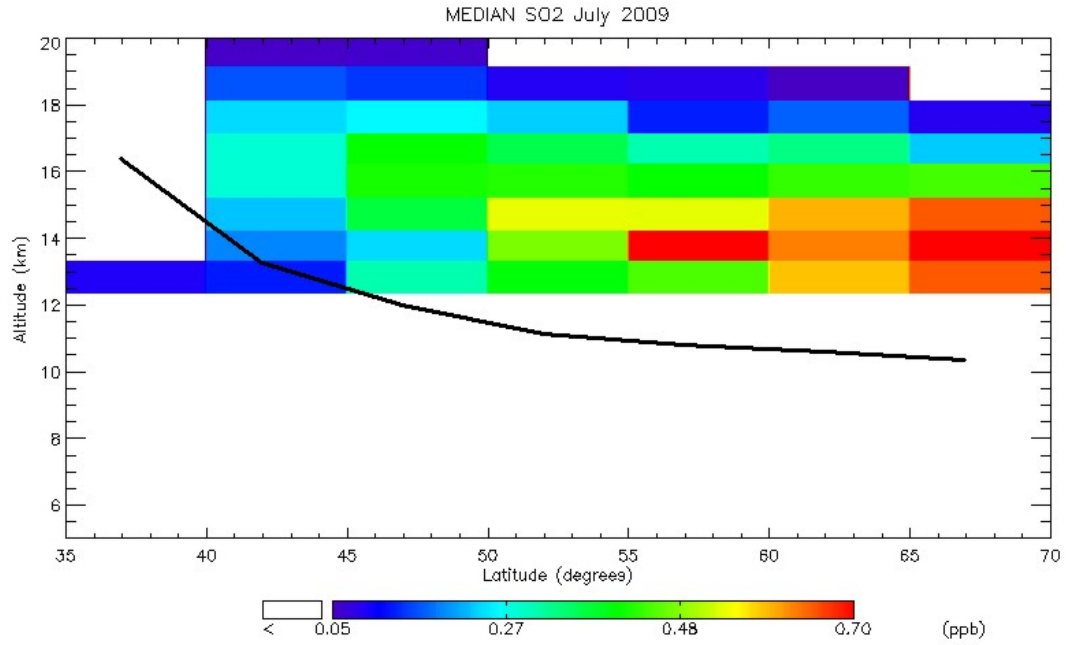

Figure 5.14: Profile of the median SO_2 concentration (ppb) in July 2009 in the NH, showing a clear, enhanced layer between 55°N and 70°N. The median tropopause is shown as a black line.

5.3. Observation of the temporal variation

As shown in Figure 4.4 the SO_2 concentration cannot be reliably measured two months after a major volcanic eruption. The temporal variation of the SO_2 concentration cannot be monitored because the time period (one month) is too short due to the low spatial resolution and the small number of occultations. However, the temporal variation of the enhancement in atmospheric extinction can be observed with NIR-Imager data from ACE.

5.3.1. On the example of Kasatochi

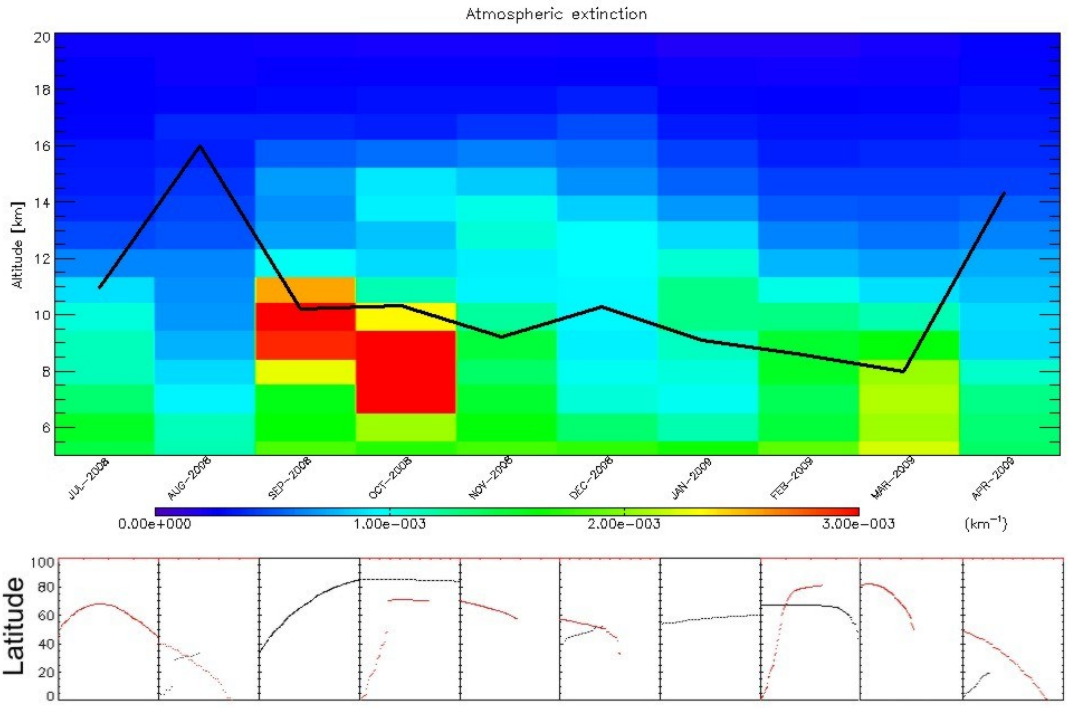

Figure 5.15: Time series of the monthly median atmospheric extinction (km^{-1}) (NIR, v.2.2) between July 2008 and April 2009 in the Northern Hemisphere. The lower panel shows the location (latitude in degrees), where the measurements were taken. The median tropopause is shown as a black line.

A time series of the median atmospheric extinction (NIR, v.2.2) in the Northern Hemisphere is plotted in Figure 5.15 for each month between July 2008 and April 2009. The lower panel demonstrates the location (latitude in degrees) of the measurements, showing that for August 2008 no measurements were taken above 40°N, therefore, the volcanic plume was not detected in August 2008 due to a transport time of a few months from the mid- latitudes to the tropics. The background or pre-Kasatochi conditions are represented by July 2008 due to the similar latitudinal coverage ($40 - 75$°N) as in September and October 2008. A very enhanced atmospheric extinction can be seen for September and October 2008, with a plume height of approximately 7 to 11 km and 6 to 10 km, respectively. In October 2008 the whole enhanced layer is below the tropopause (black solid line), where the plume was probably washed out completely by precipitation, therefore, from November 2008 onwards no strongly enhanced atmospheric extinction can be seen. However, there is also a slightly enhanced extinction layer in the stratosphere (light blue), with an upper limit of 16 km. This layer has a

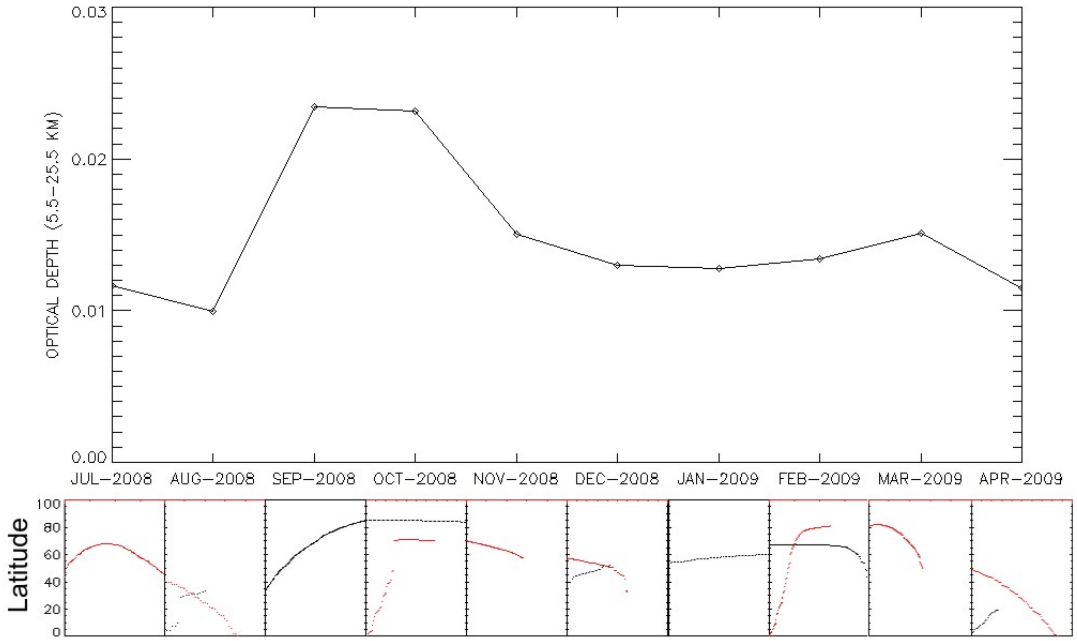

Figure 5.16: Monthly time series of the optical density τ (integrated median atmospheric extinction (NIR, v.2.2) between 5.5 km and 25.5 km) in the Northern Hemisphere between July 2008 and April 2009.

longer lifetime; even in March 2009 this enhanced extinction can still be seen and sinks about 0.5 km per month, while the layer in the troposphere (September and October 2008) sank $1\,\text{km} - 1.5\,\text{km}$ per month. In April 2009 pre-Kasatochi conditions, based on the atmospheric extinction retrieved by ACE NIR-imager, are recovered in the stratosphere as well as in the troposphere.

In Figure 5.16, the optical depth is plotted from July 2008 (background, pre-Kasatochi conditions) to April 2009. The pre-Kasatochi optical depth is approximately $\tau = 0.0012$ between 5.5 km and 25.5 km, which is approximately half of the optical depth observed in September 2008, where the optical depth τ reaches approximately 0.023. For October 2008 the optical depth remains strongly enhanced, caused by the volcanic plume in the high troposphere (see Figure 5.15). Between November 2008 and March 2009 the optical density is lowered to $\tau \approx 0.015$, but is still slightly enhanced compared to the pre-Kasatochi conditions resulting from the smaller plume in the stratosphere. In March 2009 the optical depth increases by approximately 0.002, compared to the previous month. The most likely explanation for this is the coagulation of the volcanic aerosol, which would increase the optical depth. This increase is , however, relatively small and could be due to the different latitudinal coverage in March 2009 compared to the previous months. Pre-Kasatochi conditions, based on the optical depth τ, can be found again in April 2009.

5.3.2. On the example of Sarychev

Figure 5.17 shows the temporal evolution of the median atmospheric extinction (NIR) in the Northern Hemisphere after the Sarychev eruptions. The lower panel shows the location of the occultations employed. Notice, that for August 2009 the occultations

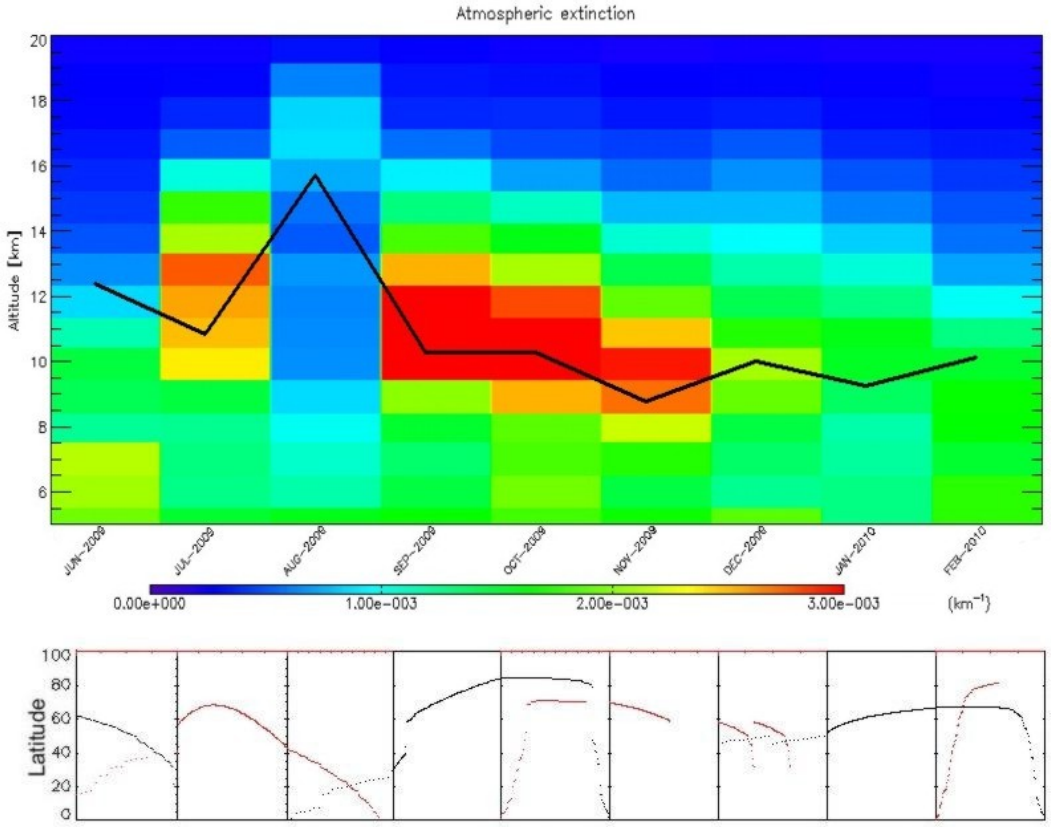

Figure 5.17: monthly time series of the median atmospheric extinction (km^{-1}) (NIR, v.2.2) between June 2009 and February 2010 in the Northern Hemisphere. The lower panel shows the location (latitude in degrees), where the measurements were taken. The median tropopause is shown as a black line.

are taken between 0°N and 40°N. Therefore, the Sarychev volcanic plume is not detected in August 2009 because of a relatively long transport time of the plume towards these latitudes. June 2009 does not contain any measurements of the Sarychev plume because there are only measurements taken before the eruptions, and June therefore, represents background extinction. Starting in July 2009 an enhanced layer of atmospheric extinction can be seen, which remains until February 2010, when background conditions are reached again. This enhanced layer can be seen in the upper troposphere and lower stratosphere (the black line symbolizes the median tropopause of each month) and descends approximately 1 km per month.

This evolution can also be confirmed by the average optical depth between 5.5 km and 25.5 km in altitude, shown in Figure 5.18. The optical depth in this altitude range has a background value of approximately 0.015, while it almost doubles the value of the normal condition in July and September. The optical depth decreases from November 2009 and reaches the pre-Sarychev conditions in February 2010. The reason for the increase in September and October 2009 is likely to be the coagulation of the volcanic aerosols, which would lead to a greater optical density.

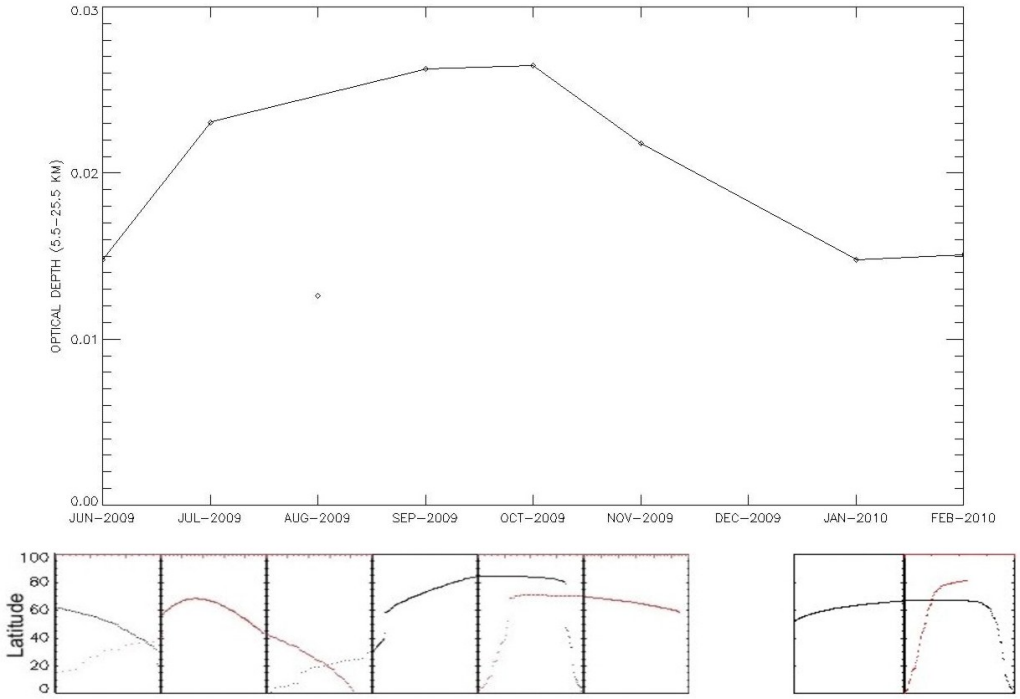

Figure 5.18: Time series of the optical density (integrated median atmospheric extinction (NIR, v.2.2) between 5.5 km and 25.5 km) in the Northern Hemisphere between June 2009 and February 2010.

5.4. Analysis of the size distribution and sulphate aerosol properties

5.4.1. The mean radius r_g and the geometric standard deviation σ

The geometric standard deviation σ of Pinatubo and El Chichón volcanic aerosols were analysed in *Massie et al.* (1996) and *Hofmann and Rosen* (1983). Their research resulted in a geometric standard deviation σ between 1.6 and 2.0 after the first month of a volcanic eruptions. Assuming that the Kasatochi and Sarychev sulphate aerosols have the similar properties, the σ value was fixed to 1.8 for our retrievals, while the parameters r_g, SC and W were derived by least-squares fitting (Program (1)).

Four different occultations with clear volcanic influence by Kasatochi (see Chapter 5.2) have been analysed for their sulphate aerosol properties. For the range of σ between 1.6 and 2.0, the mean radius r_g is in the range $0.023\,\mu\text{m} \leq r_g \leq 0.065\,\mu\text{m}$ (sr27216), $0.016\,\mu\text{m} \leq r_g \leq 0.043\,\mu\text{m}$ (sr27268) and $0.023\,\mu\text{m} \leq r_g \leq 0.061\,\mu\text{m}$ (sr27317). The low χ^2-values ($\chi^2 \approx 1$) of the retrievals indicates a very good correlation with the observed spectrum. These observations led to an approximate radius of $r_g \approx 0.04\,\mu\text{m}$ for the Kasatochi sulphate aerosol, three to four weeks after the volcanic eruptions.

In Table 2 the results of the mean radius r_g of the sulphate aerosol in the layer of the volcanic plume (displayed at approximately 18 km), assuming a geometric standard deviation between 1.6 and 2.0. The results show that with an increasing geometric standard deviation σ, the estimated radius r_g decreases. The χ^2-values, shown in Table 2, are less than 1, indicating an overestimation of the error in the observed continuum spectrum K_{meas}. However, the aerosol properties can be well retrieved, an example of the modelled spectrum compared to the observed spectrum can be seen in Figure 4.16 (see Chapter 4.3).

Table 2: Retrieved mean radius r_g for sulphate aerosol from the Kasatochi eruptions (August 2008) in the layer of the volcanic plume, at approximately 18 km.

	$\sigma = 1.6$		$\sigma = 1.8$		$\sigma = 2.0$	
Occultation	r_g [μm]	χ^2	r_g [μm]	χ^2	r_g [μm]	χ^2
sr27216	0.065 ± 0.010	0.59	0.042 ± 0.004	0.58	0.023 ± 0.003	0.58
sr27268	0.046 ± 0.008	0.65	0.027 ± 0.006	0.65	0.016 ± 0.004	0.65
sr27288	0.061 ± 0.013	0.34	0.040 ± 0.005	0.34	0.023 ± 0.003	0.34

The sulphate aerosol mean radius r_g from the Sarychev eruptions (July 2009), with the example of two occultations (ss31868: 14.07.2009, 68.31°N, 18.86°W and ss31976: 21.07.2009, 63.51°N, 176.37°W) is shown in Table 3. Assuming the same geometric standard deviation as mentioned above, the radius r_g results in $0.052\,\mu\text{m} \leq r_g \leq 0.130\,\mu\text{m}$ (ss31868) and $0.056\,\mu\text{m} \leq r_g \leq 0.143\,\mu\text{m}$ (ss31976) at about 15 km. Figure 4.16 (see Chapter 4.3 illustrates that the modelled aerosol spectrum for the mean geometric standard deviation $\sigma = 1.8$ reproduces the observed spectrum well and results, with the example of ss31868, in a $\chi^2 \approx 2.5$. A very similar radius with an average of $r_g \approx 0.09\,\mu\text{m}$ has been determined for the two occultations, for an approximately one month old Sarychev volcanic aerosol at the altitude of the aerosol layer at about 15 km. *Haywood et al.* (2010) have found a similar radius of $r_g \approx 0.095\,\mu\,\text{m}$ for the sulphate aerosols from the Sarychev eruptions which agrees with the here presented results very well. However (*Haywood et al.*, 2010) found this radius for a smaller geometric standard deviation of 1.4.

Table 3: Retrieved mean radius r_g for sulphate aerosol from the Sarychev eruptions (July 2009) in the layer of the volcanic plume, at approximately 15 km.

	$\sigma = 1.6$		$\sigma = 1.8$		$\sigma = 2.0$	
Occultation	r_g [μm]	χ^2	r_g [μm]	χ^2	r_g [μm]	χ^2
ss31868	0.130 ± 0.005	2.7	0.087 ± 0.014	2.6	$0.052 \pm \text{NaN}$	2.55
ss31976	0.143 ± 0.006	1.37	0.092 ± 0.025	1.37	0.056 ± 0.027	1.38

The error of the mean radius r_g varies between approximately 30 % and 10 %, relative to the retrieved radius. In most cases the retrieved radii for different geometric standard deviation σ within one occultation do not show agreement within their estimated errors, indicating that the geometric standard deviation has to be known to retrieve the radius of the aerosols accurately. Only a rough interval of the mean radius can be determined if the geometric standard deviation is not exactly known. With these examples, the radius r_g of the sulphate aerosol of Kasatochi is between $0.012\,\mu$m and $0.075\,\mu$m, and the radius r_g of Sarychev is between approximately $0.03\,\mu$m and $0.15\,\mu$m, for one month after the eruptions. For the Sarychev sulphate aerosol a marginal increase in the mean radius r_g can be seen between the two observed occultations, which were detected within a one week difference, which is possibly due to coagulation of the aerosol particles. However, this increase is minor compared to the estimated errors of the retrieved radii.

As discussed in Chapter 5.4.3, a more appropriate method is to combine the mean radius r_g and the geometric standard deviation σ to one variable, the so called effective radius R_{eff}. The retrievals of R_{eff} are more precise, when none of the two size distribution parameter is known.

5.4.2. Retrieved parameters and their correlation

The results for the aerosol volume slant column SC ($\mu m^3\,cm^{-3}\,km$), aerosol loading ($\mu m^3\,cm^{-3}$), composition W (%), mean aerosol radius r_g (μm) and the offset α retrieved with Program (1) are presented in Figures 5.19 to 5.21, assuming a geometric standard deviation of $\sigma = 1.8$, for the six previously mentioned occultations, influenced by Kasatochi or Sarychev.

The results of this analysis show that the mean radius can only be retrieved in the layer of the volcanic plume, where the aerosol loading reaches a certain amount. For sr27216, with an aerosol volume slant column $SC \approx 300\,\mu m^3\,cm^{-3}\,km$ and a corresponding aerosol loading of $V \approx 1.0\,\mu m^3\,cm^{-3}$, the radius r_g has been retrieved, however, for sr27317 with an aerosol volume slant column $SC \approx 360\,\mu m^3\,cm^{-3}\,km$ and a corresponding aerosol loading of $V \approx 1.1\,\mu m^3\,cm^{-3}$, the radius r_g could not be retrieved. The retrieval of the radius r_g seems to be not only connected to the volume of aerosol present, but also at which altitude the aerosol is present. The retrieval for sr27216 has been made at an altitude of about 18.4 km, while the retrieval of the occultation sr27317 has been determined at 17.72 km. For the sulphate aerosol from the Sarychev eruptions, where the aerosol layer was much lower, at approximately 15 km, the minimum required aerosol volume slant column seems to be around $SC \approx 500\,\mu m^3\,cm^{-3}\,km$ with a corresponding aerosol loading of $V \approx 1.5\,\mu m^3\,cm^{-3}$. This indicates that the minimum aerosol loading required for a successful retrieval of the mean radius r_g seems to be connected to the height of the aerosol layer. At 18 km the aerosol loading must be just over $1.0\,\mu m^3\,cm^{-3}$, while at 15 km the aerosol loading must be approximately $1.5\,\mu m^3\,cm^{-3}$.

The offset due to the linearity of the ACE detector should be $\alpha \approx 1$, which is the case, as shown for background retrievals in Chapter 4.3.3. In the results from Figure 5.19 to Figure 5.21, the retrieved offsets α sometimes differ from 1. This can be seen mainly in or below the layer of the enhanced aerosol. An offset $\alpha < 1$ is possibly due to the absorption and scattering in the plume caused by ash or other particles, decreasing the transmission value in the observed spectrum K_{meas}. This kind of extinction is not included in the modelled spectrum, but can be adjusted by the offset α.

The results from Figure 5.19 to Figure 5.21 also show that the χ^2-value increases towards low altitudes. At high altitudes, up to approximately 15 km χ^2 is close to 1, representing a good retrieval, below 15 km χ^2 starts to increase to almost 30 for all observed cases, indicating that the retrieval does not match the observed spectrum. The reason for this phenomenon is most likely the stronger absorption and scattering of other particles and trace gases because of a higher concentration in lower altitudes, which are not included in the forward model for the determination of K_{meas}. The observed continuum spectrum K_{meas} also show much a much higher noise the lower the altitude of the observation is.

The sulphate aerosol loading is approximately $1.0\,\mu m\,cm^{-3}$ for all observed occultations after the Kasatochi eruptions, presented in Figure 5.19 and Figure 5.20. Therefore a

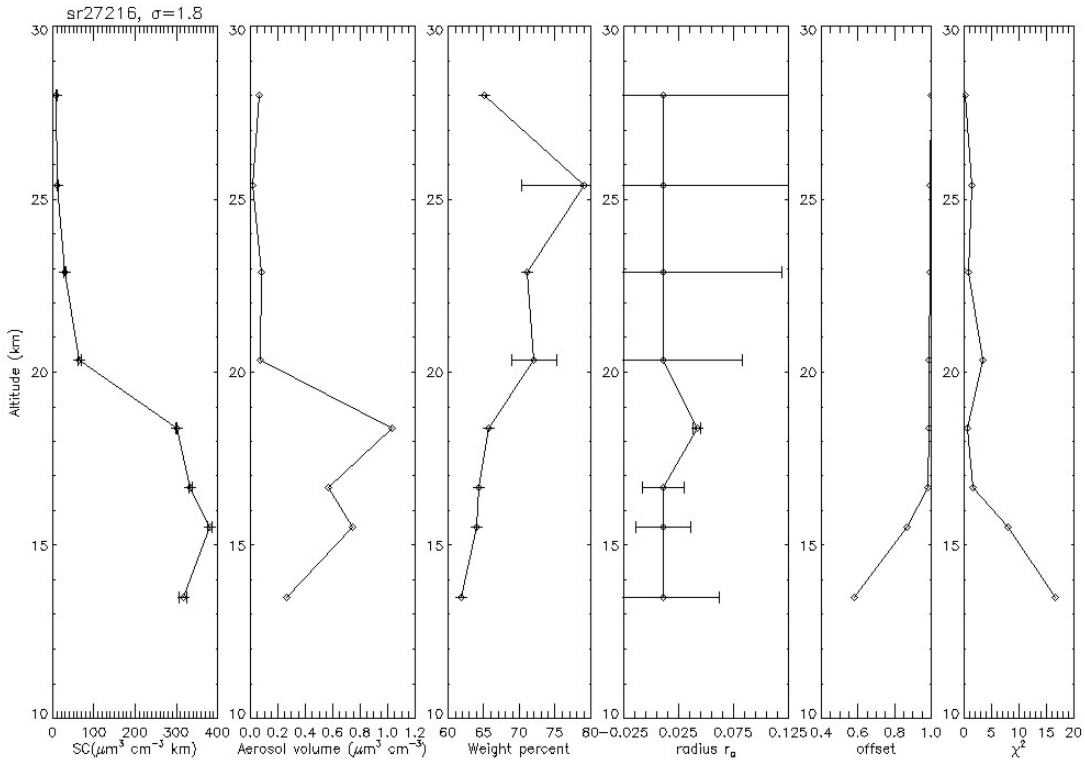

(a) sr27216 (01.09.2008, 35.27°N, 84.07°W)

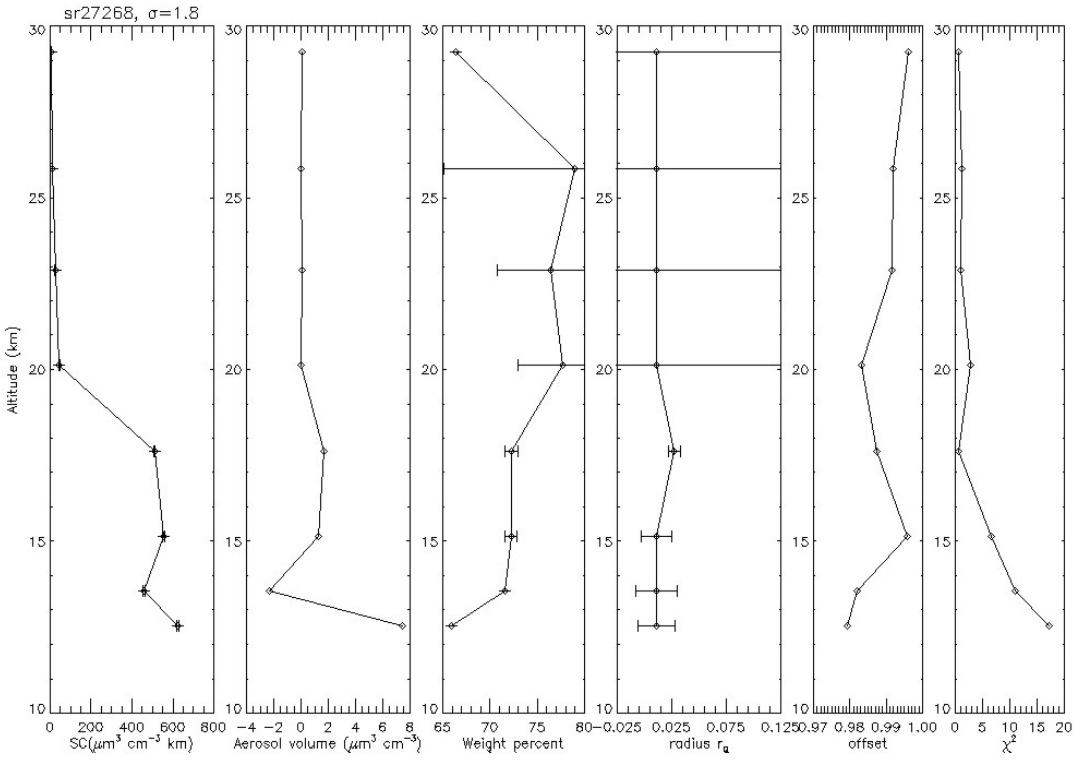

(b) sr27268 (04.09.2008, 47.58°N, 83.30°E)

Figure 5.19: Retrieved aerosol properties for sr27216 and sr27268. Shown are the aerosol SC (μm^3 cm^{-3} km), the aerosol loading (μm^3 cm^{-3}), W (%), r_g (μm), the offset α and χ^2.

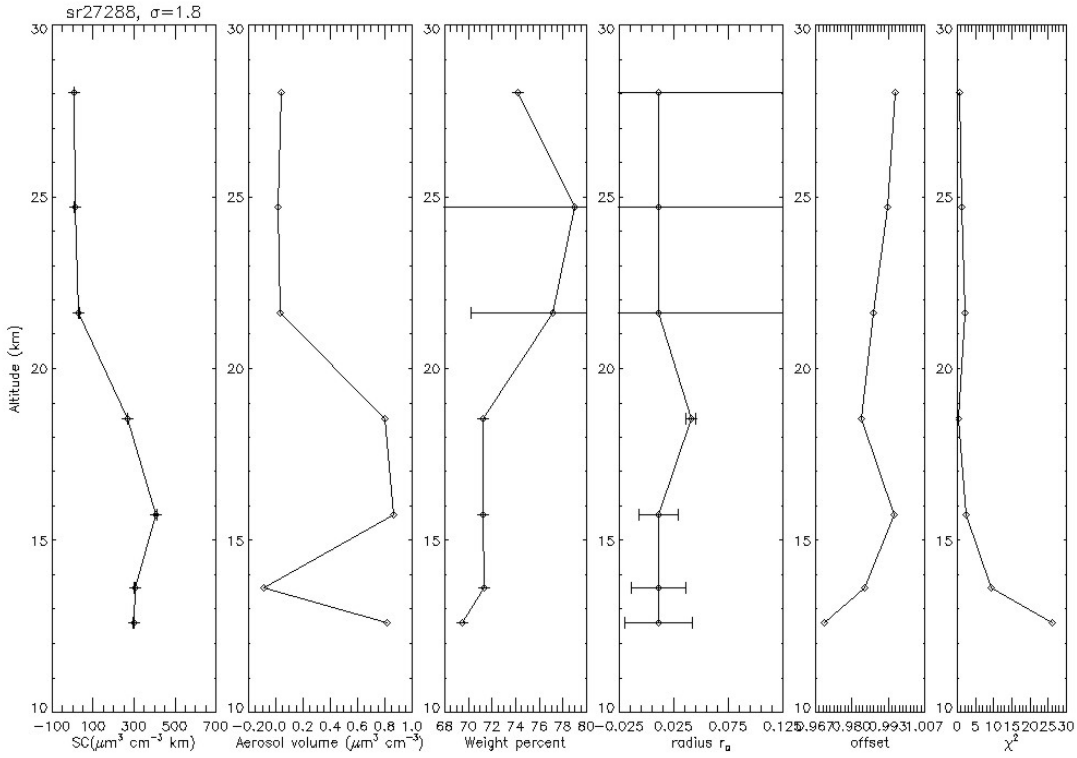

(a) sr27288 (06.09.2008, 51.48°N, 45.92°W)

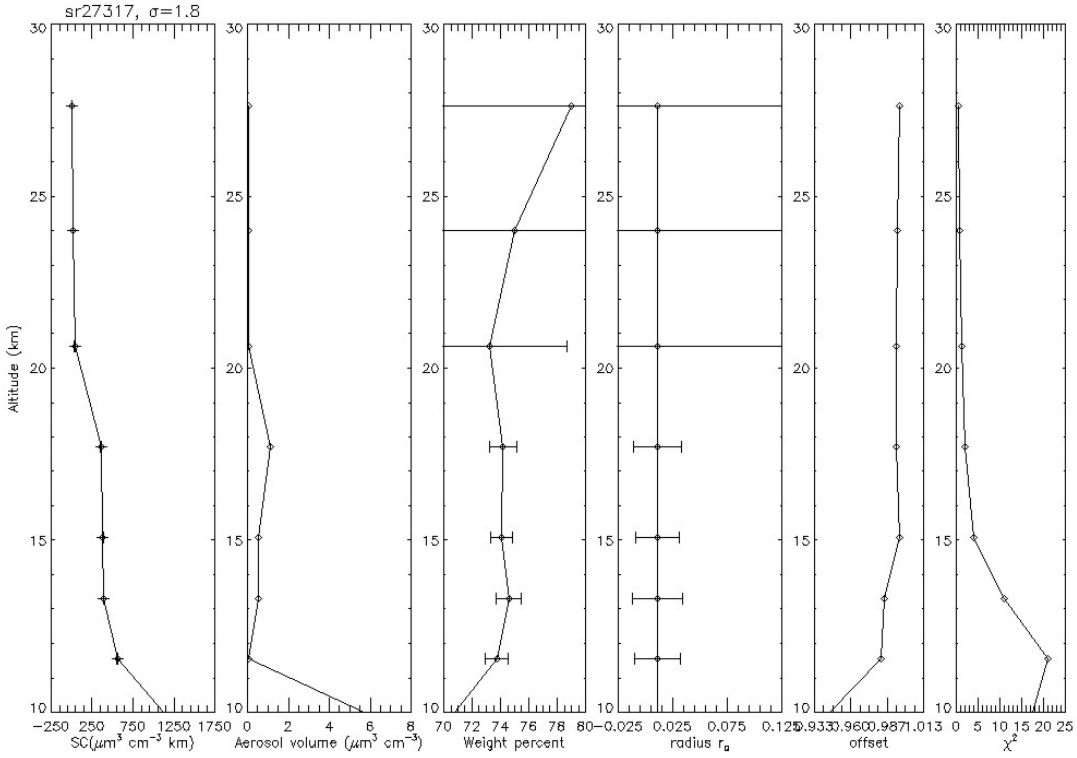

(b) sr27317 (08.09.2008, 56.51°N, 35.07°W)

Figure 5.20: Retrieved aerosol properties for sr27288 and sr27317. Shown is the aerosol SC (μm^3 cm^{-3} km), the aerosol loading (μm^3 cm^{-3}), W (%), r_g (μm), the offset α and χ^2.

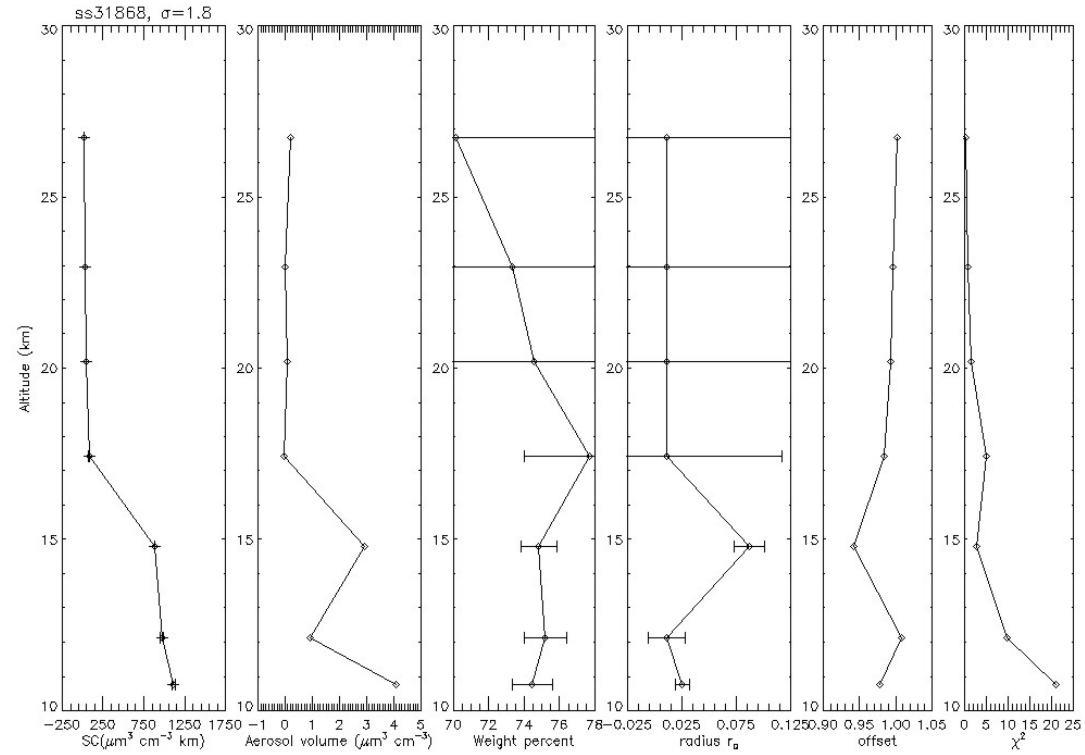

(a) ss31868 (14.07.2009, 68.31°N, 18.86°W)

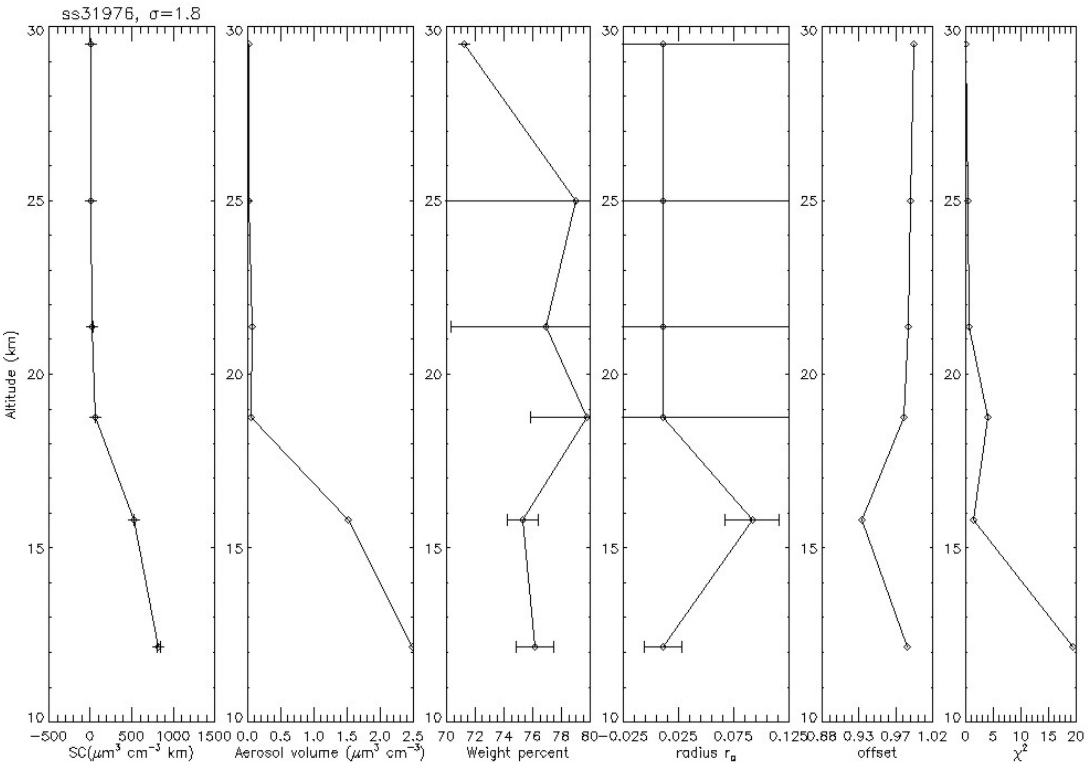

(b) ss31976 (21.07.2009, 63.51°N, 176.37°W)

Figure 5.21: Retrieved aerosol properties for ss31868 and ss31976. Shown are the aerosol SC (μm^3 cm^{-3} km), the aerosol loading (μm^3 cm^{-3}), W (%), r_g (μm), the offset α and χ^2.

dilution could not be seen within a temporal interval of one week, according to the sulphate aerosol volume density. The reason for the quite similar aerosol loading within one week is most likely the different localisations of the analysed occultations, and an irregular spreading of the plume over the globe. The composition of the sulphate aerosol increases from 65 % to 74 % acid-water solution during one week.

A possible dilution of the volcanic plume has been observed, according to a decreasing aerosol slant column and volume density, between the occultations ss31868 and ss31976, which was detected one week later, at an altitude of approximately 15 km. The volume slant column SC at this altitude reaches $SC = 879.23 \pm 2.48\,\mu\text{m}\,\text{cm}^{-3}\,\text{km}$ (ss31868) and $SC = 527.09 \pm 1.69\,\mu\text{m}\,\text{cm}^{-3}\,\text{km}$ (ss31976). For the plume height ($\sim 15\,\text{km}$) a composition of $W = 74.83 \pm 0.03\,\%$ (ss31868) and $W = 75.33 \pm 0.06\,\%$ (ss31976) sulphuric acid-water solution is retrieved and the radius reaches $r_g = 0.087 \pm 0.014\,\mu\text{m}$ and $r_g = 0.092 \pm 0.025\,\mu\text{m}$, respectively.

The statistical precision for the aerosol slant column SC, as well as for the composition W with an error of less than 0.5 % and 1.5 %, respectively, is quite high. The surprisingly small statistical error for SC and W is probably due to the large number of channels employed at which the transmission is recorded. For many altitudes the radius r_g cannot be derived because the aerosol signal is marginal and only for a height with a relatively high aerosol loading. The radius can be derived with the least-squares fitting algorithm. This height almost always corresponds to the altitude with maximum aerosol extinction. In the case of a low aerosol presence, the radius r_g is set to a value of $r_g = 0.011\,\mu\text{m}$.

5.4.3. Retrieval of the effective radius R_{eff}

As previously mentioned σ and r_g cannot be retrieved at the same time using only ACE infrared spectra and only one parameter can be derived with our method, while the other aerosol size parameter is fixed. For the analysis presented from Figure 5.22 to Figure 5.25, Program (2) (see Chapter 4.3.1) is used, where r_g and σ are fixed and the aerosol slant column SC, composition W, offset α and χ^2-values for the best fit are retrieved for a wide range of radii $0.01\,\mu\text{m} \leq r_g \leq 1.28\,\mu\text{m}$ in steps of $0.01\,\mu\text{m}$ and geometric standard deviations $1.2 \leq \sigma \leq 2.5$ in steps of 0.1. This analysis has been done for four occultations influenced by the Kasatochi volcano ((a) sr27216, (b) sr27268, (c) sr27288 and (d) sr27317) and two occultations influenced by Sarychev ((e) ss31868 and (f) ss31976).

In Figure 5.22 the χ^2-values are shown as a contour as a function of r_g and σ, showing on the contour many combinations of r_g and σ with a minimum χ^2. The minimum χ^2-values for the Kasatochi sulphate aerosols can be found in a wide, open band, running from an r_g of about 0.2 μm and a σ of 1.2 to an r_g of 0.01 μm at $\sigma = 2.5$, illustrated in Figure 5.22 (a) to (d). In the analysis of the sulphate aerosol caused by the Sarychev eruptions, minimum χ^2-values can be found in a wide enclosed diagonal band, running from an r_g of almost 0.3 μm and a σ of 1.2 to an r_g of 0.02 μm at $\sigma = 2.5$. The actual error of a combination between r_g and σ cannot be retrieved, but the Figure 5.22 shows the sensitivity of both parameters. Nevertheless, the change of SC and W for different possible combinations of r_g and σ inside the minimum χ^2-band is negligible, as the aerosol SC and the composition remains equal or quite similar within this band, as demonstrated in Figure 5.23 and Figure 5.24.

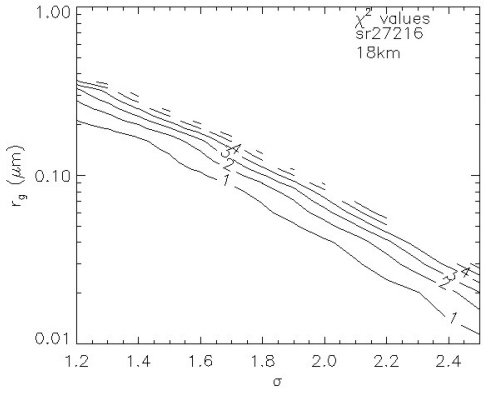

(a) χ^2-values for sr27216 at 18.380 km.

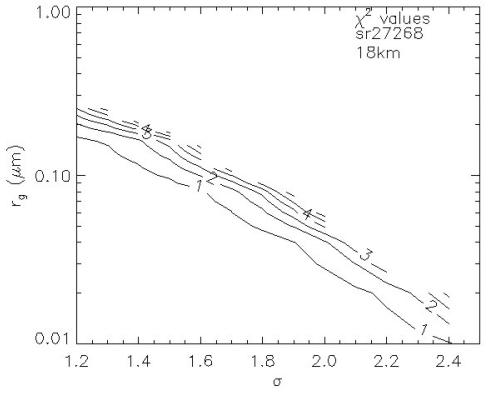

(b) χ^2-values for sr27268 at 17.611 km.

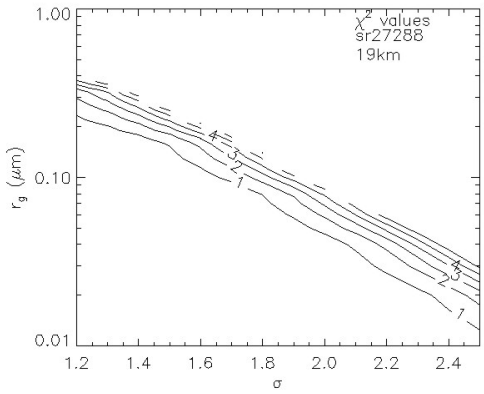

(c) χ^2-values for sr27288 at 18.547 km.

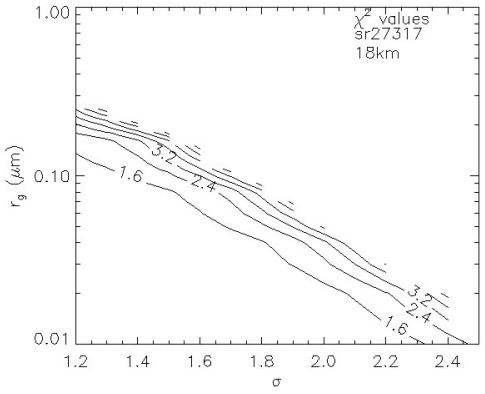

(d) χ^2-values for sr27317 at 17.722 km.

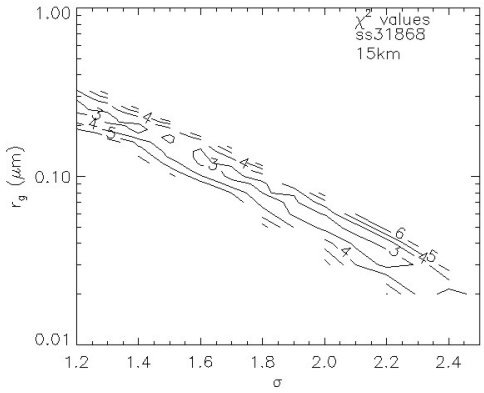

(e) χ^2-values for ss31868 at 14.784 km.

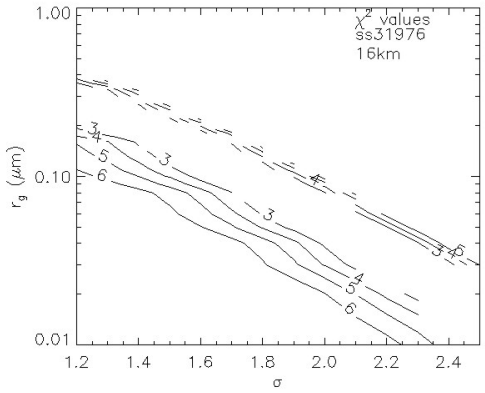

(f) χ^2-values for ss31976 at 15.815 km.

Figure 5.22: Retrieved χ^2-values as a contour plot of r_g and σ for four continuum spectra, influenced by the Kasatochi volcano: (a) sr27216, (b) sr27268, (c) sr27288 and (d) sr27317, at the height of the maximum aerosol signature, at approximately 18 km.

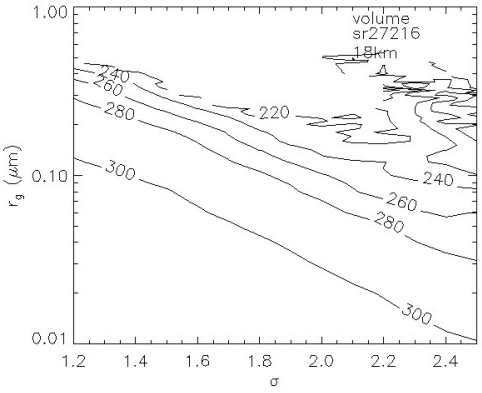

(a) *SC*-values for sr27216 at 18.380 km.

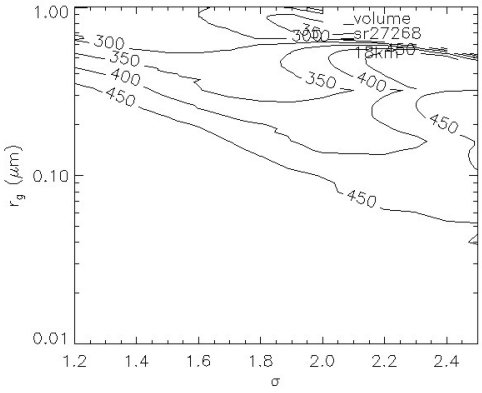

(b) *SC*-values for sr27268 at 17.611 km.

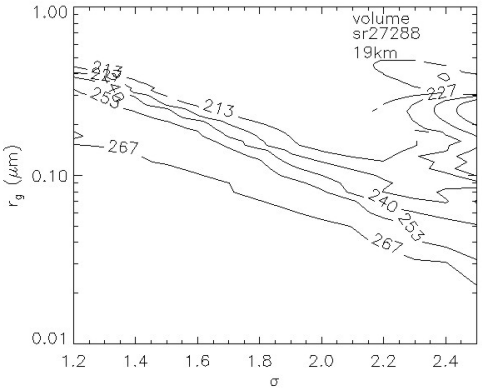

(c) *SC*-values for sr27288 at 18.547 km.

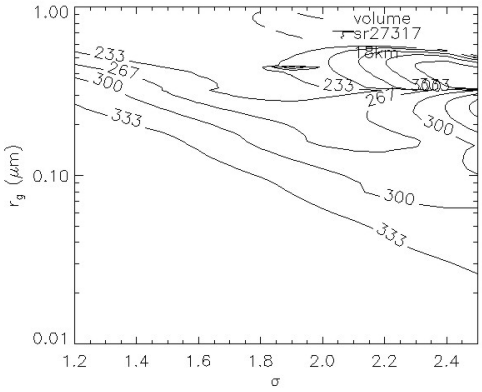

(d) *SC*-values for sr27317 at 17.722 km.

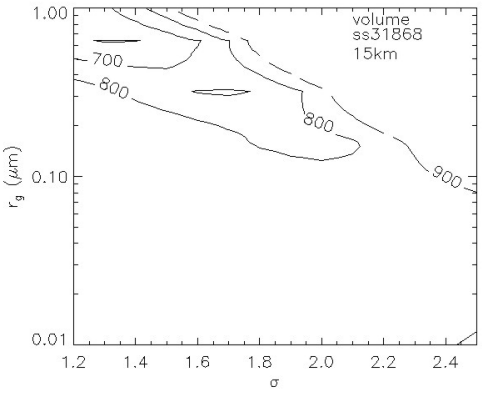

(e) *SC*-values for ss31868 at 14.784 km.

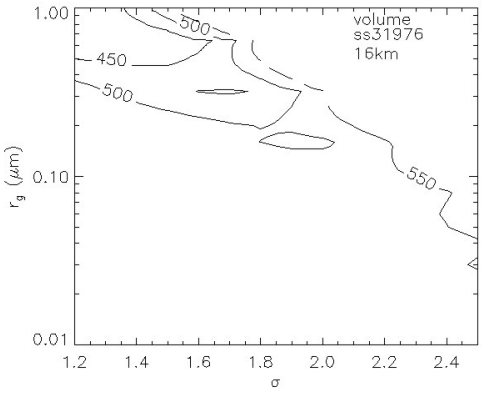

(f) *SC*-values for ss31976 at 15.815 km.

Figure 5.23: Retrieved *SC*-values ($\mu m^3\,cm^{-3}\,km$) as a contour plot of r_g and σ for four continuum spectra, influenced by the Kasatochi volcano: (a) sr27216, (b) sr27268, (c) sr27288 and (d) sr27317, at the height of the maximum aerosol signature, at approximately 18 km.

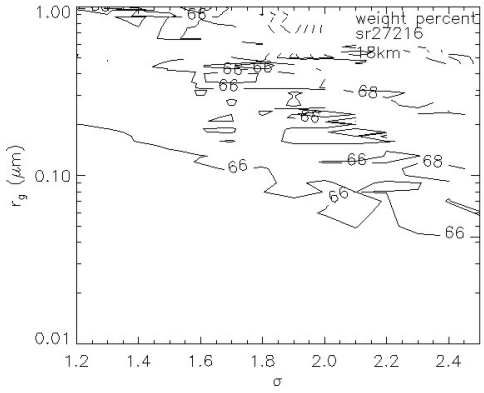

(a) Composition for sr27216 at 18.380 km.

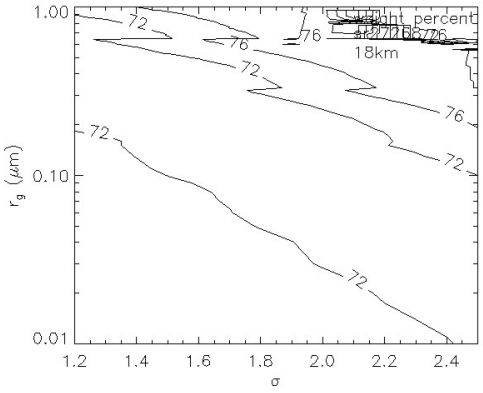

(b) Composition for sr27268 at 17.611 km.

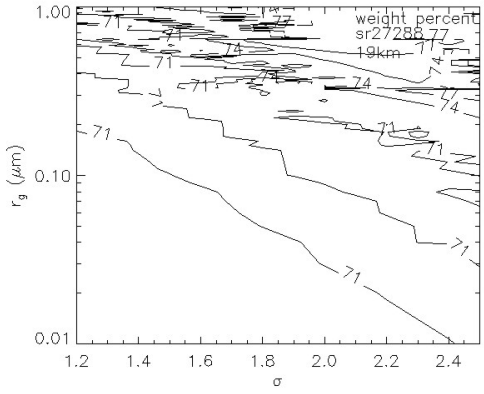

(c) Composition for sr27288 at 18.547 km.

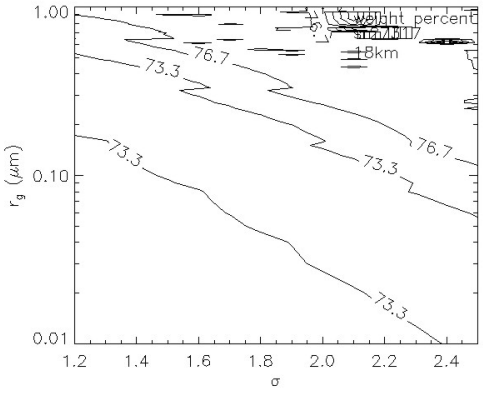

(d) Composition for sr27317 at 17.722 km.

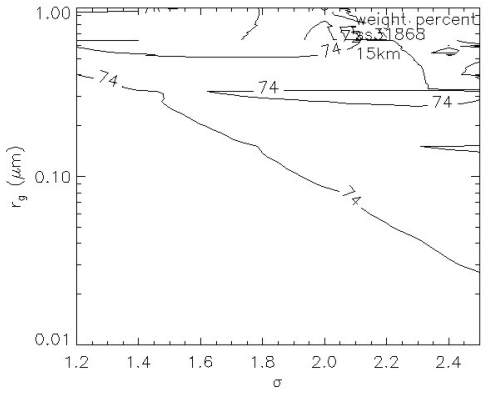

(e) Composition for ss31868 at 14.784 km.

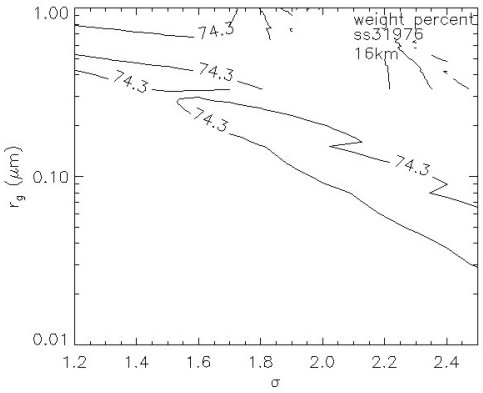

(f) Composition for ss31976 at 15.815 km.

Figure 5.24: Retrieved composition W (%) as a contour plot of r_g and σ for four continuum spectra, influenced by the Kasatochi volcano: (a) sr27216, (b) sr27268, (c) sr27288 and (d) sr27317, at the height of the maximum aerosol signature, at approximately 18 km.

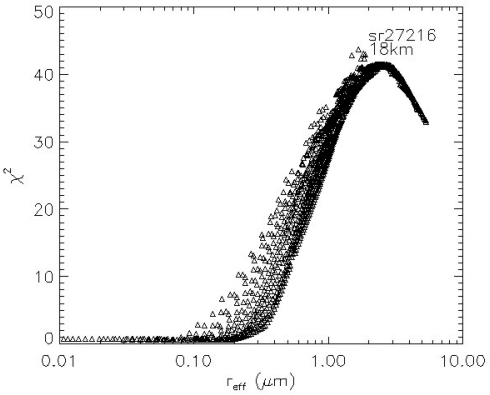

(a) sr27216 at 18.380 km.

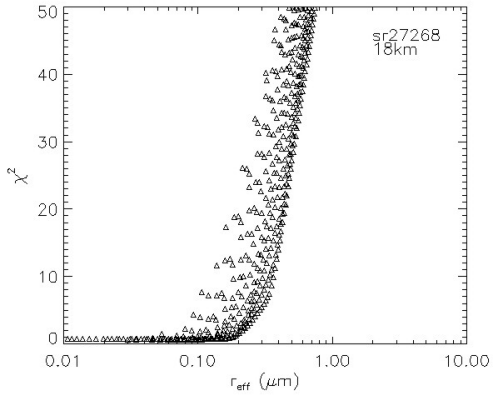

(b) sr27268 at 17.611 km.

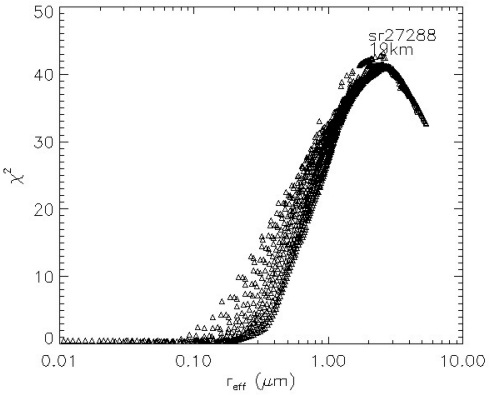

(c) sr27288 at 18.547 km.

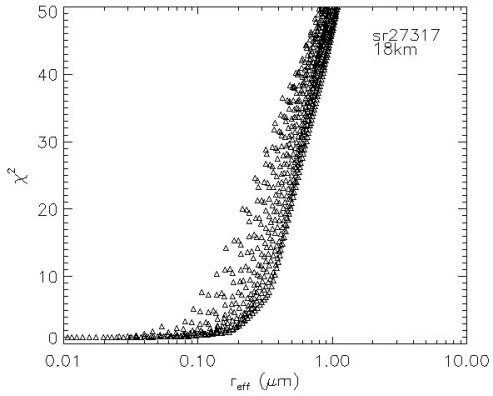

(d) sr27317 at 17.722 km.

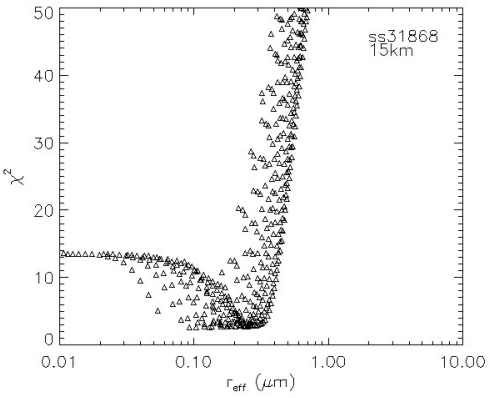

(e) ss31868 at 14.784 km.

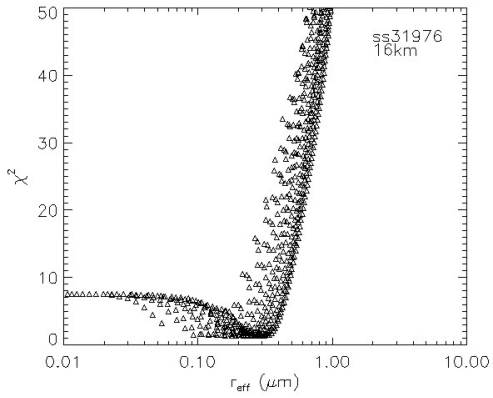

(f) ss31976 at 15.815 km.

Figure 5.25: Retrieved χ^2 as a function of R_{eff} (μm) for four continuum spectra, influenced by the Kasatochi volcano: (a) sr27216, (b) sr27268, (c) sr27288 and (d) sr27317, at the height of the maximum aerosol signature, at approximately 18 km.

Without knowing the exact geometric standard deviation σ of the sulphate aerosol, the radius r_g can only be retrieved vague, however, the method presented in this thesis, can be used to derive and analyse the approximate effective radius, given by Equation 5 (see Chapter 2.2.2) (*Steele et al.*, 2003) to a high degree of precision. R_{eff} is shown in Figure 5.25 and plotted against χ^2. Figure 5.25 (a) to (d) show the minimum χ^2-values from the Kasatochi eruptions. The best-fitting effective radius R_{eff} is in all four cases below $0.2\,\mu$m for – approximately three to four weeks old sulphate aerosol. The results for the sulphate aerosol resulting from the Sarychev eruptions are presented in Figure 5.25 (e) and (f). The minimum χ^2-values occur for an R_{eff} between 0.1 and 0.3 μm in both analysed measurements. The effective radius has been analysed in many other studies of volcanic aerosols and has led to a value of R_{eff} of $0.1-0.2\,\mu$m for the Kasatochi and Pinatubo volcanoes almost one month after the eruptions (*Mattis et al.*, 2010; *Ansmann et al.*, 1997). This is in good agreement with our calculation of the effective radius R_{eff} of sulphate aerosol, occurring one month after the volcanic eruptions.

The long term behaviour of R_{eff} of volcanic aerosol (e.g. for Pinatubo (*Massie et al.*, 1996; *Ansmann et al.*, 1997; *Pueschel et al.*, 1994) and El Chichón (*Hofmann and Rosen*, 1983)) shows that the effective radius starts increasing with time directly after the volcanic eruptions. A second radius mode, $r_{g,2} \approx 1\,\mu$m (*Hofmann and Rosen*, 1983; *Massie et al.*, 1996) appears approximately two months after the eruptions due to coagulation of the aerosol particles. The very small particles ($r_g \leq 0.05\,\mu$m) disappear after a few months as a result of the accretion on other particles (*Hofmann and Rosen*, 1983). Approximately six months after the Pinatubo eruptions the effective radius started to decrease slowly (*Ansmann et al.*, 1997). This evolution of the aerosol size distribution cannot be seen in our measurements due to the lack of occultations with a high volcanic aerosol signature from the volcanic plume at a later state.

In our analyses of the aerosol size distribution, the aerosol loading is extremely weak after the first month of the volcanic eruptions of Kasatochi and Sarychev. An analysis of the radius r_g and geometric standard deviation σ with the method presented in this study. The threshold aerosol loading is not reached two months after the volcanic eruptions of Kasatochi and Sarychev, a precise fitting correlation between the modelled and the observed spectrum is no longer possible. There is no evidence that the effective radius increases over time for the Kasatochi sulphate aerosol because the occultations, analysed for the radius, have a temporal difference of less than one week, wherefore the effect is marginal compared to the estimated errors. In July 2009 between the first and the second presented observations, the calculated radii, increase slightly from $0.052\,\mu\text{m} \leq r_g \leq 0.13\,\mu$m (ss31868) to $0.056\,\mu\text{m} \leq r_g \leq 0.14\,\mu$m (ss31976). This increase, however, is relatively small and within the estimated errors, for an observation within a one week temporal difference. The only reliable evidence of the increase in the particle size can be seen in the increase of the optical density (Figure 5.18 in Chapter 5.3) after the Sarychev volcanic eruptions until October 2009 (four months after the eruption). After this point the optical density starts decreasing until in February 2010 normal pre-Sarychev conditions are reached again. In the case of the Kasatochi aerosol, there is a very small increase of the optical depth (Figure 5.16) from February 2009 to March 2009, seven months after the eruptions, however, this increase is very small and is possibly due to other reasons.

5.5. Influence of cirrus clouds

The observed occultations here have been analysed for the presence of cirrus cloud, including the extinction spectrum β_{ice} of ice particles in Equation 22 (Chapter 4.3.1). With the optical constants taken from *Clapp et al.* (1995), the extinction spectrum β_{ice} has been calculated with AXE for a typical cirrus cloud ice particle with a radius $r_g = 2.5\,\mu$m and a width $\sigma = 1.8$ (*Yang et al.*, 1997). The extinction spectrum and the transmission spectrum for an aerosol volume $SC = 500\,\mu\text{m}^3\,\text{cm}^{-3}\,\text{km}$ of ice particles at 215 K is shown in Figure 5.26. The transmission spectrum in Figure 5.26 (b) shows relatively weak absorption lines, with the strongest absorption and scattering between 1250 cm^{-1} and 3250 cm^{-1}, however, without a significant shape, which makes the analysis of cirrus clouds for a spectrum between 800 cm^{-1} and 4100 cm^{-1} difficult.

In Figure 5.27, two examples of the analysis of the presence of cirrus clouds are presented, showing that the residuum does not lead to a better result with the insertion of the extinction spectrum of ice particles. In these graphs, three different transmission spectra are plotted; the observed transmission spectrum K_{meas} (black), the modelled transmission spectrum with only the absorption of sulphuric acid aerosol K_{model} (red) and the modelled transmission with both the sulphuric acid and ice aerosols K_{combo} (blue). In the small graph below, the residuum is presented in black for the K_{model}-fit and in blue for the K_{combo}-fit. The first example in Figure 5.27 (a) shows the occultation sr27216 as an example for the aerosols caused by the Kasatochi's eruptions. The calculated aerosol volume slant column of the ice particles results in $SC_{ice} \approx 222\,\mu\text{m}^3\,\text{cm}^{-3}\,\text{km}$, however the modelled spectrum has declined, with the combination of the absorption from sulphate aerosol and ice particles. The fitting on the observed spectrum fails, especially between 2000 cm^{-1} and 3300 cm^{-1}, where the transmission is much smaller than in the observed one. The second example (Figure 5.27 (b)) shows a negative concentration of ice particles. The results of this and analysis of other (here presented) measurements lead to the conclusion that in all observed cases no signature of absorption due to ice was found. The formation of cirrus clouds caused by the volcanic aerosols from the Kasatochi and Sarychev eruptions could not be observed in this study.

5.6. Effect on the temperature in the volcanic plume

As previously mentioned (Chapter 1), the temperature due to absorption of IR radiation increases in a layer with enhanced aerosol loading (*Pollack et al.*, 1976). A temperature increase mainly occurs in the first few months after a volcanic eruption, when there are still larger dust and ash particles, which absorb infrared radiation from the terrestrial radiation. An approximate mode of a radius of $1\,\mu$m leads to a maximum warming, according to *Pollack et al.* (1976). The normal, unperturbed temperature profile of the atmosphere is illustrated in Figure 2.1, where the temperature decreases linearly in the troposphere, is constant in the tropopause and decreases linearly in the stratosphere with altitude. Temperature enhancements in this profile can be associated with a large concentration of particles, which absorb IR radiation. This phenomenon will be discussed in this section using the previously analysed occultations, influenced by a volcanic plume and containing a clear layer with an enhanced aerosol concentration.

Figure 5.28 shows the temperature profile of two occultations influenced by the Kasatochi (Figure 5.28 (a)) and the Sarychev (Figure 5.28 (b)) eruptions, respectively. The occultation sr27268 has a maximum aerosol loading of $V \approx 1.8\,\mu\text{m}^3\text{cm}^{-3}$ at 17.5 km,

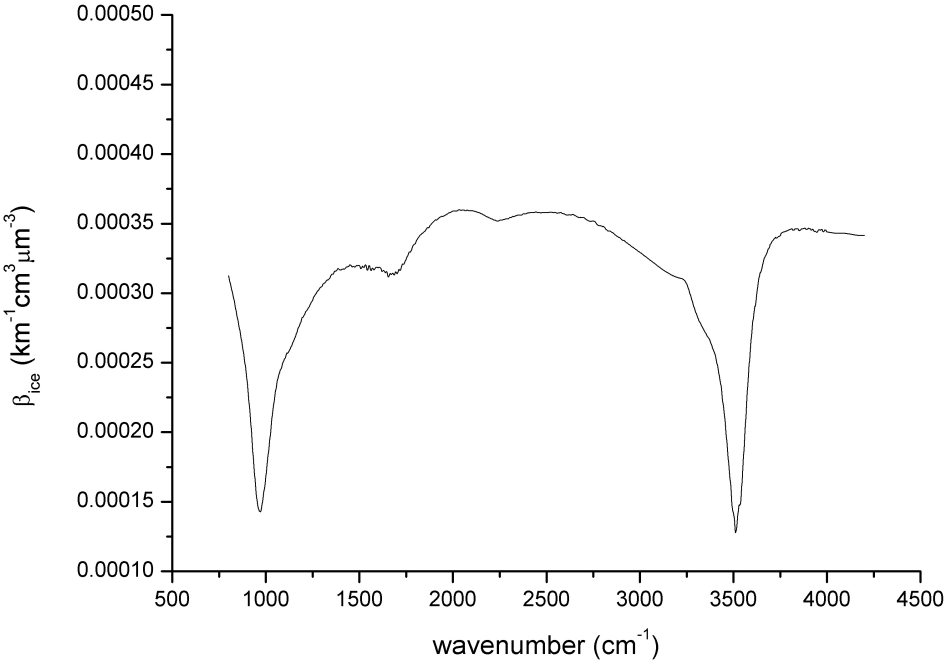

(a) The extinction β_{ice} of an ice particle

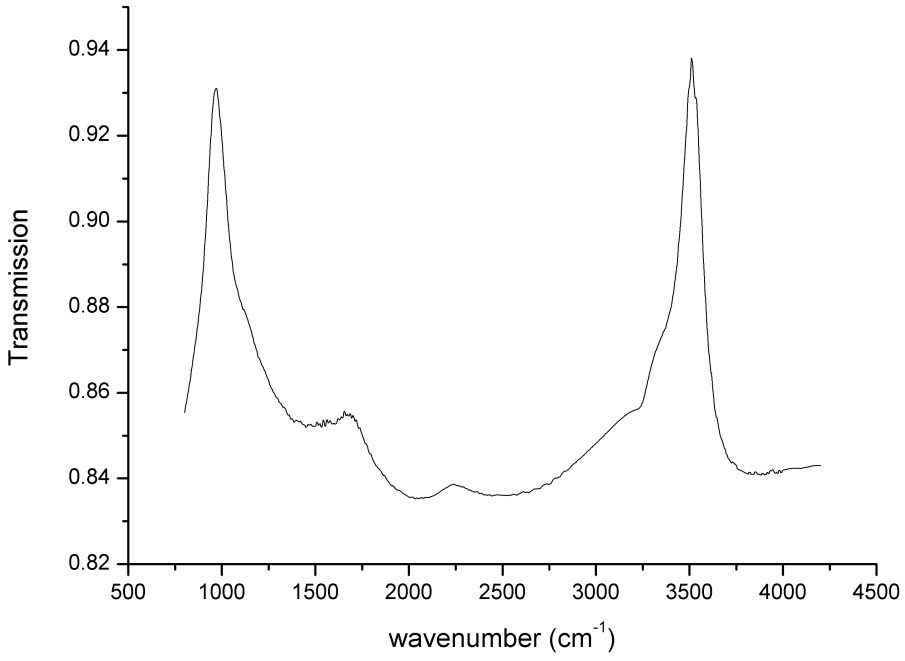

(b) Transmission K_{ice} for an ice particle

Figure 5.26: Extinction β_{ice} ($\mathrm{km^{-1}cm^3}\mu\mathrm{m^{-3}}$) and transmission K_{ice} for an aerosol volume slant column $SC = 500\,\mu\mathrm{m^3\,cm^{-3}\,km}$ of ice particles. The optical constants are taken from *Clapp et al.* (1995), measured at 215 K.

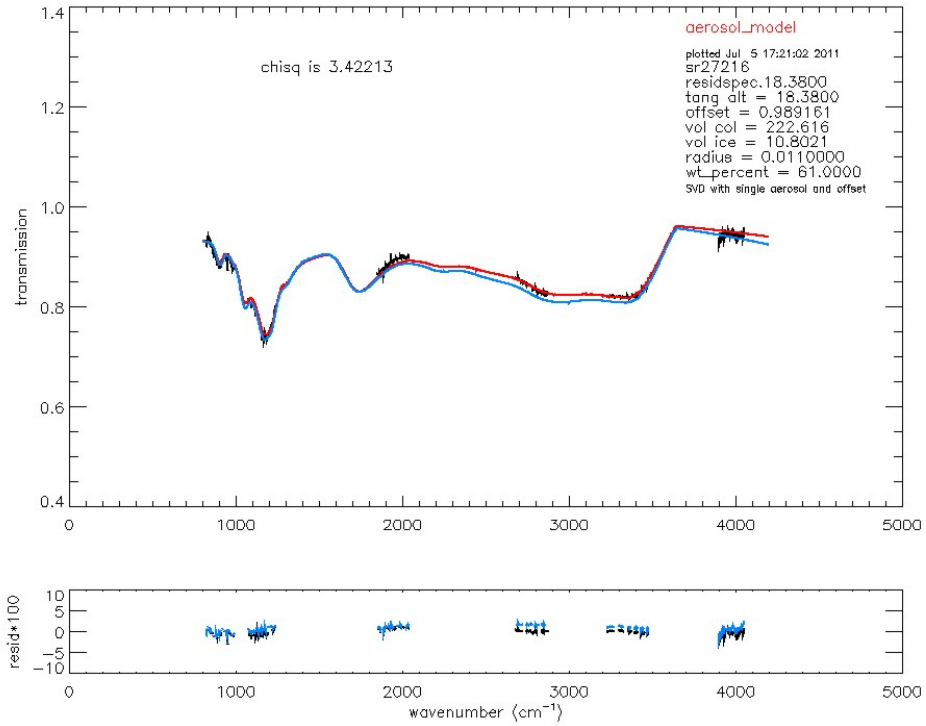

(a) sr27216 (01.09.2008, 35.27°N, 84.07°W) at 18.4 km

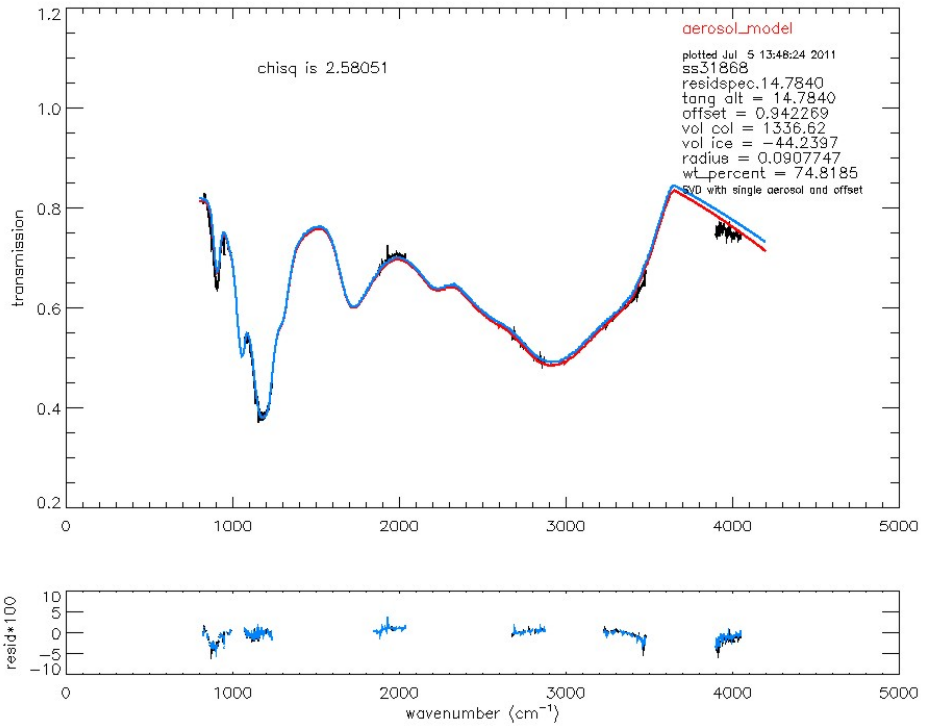

(b) ss31868 (14.07.2009, 68.31°N, 18.86°W) at 14.8 km

Figure 5.27: K_{meas} (black), K_{model} (red) and K_{combo} – including both the extinction of ice particles and sulphate aerosol – (blue) against the wavenumber (cm^{-1}) between 800 and 4200 cm^{-1}, are shown for two different occultations in the tangent height with the maximum aerosol signal. The residuals are displayed in the lower panel showing the precision of the fitting.

with an effective radius R_{eff} below 0.2 μm. In the temperature profile (Figure 5.28 (a)) a layer with enhanced temperature has been observed at an altitude of approximately 14 km with an approximate enhancement of $\Delta T \approx 1.5\,\mathrm{K}$. For the occultation ss31868, influenced by the Sarychev eruptions, with an enhanced aerosol loading of $V \approx 3.0\,\mu\mathrm{m}^3\mathrm{cm}^{-3}$ at 15 km and an effective radius R_{eff} between 0.1 μm and 0.3 μm, enhanced temperature can be seen at approximately 12 km with $\Delta T \approx 4.8\,\mathrm{K}$. The enhancement of the temperature occurs at a lower altitude than the actual altitude of the maximum aerosol loading. A possible reason for this could be that the warming is mainly caused by large aerosol particles which might have a maximum at a lower altitude than the median sized aerosol particles.

However, this enhancement is relatively small compared to the large uncertainty of the temperature retrieval from ACE-FTS of 2 K (*Dufour et al.*, 2009). This error is larger than most observed temperature enhancements, e.g. for sr27268 $\Delta T \approx 1.5\,\mathrm{K}$, and for many other occultations, a temperature enhancement does not appear with an aerosol loading from a volcanic plume. It is most likely that the effect cannot be observed because of the age (here approximately one month after the eruption), when larger particles like dust and ash particles have already dispersed to the surface. As an exception, for the occultation ss31868 a temperature increase of $\Delta T \approx 4.8\,\mathrm{K}$ has been observed approximately 3 km below the maximum aerosol loading, indicating a layer of larger particles at that altitude. However, due to the large uncertainty, a precise analysis of the absorption of IR, leading to a warming in the layer of high aerosol loading cannot be done using ACE-FTS temperature retrievals. The temperature perturbation can also cause difficulties in detecting the temperature anomaly due to a volcanic plume. Hereby the temperature is likely to be much larger in the absence of the cloud than the brightness temperature of the underlying atmosphere or surface. In this case, a much larger temperature would be detected than if clouds are present.

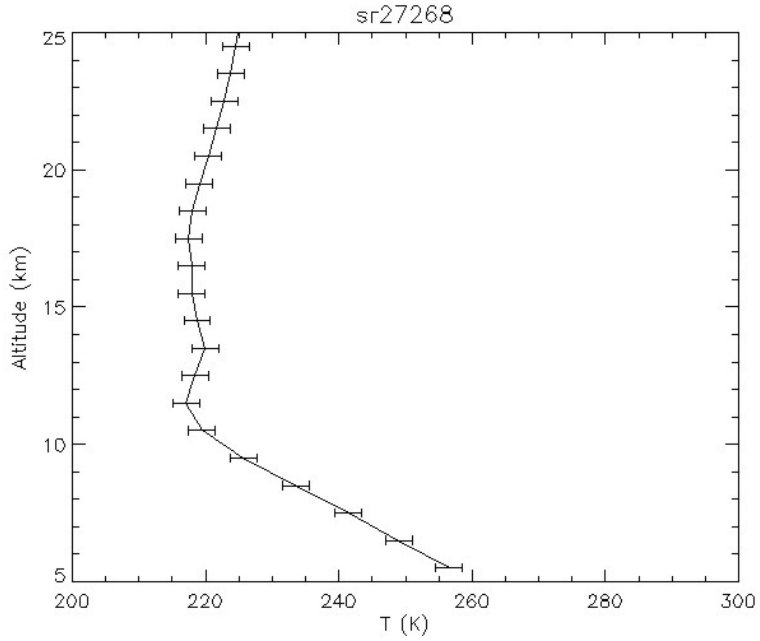

(a) sr27268 (04.09.2008, 47.58°N, 83.30°E)

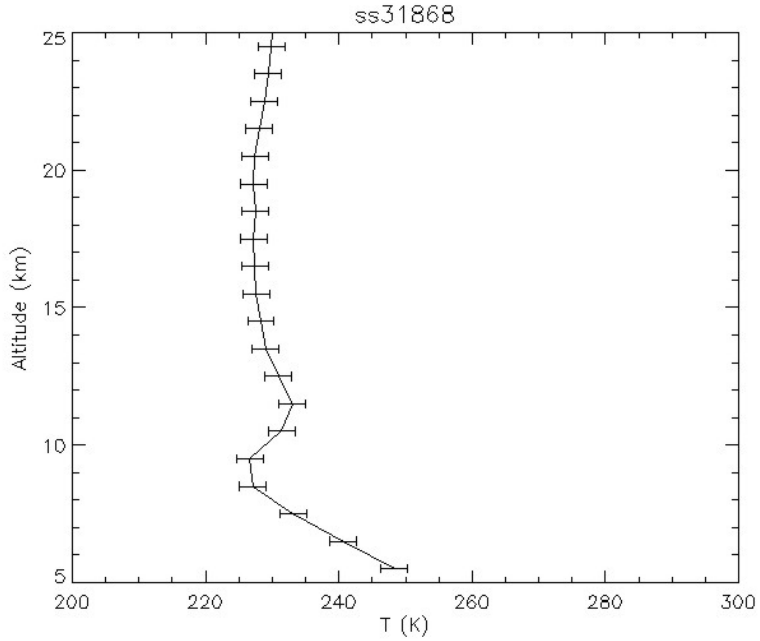

(b) ss31868 (14.07.2009, 68.31°N, 18.86°W)

Figure 5.28: Two temperature profiles (K) are displayed for two different occultations with a high aerosol loading: (a) influenced by the Kasatochi eruptions (August 2008) with a maximum aerosol loading of $V \approx 1.8\,\mu\mathrm{m}^3\mathrm{cm}^{-3}$ at 17.5 km and (b) influenced by the Sarychev eruptions (June 2009) with a maximum aerosol loading of $V \approx 3.0\,\mu\mathrm{m}^3\mathrm{cm}^{-3}$ at 15 km.

5.7. Analysis of other volcanic gases using ACE-FTS

Table 1 (in Chapter 2.2.1) lists the most typical gas compositions of the main components in volcanic plumes. Apart from the previously discussed, sulphur dioxide, the following are classed as the most common gases: water vapour, carbon dioxide, hydrogen sulphide, hydrogen chlorine as well as hydrogen fluorine and will be analysed in this chapter using ACE-FTS retrievals. Unfortunately, the retrieval of hydrogen sulphide (H_2S), oxidizing to SO_2 within a few days (*Rose et al.*, 2000), corresponds only to noise, probably because of the age of the observed volcanic plumes of almost one month, and due to the difficulties in the retrieval of H_2S.

5.7.1. Carbon dioxide (CO_2)

Figure 5.29 shows two examples of the CO_2 profiles, influenced (a) by the Kasatochi eruptions and (b) the Sarychev eruptions (black solid lines). The median CO_2 concentration profile of the accordant month (between 2004 and 2010) is displayed in red, showing an almost straight line at a concentration between 373 ppm and 381 ppm. In most analysed cases (from occultations influenced by the Kasatochi or Sarychev eruption) no or very little enhanced CO_2 could be found. For example, the occultation sr27268 in Figure 5.29 (a), influenced by the Kasatochi eruptions, shows a small enhancement with a maximum of 386 ppm at 15.5 km.

However, one observed occultation (ss31976, 21.07.2009, 63.51°N, 176.37°W), shown in Figure 5.29 (b) has been found with a high proportion of carbon dioxide. The enhanced CO_2 layer spans from 21 km to 15.5 km with a maximum concentration of 406 ppm at an altitude of 18.5 km, which corresponds to the profile of SO_2 and atmospheric extinction (see Figure 5.12).

The percentaged proportion of CO_2 in volcanic plumes is between 1 % and 40 % of their volume (*Textor et al.*, 2004), therefore, depending on the specific volcanic eruption the amount of injected CO_2 into the troposphere and lower stratosphere, varies significantly. Furthermore, the amount of CO_2 injected into the atmosphere, although it would be 40 % of the volcanic plume, is quite small compared to the CO_2 background of approximately 380 ppm. This leads to the result that the detection of volcanic plumes using the CO_2 concentration profile from ACE-FTS is almost impossible and the analysis of the CO_2 concentration in the volcanic plume is quite difficult and not precise due the the high background concentration. Only for one example (ss31976) a strong enhanced and clearly defined layer of carbon dioxide has been detected, which is very unusual.

5.7.2. Hydrogen halides (HF and HCl)

Particular hydrogen halides, like hydrogen chlorine (HCl) and hydrogen fluorine (HF) are stable in the stratosphere and are mostly removed by dilution into the troposphere, where they are disposed by precipitation.

The injection of hydrogen chlorine varies between $1-10$ % of the volume of the volcanic plume (*Textor et al.*, 2004), while the background concentration in the higher troposphere and lower stratosphere varies between 0.1 ppb and 1 ppb, increasing monotonically with altitude. Figure 5.30 shows an example of the HCl profile (black solid line) for two occultations (sr27268 and ss31868), which are influenced by volcanic plumes from the Kasatochi and Sarychev eruptions, respectively. The red line represents the median

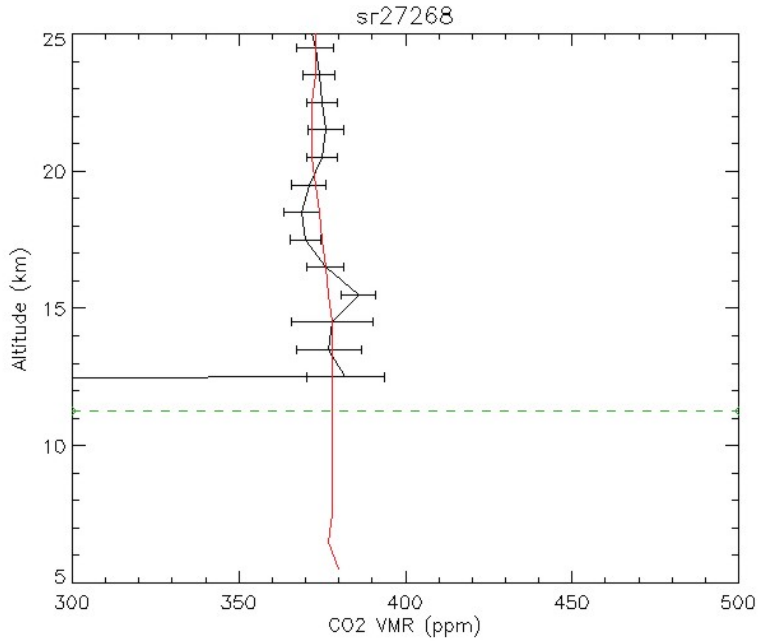

(a) sr27268 (04.09.2008, 47.58°N, 83.30°E)

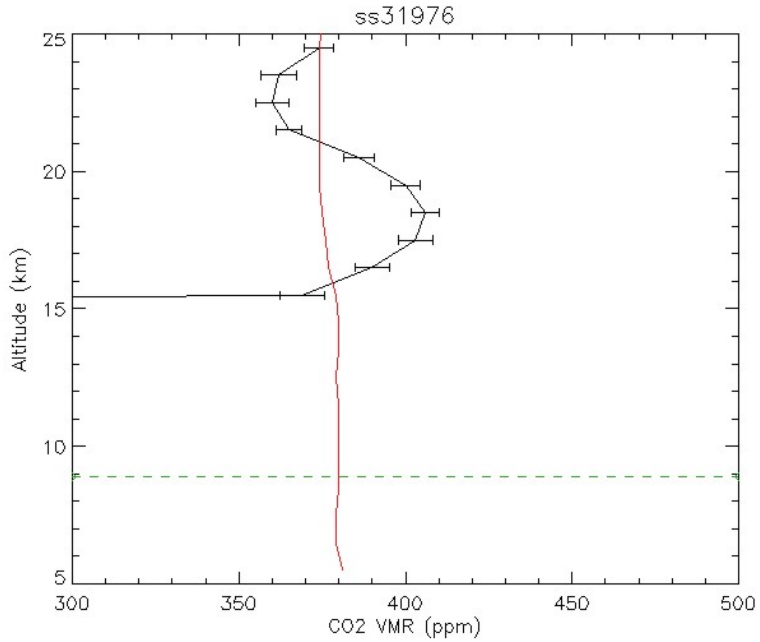

(b) ss31976 (21.07.2009, 63.51°N, 176.37°W)

Figure 5.29: Two carbon dioxide profiles (ppb) (black solid lines) are displayed for two different occultations with a high aerosol loading: (a) influenced by the Kasatochi eruptions (August 2008) with a maximum aerosol loading at 17.5 km and (b) influenced by the Sarychev eruptions (June 2009) with a maximum aerosol loading at 16 km. The red line represents the median of the accordant month (from 2004 to 2010).

HCl concentration for the accordant month (between 2004 and 2010) for a comparison with the individual concentration profile. In neither of these examples nor in any other occultations with a clear influence of a volcanic plume from either Kasatochi (2008) or Sarychev (2009), have a strongly enhanced layer of HCl been found. The low proportion in the volcanic plumes of both eruptions is possibly the cause for the absence of enhanced HCl in these profiles. Therefore, the concentration profile or enhancements of HCl, using ACE data, do not appear to be suitable for the detection of volcanic plumes.

The proportion of HF in volcanic plumes is very low, but mostly above 10^{-3} % (*Textor et al.*, 2004). The profile of HF increases with altitude in the stratosphere and varies between 0.1 ppb and 1 ppb. In Figure 5.31 the profile of two occultations (black sold lines), influenced by the Kasatochi and Sarychev eruptions, respectively. For comparison between these occultations and background concentration, the median of the accordant month (between 2004 and 2010) is displayed in red. As seen in Figure 5.31, an enhanced layer of HF cannot be seen, neither for the Kasatochi plume (sr27268, Figure 5.31 (a)), nor for the Sarychev plume (ss31868, Figure 5.31 (b)), due to the very low concentration of HF in a volcanic plume.

5.7.3. Water vapour

Water vapour is the major gas in a typical volcanic plume, as a percentaged proportion of the volume varies between 50 % and 90 % (*Textor et al.*, 2004). Therefore, for a plume with an SO_2 concentration of $[SO_2] = 1$ ppb and a typical proportion of 15 % SO_2 (*Textor et al.*, 2004) and 70 % H_2O, the concentration of H2O would lead to $[H_2O] \approx 5$ ppb. Compared to the background concentration in the stratosphere (above the tropopause) of approximately 5 ppm, the perturbation is approximately 1000 times smaller than the typical background concentration, which makes a precise analysis of the impact of water caused by a volcanic eruption, using ACE-FTS retrievals with a median error of 0.1 ppm, impossible.

In Figure 5.32, two examples are presented for the Kasatochi (Figure 5.32 (a)) and the Sarychev (Figure 5.32 (b)) plume. The median of the accordant month (between 2004 and 2010) is plotted in red for the purpose of comparison with the individual profiles. At an altitude of 15.5 km (Figure 5.32 (a)) and 13.5 km (Figure 5.32 (b)), respectively, which is approximately 2 km below the maximum aerosol loading, a small enhancement in the water vapour concentration can be seen (red encircled), which is, however, too small for a precise analysis.

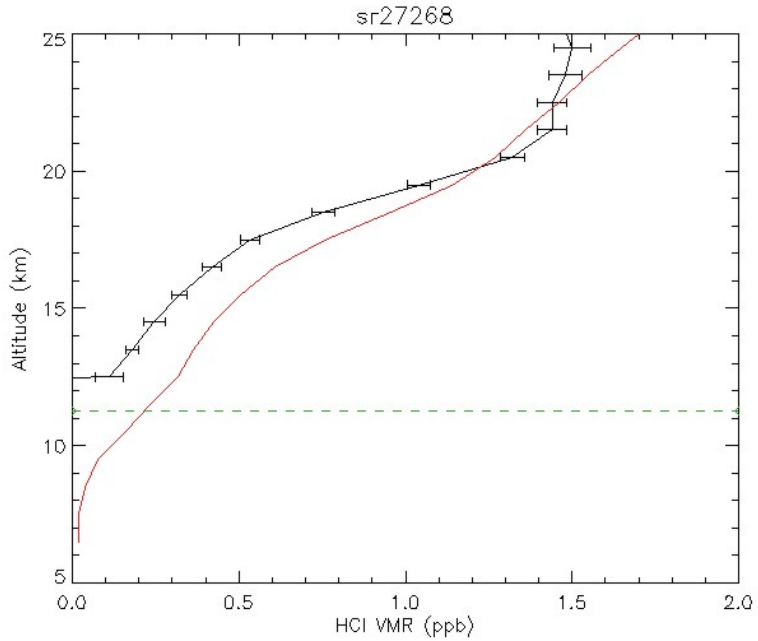

(a) sr27268 (04.09.2008, 47.58°N, 83.30°E)

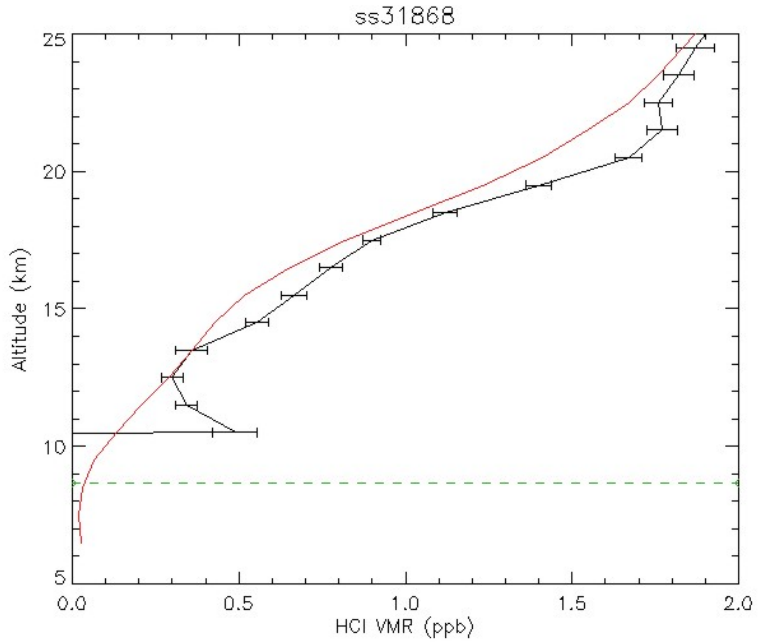

(b) ss31868 (14.07.2009, 68.31°N, 18.86°W)

Figure 5.30: Two hydrogen chloride profiles (ppb) (black solid lines) are displayed for two different occultations with a high aerosol loading: (a) influenced by the Kasatochi eruptions (August 2008) with a maximum aerosol loading at 17.5 km and (b) influenced by the Sarychev eruptions (June 2009) with a maximum aerosol loading at 15 km. The red line represents the median of the accordant month (from 2004 to 2010).

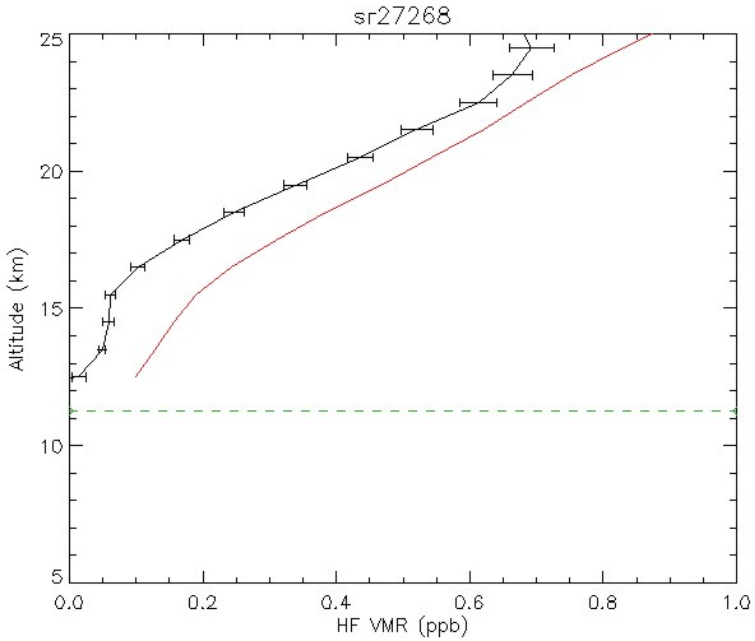

(a) sr27268 (04.09.2008, 47.58°N, 83.30°E)

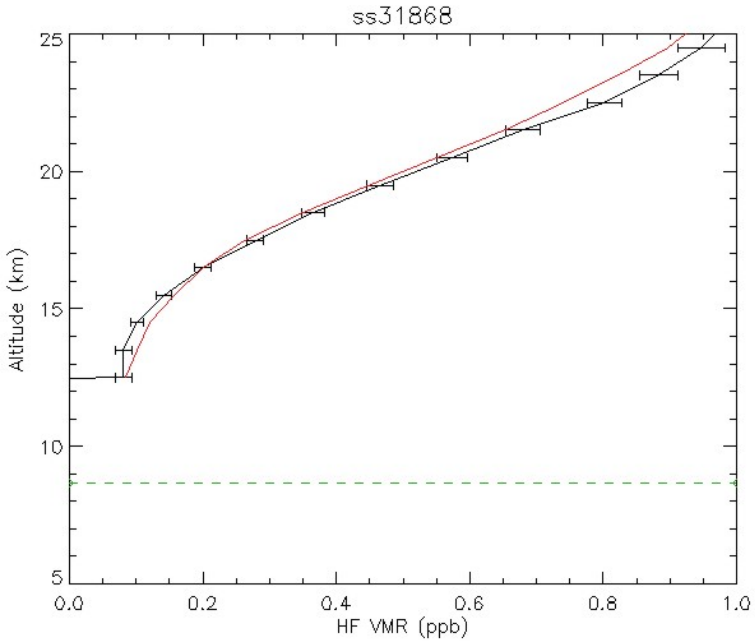

(b) ss31868 (14.07.2009, 68.31°N, 18.86°W)

Figure 5.31: Two hydrogen fluoride profiles (ppb) (black solid lines) are displayed for two different occultations with a high aerosol loading: (a) influenced by the Kasatochi eruptions (August 2008) with a maximum aerosol loading at 17.5 km and (b) influenced by the Sarychev eruptions (June 2009) with a maximum aerosol loading at 15 km. The red line represents the median of the accordant month (from 2004 to 2010).

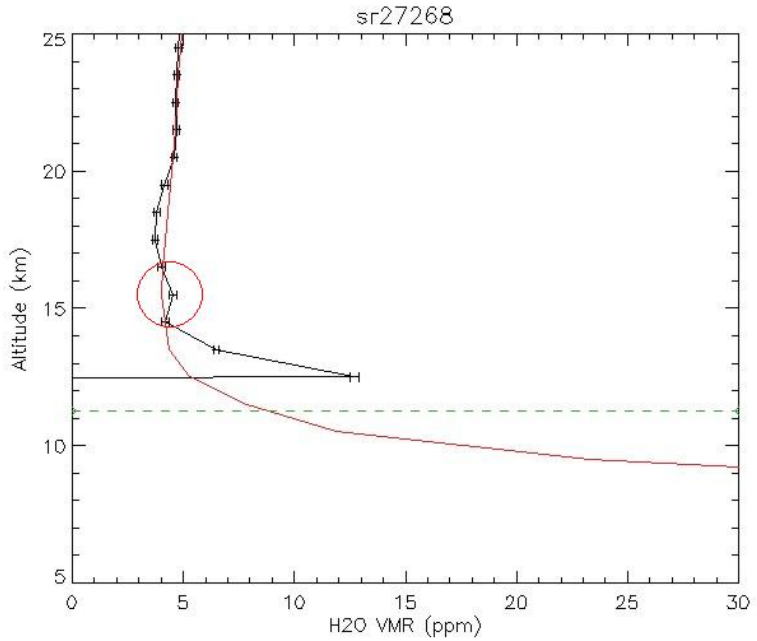

(a) sr27268 (04.09.2008, 47.58°N, 83.30°E)

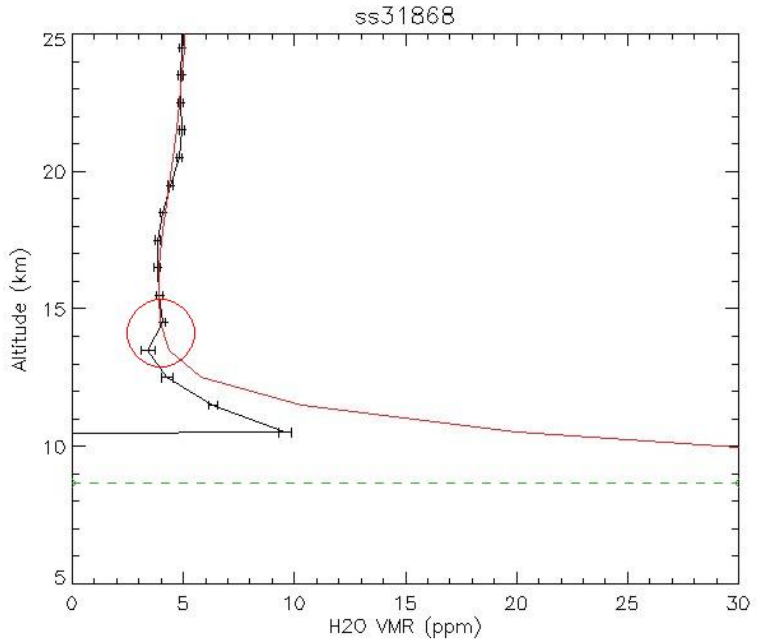

(b) ss31868 (14.07.2009, 68.31°N, 18.86°W)

Figure 5.32: Two water vapour profiles (ppm) (black solid lines) are displayed for two different occultations with a high aerosol loading: (a) influenced by the Kasatochi eruptions (August 2008) with a maximum aerosol loading at 17.5 km and (b) influenced by the Sarychev eruptions (June 2009) with a maximum aerosol loading at 15 km. The red line represents the median of the accordant month (from 2004 to 2010), while the green dashed line indicates the height of the tropopause.

5.8. Analysis of a "fresh" volcanic plume

The Icelandic volcano Grimsvötn, located at 65° 25' N and 17° 20' W, erupted between 21 – 28 May 2011. During this time period, the ACE satellite orbited the Earth between a latitude of 65° and 69° in the Northern Hemisphere, detecting in exactly the area, where the volcano erupted. In this chapter this fresh volcanic plume is analysed using ACE-FTS retrievals, comparing the results to the analysis of the Kasatochi and Sarychev eruptions, which were detected by ACE one month after the eruptions.

Between 21 – 24 May 2011, two occultations have been detected by ACE with an enhanced SO_2 concentration (VMR > 0.1 ppb), which are namely sr41865 (23.05.2011, 67.39°N, 24.58°W) and sr41880 (24.05.2011, 68.05°N, 36.63°W). Figure 5.33 displays the SO_2 concentration profile for (a) sr41865 and (b) sr41880, showing a plume (a) below 13.5 km and (b) at 14.5 km, respectively. The maximum enhancement of (a) $[SO_2] = 1.39 \pm 0.02$ ppb for sr41865 at an altitude of 13.5 km and (b) $[SO_2] = 0.54 \pm 0.01$ ppb for sr41880 at an altitude of 14.5 km, is clear indicator of the influence from the Grimsvötn eruptions in the accordant occultation. As before the eruptions no SO_2 enhancement was detected by ACE.

The same occultations have been analysed of the existence of sulphate aerosol using the previously described method employing the continuum spectrum from ACE-FTS data. The results of this analysis at the approximate altitude of the maximum SO_2 concentration are presented in Figure 5.34, where the observed spectrum ΔK_{meas} is plotted in black and the modelled spectrum ΔK_{model} in red. No strong absorption from sulphate aerosol (H_2SO_4) can be seen in either of these occultations. For sr41865 a volume slant column $SC \approx 75\,\mu m^3\,cm^{-3}\,km$ and for sr41880 $SC \approx 88\,\mu m^3\,cm^{-3}\,km$, was retrieved, compared to the background of $SC \approx 80\,\mu m^3\,cm^{-3}\,km$ at 13.5 km, no sulphate aerosol caused by the volcanic eruption is present. Furthermore, it can be seen that the retrieved spectrum ΔK_{model} does not correspond to the observed spectrum ΔK_{meas}, especially for the wavenumber range between $2000\,cm^{-1}$ and $3500\,cm^{-1}$; the absorption is overestimated in the modelled spectrum. Also the χ^2-value indicates an inaccurate retrieval of the modelled spectra, as the value correlates to $\chi^2 = 15.8$ for sr41865 and $\chi^2 = 13.1$ for sr41880. In the observed spectrum ΔK_{meas}, absorption features can be seen, which are probably related to dust and ash particles from the volcanic eruptions. The process for SO_2 oxidizing to H_2SO_4 takes several weeks, this can be seen in our results, as fresh volcanic plumes do not contain any sulphate aerosol absorption bands, but clear sulphate acid signatures have been found in aged volcanic plumes from Kasatochi and Sarychev.

The fresh volcanic plume, which is not older than three days, has also been analysed for H_2S, which oxidises within a few days to SO_2. Although the volcanic plume is fresh, no signal of H_2S has been found above the noise for the retrievals of the two occultations, influenced by a fresh volcanic plume. The possible reason for that is, that it is difficult to retrieve H_2S because most of its absorption bands overlap with strong water absorption bands, which makes any retrieval problematic (*Clarisse et al.*, 2011).

The temperature profile of these two occultations influenced by fresh volcanic gases and probably ash particles have been analysed and the profile of the temperature is presented in Figure 5.35. In Figure 5.35 (a), a temperature increase can be seen at an altitude of 11.5 km with $\Delta T \approx 3.8\,K$, which could be due to a layer of volcanic ash. A smaller temperature increase of approximately $\Delta T \approx 2\,K$ can be seen for sr41880 at

11.5 km, shown in Figure 5.35 (b). However, as previously mentioned, the uncertainty of the temperature is approximately 2 K (*Dufour et al.*, 2009) and, therefore, small temperature abnormalities should not be overrated in the profile. Therefore, definite evidence of a temperature increase in the layer of volcanic aerosols cannot be shown, using ACE-FTS data.

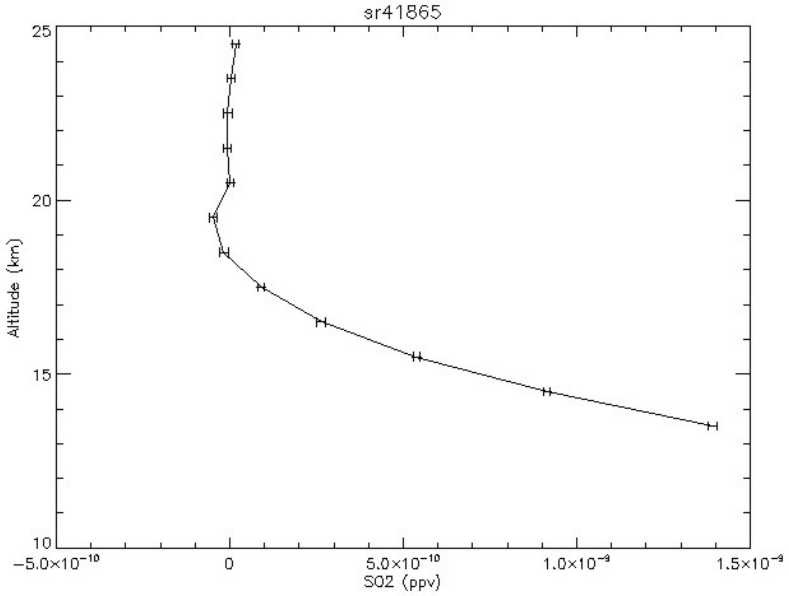

(a) sr41865 (23.05.2011, 67.39°N, 24.58°W)

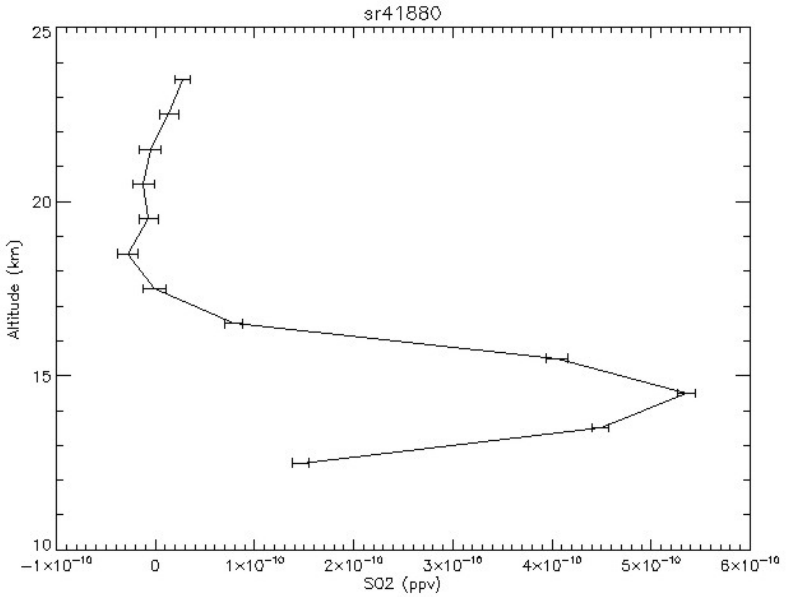

(b) sr41880 (24.05.2011, 68.05°N, 36.63°W)

Figure 5.33: SO_2 profile of two occultations with enhanced SO_2 (VMR > 0.1 ppb), after the eruptions of Grimsvötn in Iceland (May 2011).

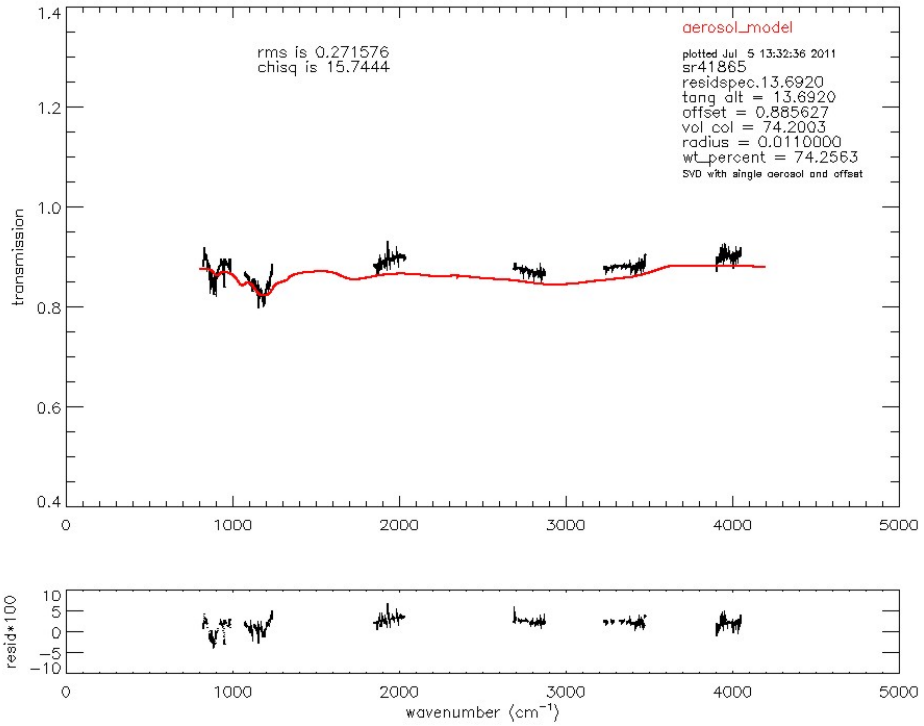

(a) sr41865 at 13.69 km (23.05.2011, 67.39°N, 24.58°W)

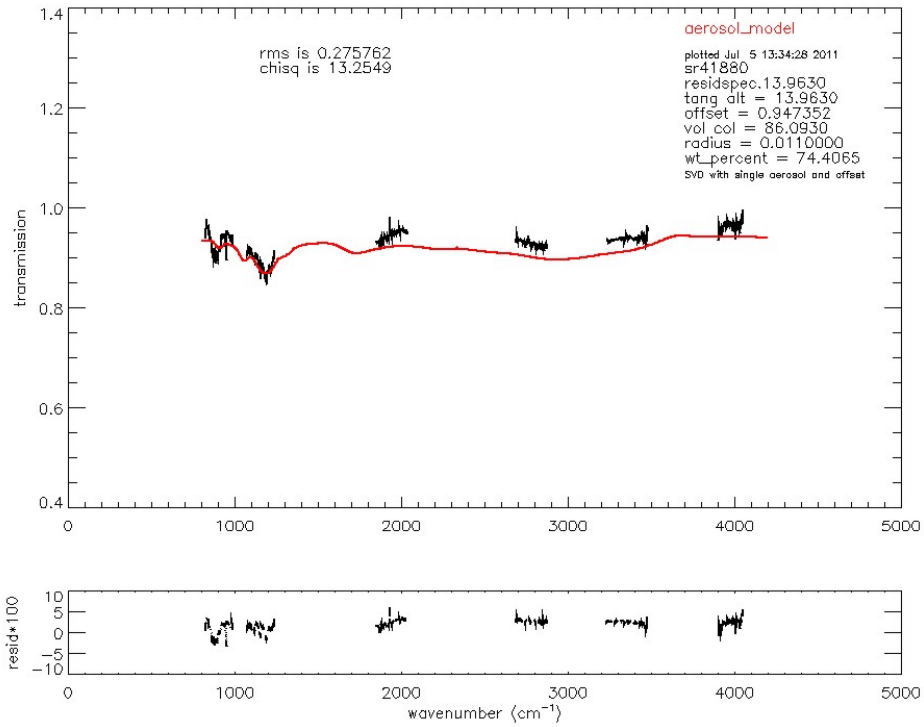

(b) sr41880 at 13.96 km (24.05.2011, 68.05°N, 36.63°W)

Figure 5.34: K_{meas} (black) and K_{model} against the wavenumber (cm^{-1}) between 800 and 4200 cm^{-1} is shown for two occultations, influenced by the eruptions of Grimsvötn (Iceland, 2011) for the tangent height with the maximum aerosol signal (at about 14 km). No strong absorption lines due to sulphate aerosols can be seen. The residuals are displayed in the lower panel showing that the retrieval is not precise, resulting in a $\chi^2 \approx 14$.

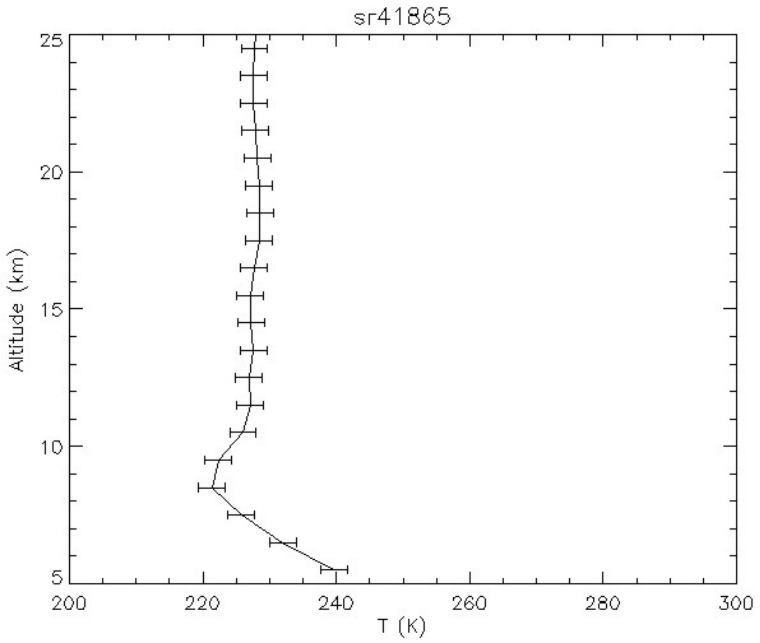

(a) sr41865 (23.05.2011, 67.39°N, 24.58°W)

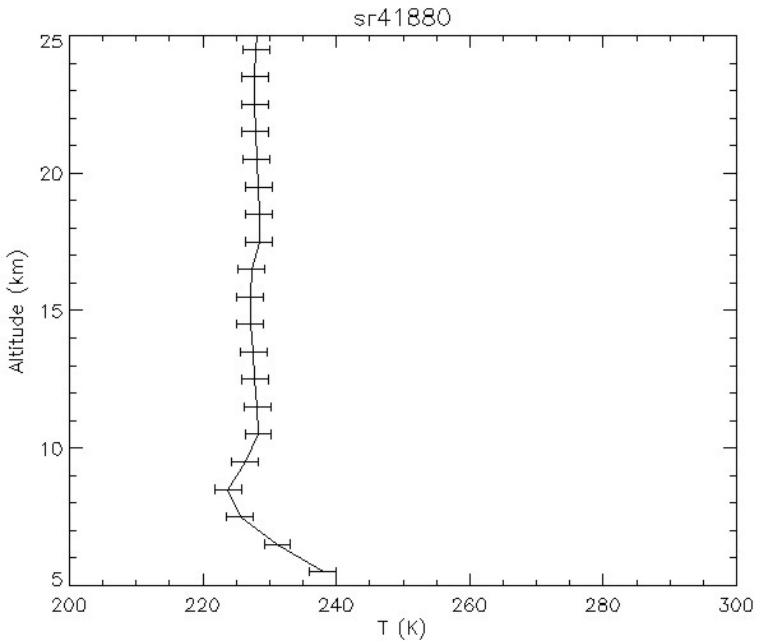

(b) sr41880 (24.05.2011, 68.05°N, 36.63°W)

Figure 5.35: Temperature profile of two occultations with enhanced SO_2 (VMR > 0.1 ppb), after the eruptions of Grimsvötn in Iceland (May 2011).

6. Summary and outlook

6.1. Analysis of volcanic plumes

For the first time the SO_2 concentration profiles have been analysed and the parameters of the aerosol size distributions have been successfully derived, using the data from the ACE instrument. Tracing volcanic plumes from the Kasatochi (August 2008), Sarychev (June 2009) and Grimsvötn (May 2011) eruptions, using enhanced SO_2 profiles from ACE-FTS retrievals, was successfully determined using infrared solar occultation spectra recorded with ACE-FTS. SO_2 retrievals are unfortunately limited to a minimum altitude of 12.5 km, and therefore, only strato-volcanic eruptions with a large injection of sulphur can be detected. For example, the eruptions of Eyjafjallajökull (Iceland, 2010) have not been detected because of the low injection of SO_2. However, this method seems to be the best way of detecting volcanic plumes using ACE data, as neither of the other major gases in volcanic plumes, such as H_2O, CO_2, H_2S, HCl and HF, seem to be suitable for plume tracing (see Chapter 5.7), due to a relatively small injection compared to the high background concentration (H_2O and CO_2), a generally marginal or negligible injection (HCl and HF) or a relatively short lifetime (H_2S).

The work discussed, *inter alia* the observation and evolution of the Kasatochi and Sarychev volcanic plume and the "fresh" plume from the Grimsvötn eruptions. Using enhanced SO_2 concentrations, volcanic plumes can successfully and reliably be found, as well as sulphate aerosol parameters within favourable occultations. A volcanic plume from the Kasatochi eruptions was found in September 2008 between 6.5 km and 17.5 km altitude and between 8.5 km and 17.5 km altitude for the Sarychev eruptions in July 2009. The plume height was found to decline by approximately 1 km per month based on near infrared imager profiles. A temperature increase from the FTS retrieval (*Boone et al.*, 2005) in the layer of the plume resulting from absorption of IR radiation of the aerosols cannot be seen clearly because the effect is relatively small compared to the statistical error of 2 K (*Sica et al.*, 2008). One month after the eruptions, Kasatochi's, as well as Sarychev's volcanic plumes were spread over mid and high-latitudes of the Northern Hemisphere (between approximately 55°N and 70°N), but did not reach the region around the tropics or the Southern Hemisphere because of the long transport time. A similar spreading for the Sarychev plume has been detected by IASI (*Haywood et al.*, 2010), where the highest SO_2 concentrations are between 55°N and 80°N and small perturbation reaches down to 35°N; IASI detected the Kasatochi plume between 35°N−90°N at the end of August (`http://cpm-ws4.ulb.ac.be/Alerts/index.php`). This is in very good agreement with our results using ACE infrared data, considering that ACE does not have the same global coverage as IASI. The different analysis methods presented here: atmospheric extinction with the ACE-Imager, SO_2 concentrations retrieved from ACE-FTS and aerosol loading determined by a least-squares fitting of a modelled H_2SO_4 spectrum, show consistency, resulting in the same height of the plume.

The Cloud-Aerosol Lidar and Infrared Pathfinder Satellite Observation (CALIPSO) from NASA and CNES (Centre National d'Etudes Spatiales), provides *inter alia* information of the atmospheric extinction. Two example profiles of the atmospheric extinction from 7 and 10 July 2009 detected by CALIPSO (from `http://www-calipso.larc.nasa.gov`) are presented in Figure 6.1. An enhancement of the atmospheric extinction (approximately 3.0×10^{-3} 1/km at 525 nm) has been detected at an approximate altitude of 15 km and between 76°N and 40°N (see Figure 6.1). These results agree well with the results from ACE observations of the Sarychev eruptions presented in this the-

sis. Note, that the absolute value of the atmospheric extinction cannot be compared as it was detected at different wavelength. The temporal evolution the zonal mean scattering ratio from CALIPSO observations (*Solomon et al.*, 2011) is in good agreement with our evolution of the optical depth, where the atmosphere had returned to pre-eruptions conditions by April 2009 (Kasatochi) and by February 2010 (Sarychev).

The plume of the Grimsvötn eruptions was detected with a maximum age of 3 days, which could be used for a comparison between "fresh" and aged volcanic plumes. Evidence for the differences between these plumes has been obtained, including the evolution of H_2SO_4. Only for aged volcanic plumes, a signal of sulphate acid has been observed in the continuum spectrum, showing that the oxidation of SO_2 in the stratosphere takes up to several weeks.

Significantly different conditions in atmospheric extinction and optical depth have been obtained after both the Kasatochi and the Sarychev eruptions, indicating distinct post-volcanic conditions. Table 4 lists the SO_2 injection and the change in the optical depth due to the Pinatubo, El Chichón, Sarychev and Kasatochi eruptions. The eruptions of Kasatochi and Sarychev are remarkably smaller than these from Pinatubo and El Chichón, leading to a change in the optical depth in the Northern Hemisphere of 0.013 (NIR) or 0.014 (VIS) caused by Kasatochi and 0.011 (VIS) or between 0.009 and 0.013 (VIS) due to Sarychev. Table 4 also lists the results of this study compared to other results, according to the change in the optical depth, which demonstrates very good agreement with the results from other studies. Approximately 8 months after the Kasatochi eruptions, in April 2009, no influence of the Kasatochi volcanic plume can be detected with ACE and pre-Kasatochi conditions are reached again. No evidence of the presence of the Sarychev volcanic plume was observed after February 2010 and therefore pre-Sarychev conditions were reached once again from this date.

Table 4: Volcanic eruptions (comparison) of the SO_2 injection and change in the Aerosol optical depth in the Northern Hemisphere at approximately 550 nm and at 1030 nm (*).

Volcano	Eruption date	SO_2 injection (Tg)	Change in AOD
Pinatubo	June 1991	$1 - 40$[1]	0.15[4] $- 0.20$[5]
El Chichón	March - April 1982	$7 - 12$[1]	0.10[4] $- 0.14$[5]
Sarychev	June 2009	1.2[2]	$0.009 - 0.010$[2]
Kasatochi	August 2008	$1.4 - 1.6$[3]	0.013^{*}[6]
Sarychev	June 2009	–	0.013[7]
Kasatochi	August 2008	–	0.014[7]
Sarychev	June 2009	–	0.011^{*}[7]
Kasatochi	August 2008	–	0.013^{*}[7]

[1] *Bluth et al.* (1992)
[2] *Haywood et al.* (2010)
[3] *Carn et al.* (2009)
[4] *Sato et al.* (1993)
[5] *Ammann et al.* (1992)
[6] *Sioris et al.* (2010)
[7] This study.

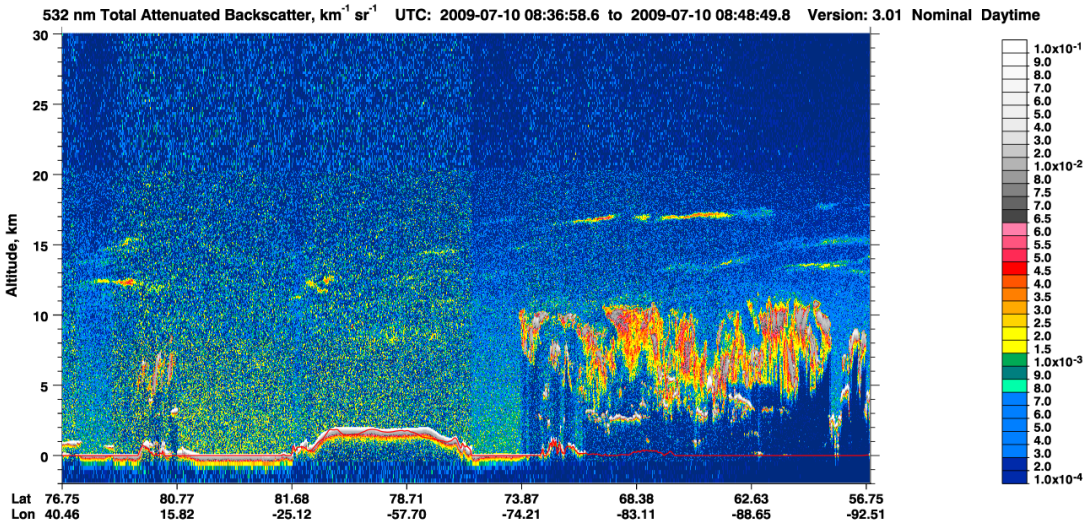

(a) CALIPSO observations from 10 July 2009

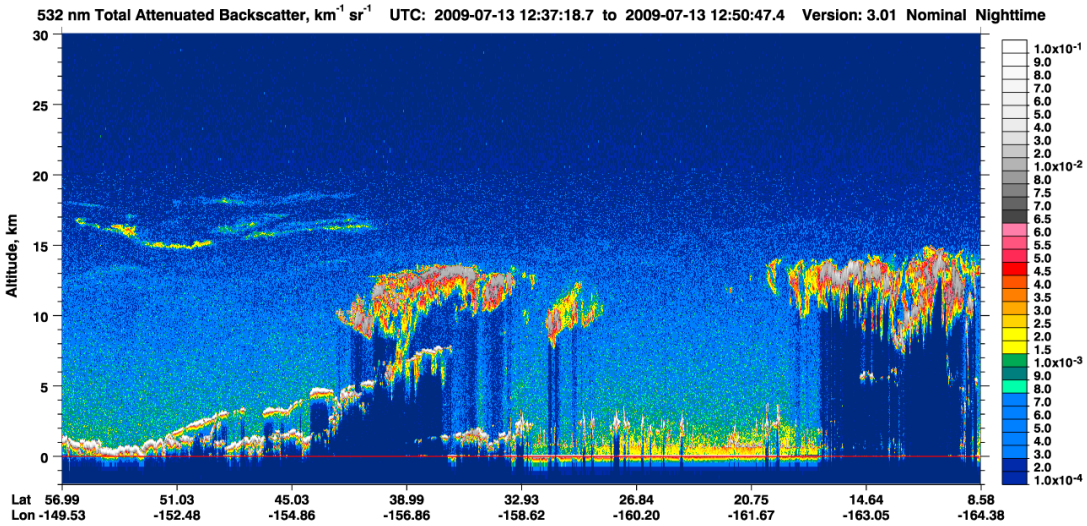

(b) CALIPSO observations from 13 July 2009

Figure 6.1: CALIPSO observations of the atmospheric extinction at 525 nm. An enhancement is detected between 70°N and 40°N at approximately 15 km which is likely due to the Sarychev volcanic aerosol.

6.2. Retrieval of the aerosol properties

It has been shown that aerosol properties can be studied with the wide, high resolutive spectra and low SNR from ACE. The aerosol absorption signal was separated from the continuum spectra between 820 and 4100 cm^{-1} using the method of *Eldering et al.* (2001). However, the radius retrieval method works only when the slant column is greater than a threshold value. The higher the aerosol concentration, the more values like the effective radius R_{eff} and the mean radius r_g can be retrieved. It has been found that the amount of aerosol loading necessary for a successful aerosol radius retrieval is also linked to the height of the aerosol loading, while a stronger aerosol signal is required for a retrieval at a lower altitudes. As shown in this study, the minimum volume slant column required for a retrieval of these radii is approximately $SC \geq 300\,\mu m^3\,cm^{-3}\,km$ at 18 km and $SC \geq 500\,\mu m^3\,cm^{-3}\,km$ at 15 km, and has been found for several analysed occultations.

The aerosol volume slant column, a month after the Kasatochi eruptions was between $500\,\mu m^3\,cm^{-3}\,km$ and $300\,\mu m^3\,cm^{-3}\,km$, leading to an aerosol loading of $1.8 - 1.0\,\mu m^3\,cm^{-3}$. A change of the composition of the aerosol droplets has been observed, changing from 65 % to 73 % sulphate acid-water droplets within one week. The mean radius r_g has been retrieved and shown to be on average $0.04\,\mu m$ (for a geometric standard deviation of $\sigma = 1.8$), while the effective radius R_{eff} was found for $R_{eff} \leq 0.2\,\mu m$. In the two occultations from the Sarychev eruptions, the maximum volume slant column SC was found to be $850\,\mu m^3\,cm^{-3}\,km$ (ss31868) and $500\,\mu m^3\,cm^{-3}\,km$ (ss31976), which results in an approximate aerosol loading of 3 $\mu m^3\,cm^{-3}$ (ss31868) and 1.5 $\mu m^3\,cm^{-3}$ (ss31796). The size distribution cannot be constrained uniquely but with a geometric standard deviation σ between 1.6 and 2.0 the radius r_g results in $0.052\,\mu m \leq r_g \leq 0.13\,\mu m$ (ss31868) and $0.056\,\mu m \leq r_g \leq 0.14\,\mu m$ (ss31976). The lowest χ^2-values (between 2.0 and 2.5) corresponds to an R_{eff} of $0.1 - 0.3\,\mu m$. The composition of the aerosol droplets was in both cases 75 % H_2SO_4 and 25 % H_2O. The retrieved offsets $\alpha = 1$ in most cases because the ACE-detector is linear. Only at or below the peak height of the plume is the offset α less than 1 (around 0.95), probably due to extinction of a high concentration of particles in the plume, e.g. ash particles.

In addition to the H_2SO_4 aerosol, the extinction of an ice cloud was fitted on the observed continuum spectra with refractive indices taken from *Clapp et al.* (1995) and a unimodal log-normal distribution ($r_g = 2.5\,\mu m$ and $\sigma = 1.8$) (*Yang et al.*, 1997). However, in all observed cases no signature of absorption from ice particles was found. The formation of cirrus clouds, in association with a volcanic plume from the Kasatochi and Sarychev eruptions, as it rises in the troposphere, are not present in the observed ACE spectra.

6.3. Understanding gained from this study

Large volcanic eruptions have a significant impact on the atmosphere. They affect climate by increasing the cloud albedo and reflecting more solar radiation to space, which leads to a net cooling of the lower atmosphere. The change of the chemical composition in volcanic plumes over time is important to understand their impact on global climate change. Especially, with the idea of geo-engineering, where SO_2 would be deliberately injected into the stratosphere to reduce the effects of global warming, it is of prime importance to understand the effects on the global climate, cloud formation and evolution of stratospheric SO_2 injections.

This study illustrates the influence of volcanic eruptions on the atmosphere and the time period in which the Kasatochi and Sarychev eruptions perturbed the stratosphere and troposphere. It has been shown, that the influence of volcanic eruptions is enhanced in the stratosphere compared to perturbations in the troposphere. While enhancements of the atmospheric extinction in the troposphere were not detected approximately 2 months after the eruptions, it takes approximately 8 months, dependent on the SO_2 injection for the removal of the plume in the stratosphere. A possible cooling effect due to the volcanic eruptions, as the optical depth is altered, occurs in a time period of approximately 8 months after the volcanic eruptions, which is likely to change with the intensity of the eruption and the amount of SO_2 injected into the stratosphere.

The reaction of sulphur dioxide to sulphuric acid takes several weeks. In this thesis it has been shown that it takes approximately 2 months until the sulphur dioxide is not detectable any more as it mostly oxidized to sulphuric acid. This could be an important time period for the oxidation to sulphuric acid to include in climate models.

6.4. Further applications of the analysis procedure

Sulphate aerosols from Merapi (Indonesia, 2010) and later occultations from Grimsvötn (Iceland, 2011) could be analysed in the future using ACE data with the method demonstrated here. The eruptions of Grimsvötn are of special interest because the evolution of the plume could be traced from just after the eruptions until the pre-Grimsvötn state is reached again.

The χ^2-values in the retrieval of the aerosol size parameters have been less than one for some retrievals of sulphate aerosol properties from Kasatochi's eruptions. These values are unrealistic and indicate an overestimated error ΔK_{meas}. The determination of the error ΔK_{meas} should be changed in the future, so that there is a maximum value the error is fixed to. If the retrieval of the error exceeds a certain value, the error will then be set at the pre-determined maximum.

According to *Steele et al.* (2006), the spectral range of the applied continuum spectrum is very important, much more than the number of points within a wavenumber range, for determination of the aerosol parameter with a high statistical precision. With the combination of ACE-FTS and MAESTRO spectra, the spectral range could be expanded and, therefore, the results improved. The expansion of the continuum spectrum using data from MAESTRO has the advantage of having a wavenumber range in the visible spectrum, where the sensitivity of the radius and geometric standard deviation is enhanced. Retrievals of the mean radius r_g, the effective radius R_{eff} and the geometric standard deviation σ could be improved, by enhancing the sensitivity for these parameters. For a higher sensitivity, the limit of the minimum required aerosol loading is likely to decreases, meaning that the evolution of the aerosol size parameters could be traced and analysed for selected volcanic eruptions *inter alia* Kasatochi or Sarychev.

Furthermore, instead of applying a unimodal log-normal distribution, a bimodal log-normal distribution could be included in the algorithm retrieving the aerosol properties. This would be a more realistic model for aged volcanic plumes, with a first mode around $r_1 \approx 0.01\,\mu$m and a second mode at approximately $r_2 \approx 1.0\,\mu$m.

A. Bibliography

References

Ammann, C. A., G. A. Meehl, and W. Washingtn (1992), A monthly and latidudinally varying volcanic forcing dataset in simulations of 20th century climate, *Geophys. Res. Lett.*, *30*, doi:10.1029/2003GL016875.

Ansmann, A., I. Mattis, U. Wandinger, F. Wagner, J. Reichardt, and T. Deshler (1997), Evolution of the Pinatubo aerosol: Raman lidar observations of particle optical depth, effective radius, mass, and surface area over central Europe at 53.4°N, *J. Atmos. Sci.*, *54*, 2630–2641.

AURA (2009), Summary of volcanic activity, *Bulletin of the Global Volcanism Network*, cloud/Aerosol/SO2 Working Group, based upon information contained in the Smithsonian, `http://www.volcano.si.edu/reports/bulletin/index.cfm`.

Barry, R. G., and R. J. Chorley (2003), *Atmosphere, weather and climate*, 8th ed., Routledge, London.

Bernath, P., et al. (2005), Atmospheric Chemistry Experiment (ACE): Mission overview, *Geophys. Res. Lett.*, *32*, doi:10.1029/2005GL022386.

Bernath, P. F. (2006), Atmospheric chemistry experiment (ACE): Analytical chemistry from orbit, *Trends in Analytical Chemistry*, *25*, 647–654, doi:10.1016/j.trac.2006.05.001.

Bluth, G. J. S., S. D. Doiron, C. C. Schnetzler, A. J. Krueger, and L. S. Walter (1992), Global tracking of the SO_2 clouds from the June 1991 Mount Pinatubo eruptions, *Geophys. Res. Lett.*, *19*, 151–154, doi:10.1029/91GL02792.

Bobrowski, N. H. G., B. Galle, and U. Platt (2003), Detection of bromine monoxide in a volcanic plume, *Nature*, *423*, 273–276.

Boone, C., R. Nassar, K. A. Walker, Y. Rochon, S. D. McLeod, C. P. Rinsland, and P. F. Bernath (2005), Retrievals for the atmospheric chemistry experiment Fourier transform spectrometer, *Appl. Opt.*, *44*, 7218–7231.

Carn, S. A., A. J. Prata, N. A. Kroktov, K. Yang, and A. J. Krueger (2009), Satellite measurements of volatile emissions from recent North Pacific Arc eruptions, paper presented at Geological Society of America Annual meeting, Portland, Ore.

Clapp, M. L., R. E. Miller, and D. R. Wornsnop (1995), Frequency-dependent optical constants of water ice obtained directly from aerosol extinction spectra, *J. Phys. Chem.*, *99*, 6317–6326.

Clarisse, L., P.-F. Coheur, S. Chefdeville, J.-L. Lacour, D. Hurtmans, and C. Clerbaux (2011), Infrared satellite observations of hydrogen sulfide in the volcanic plume of the August 2008 Kasatochi eruption, *Geophys. Res. Lett.*, *38*, doi:10.1029/2011GL0474402.

Dufour, G., S. Szopa, M. P. Barkley, C. D. Boone, A. Perrin, P. I. Palmer, and P. F. Bernath (2009), Global upper-tropospheric formaldehyde: seasonal cycles observed by the ACE-FTS satellte instrument, *Atmos. Chem. Phys.*, *9*, 3893–3910, doi:10.5194/acp-9-3893-2009.

Dutton, E. G., and J. R. Christy (1992), Solar radiative forcing at selected locations and evidence for global lower tropospheric cooling following the eruption of El Chichon and Pinatubo, *Geophys. Res. Lett.*, *19*, 2313–2316, doi:10.1029/92GL02495.

Eldering, A., F. W. Irion, A. Y. Chang, M. R. Gunson, F. P. Mills, and H. M. Steele (2001), Vertical profiles of aerosol volume from high-spectral-resolution infrared transmission measurements, I. Methodology, *Appl. Opt.*, *40*, 3082–3091.

Eldering, A., B. H. Kahn, F. P. Mills, F. W. Irion, H. M. Steele, and M. R. Gunson (2004), Vertical profiles of aerosol volume from high-spectral-resolution infrared transmission measurements: Results, *J. Geophys. Res.*, *109*, doi:10.1029/2004JD004623.

Forster, P., et al. (2007), *Changes in atmospheric constituents and radiative forcing. In: Climate change 2007: The physical science basis. Contribution of working group I to the fourth assessment report of the Intergovernmental Panel on Climate Change*, Cambridge University Press, Cambridge (UK) and New York (NY, USA).

Fromm, M., J. Alfred, and M. Pitts (2003), A unified, long-term, high-altitude stratospheric aerosol and cloud database using SAM II, SAGE II, and POAM II/III data: Algorithm description, database definition, and climatology, *J. Geophys. Res.*, *108*, doi:10.1029/2002JD002772.

Gilbert, K. L., et al. (2007), The onboard imagers for the Canadian ACE SCISAT-1 mission, *J. Geophys. Res.*, *112*, doi:10.1029/2006JD007714.

González Abad, G., et al. (2011), Ethane, ethyne and carbon monoxide concentrations in the upper troposphere and lower stratosphere from ACE and GEOS-Chem: a comparison study, *Atm. Chem. Phys. Discuss.*, *11*, 13,099–13,139, doi: 10.5194/acpd-11-13099-2011.

Goodman, J., K. G. Snetsinger, R. F. Pueschel, G. V. Ferry, and S. Verma (1994), Evolution of Pinatubo aerosol near 19 km altitude over western North America, *Geophys. Res. Lett.*, *21*, 1129–1132, 94GL00696.

Gunson, M. R., et al. (1996), The Atmospheric Trace Gas Spectroscopy (ATMOS) experiment: deployment on the ATLAS Space Shuttle mission, *J. Geophys. Res.*, *23*, 2333–2339.

Hansen, J. E., and L. D. Travis (1974), Light scattering in planetary atmospheres, *Space. Sci. Rev.*, *16*, 527–610.

Haywood, J., and O. Boucher (2000), Estimates of the direct and indirect radiative forcing due to tropospheric aerosols: a review, *Reviews of Geophysics*, *38*, 513–543.

Haywood, J. M., et al. (2010), Observation of the eruption of the Sarychev volcano and similations using the HadGEM2 climate model, *J. Geophys. Res.*, *115*, doi:10.1029/2009JD014447.

Hofmann, D. J., and J. M. Rosen (1983), Sulfuric acid droplet formation and growth in the stratosphere after the 1982 eruption of El Chichon, *Science*, *222*, 325–327.

Houghton, J. T. (2003), *The physics of atmospheres*, 2nd ed., Cambridge University Press, Cambridge.

Humphreys, W. J. (1929), *Physics of the air*, 2nd ed., McGraw-Hill Book Company, New York.

Jacob, D. J. (1999), *Introduction to atmospheric chemistry*, Princeton University Press, Chichester (UK) and Princeton (New Jersey, USA).

Jacobson, M. Z. (1999), *Fundamentals of atmospheric modeling*, 1st ed., Cambridge University Press, Cambridge (UK).

Jaenicke, R. (1978), Über die Dynamik atmosphärischer Aitkenteilchen, *Ber. Bunsenges. Phys. Chem.*, *82*, 1198–1202.

Jones, A., J. Haywood, O. Boucher, B. Kravitz, and A. Robock (2010), Geoengineering by stratospheric SO_2 injection: results from the Met Office HadGEM2 climate model and comparison with the Goddard Institute for Space Studies ModelE, *Atmos. Chem. Phys.*, *10*, 5999–6006.

Karagulian, F., L. Clarisse, C. Clerbaux, A. J. Prata, D. Hurtmans, and P. F. Coheur (2010), Detection of volcanic SO_2, ashes and H_2SO_4 using the Infrared Atmospheric Sounding Interferometer (IASI), *J. Geophys. Res.*, *115*, D00L02.

Kern, C. (2009), Spectroscopic measurements of volcanic gas emissions in the ultraviolet wavelength region, Ph.D. thesis, Ruprecht-Karls Universität Heidelberg.

Kidder, S. Q., and T. H. Vonder Haar (1995), *Satellite Meteorology: An introduction (international geophysics)*, Academic Press, London (UK) and San Diego (California, USA).

Mahieu, E., et al. (2005), Comparisons between ACE-FTS and ground-based measurements of stratospheric HCl and $ClONO_2$ loadings at narthern latitudes, *Geophys. Res. Lett.*, *32*, doi:10.1029/2005GL022403.

Massie, S. T., T. Deshler, G. E. Thomas, J. L. Mergenthaler, and J. M. Russell (1996), Evolution of the infrared properties of the Mount Pinatubo aerosol cloud over Laramie, Wyoming, *J. Geophys. Res.*, *101*, 23,007–23,019.

Mattis, I., et al. (2010), Volcanic aerosol layers observed with multiwavelength Raman lidar over central Europe in 2008-2009, *J. Geophys. Res.*, *115*, doi:10.1029/2009JD013472.

McElroy, C. T., et al. (2007), The ACE-MAESTRO instrument on SCISAT: description, performance, and preliminary results, *Appl. Opt.*, *46*, 4341–4356.

McHugh, M., B. Magill, K. A. Walker, C. D. Boone, P. F. Bernath, and J. M. Russell (2005), Comparison of atmospheric retrievals from ACE and HALOE, *Geophys. Res. Lett.*, *32*, doi:10.1029/2005GL022403.

Oberbeck, V., E. F. Danielson, K. G. Snetsinger, G. V. Ferry, W. Fong, and D. M. Hayes (1983), Effect of the eruption of El Chichon on stratospheric aerosol size and composition, *Geophys. Res. Lett.*, *10*, 1021–1024.

Parker, D. E., H. Wilson, P. Jones, J. R. Christy, and C. K. Folland (1996), The impact of Mount Pinatubo on world-wide temperatures, *Int. J. Climatol.*, *16*, 487–497.

Petelina, S. V., et al. (2005), Validation of ACE-FTS stratospheric ozone profiles against Odin/OSIRIS measurements, *Geophys. Res. Lett.*, *32*, doi:10.1029/2005GL022377.

Pinnick, R. G., J. M. Rosen, and D. J. Hofmann (1976), Stratospheric aerosol measurements, III, Optical model calculations, *J. Atmos. Sci.*, *33*, 304–314.

Pinnick, R. G., S. G. Jennings, and P. Chylek (1980), Relationship between extinction, absorption, backscattering, and mass content of sulforic acid aerosol, *J. Geophys. Res.*, *85*, 4059–4066.

Pollack, J. B., O. B. Toon, C. Sagan, A. Summers, B. Baldwin, and W. van Camp (1976), Volcanic Explosion and Climatic Change: A Theoretical Assesment, *J. Geophys. Res.*, *41*, 2768–2780.

Press, W. H., S. A. Teukolosky, W. T. Vetterling, and B. P. Flannery (1992), *Numerical Recipes in Fortran 77 - Volume 1*, 2nd ed., Cambridge University Press.

Pueschel, R. F., P. B. Russell, D. A. Allen, G. V. Ferry, K. G. Snetsinger, J. M. Livingston, and S. Verma (1994), Physical and optical properties of the Pinatubo volcanic aerosol: Aircraft observations with impactors and a Sun-tracking photometer, *J. Geophys. Res.*, *99*, 12,915–12,922, 94JD00621.

Reeves, C. E., and S. A. Penkett (2003), Measurements of peroxides and what they tell us, *Chem. Rev.*, *103*, 5199–5218.

Reiner, T., and F. Arnold (1994), Laboratory investigation of gaseous sulfuric acid formation via SO_3+H_2O+M→H_2SO_4+M: Measurement of the rate constant and product identification, *J. Chem. Phys.*, *101*, 7399–7407.

Roedel, W. (2000), *Physik unserer Umwelt*, 3rd ed., Springer Verlag.

Rose, W., G. J. S. Bluth, and G. G. J. Ernst (2000), Integrating retrievals of volcanic cloud characteristics from satellite remote sensors: A summary, *Philos. Trans. R. Soc. A*, *358*, 1585–1606.

Rothman, L. S., D. Jacquemart, A. Barbe, et al. (2005), The HITRAN 2004 molecular spectroscopic database, *J. Quant. Spectrosc. Radiat. Transf.*, *96*, 139–204, doi:10.1016/j.jqsrt.2004.10.008.

Sato, M., J. E. Hansen, M. P. McCormick, and J. B. Pollack (1993), Stratospheric aerosol optical depths, 1850-1990, *J. Geophys. Res.*, *98*, 22,987–22,994, doi:10.1029/93JD02553.

Seinfeld, J. H., and S. N. Pandis (1998), *Atmospheric chemistry and physics: From air pollution to climate change*, 1st ed., John Wiley & Sons, Inc., New York.

Sen, B., G. C. Toon, J.-F. Blavier, E. L. Fleming, and C. H. Jackman (1996), Baloonborne observations of midlatitude fluorine abundance, *J. Geophys. Res.*, *101*, 9045–9054.

Sen, B., G. C. Toon, G. B. Osterman, J.-F. Blavier, J. J. Margitan, R. J. Salawitch, and G. K. Yue (1998), Measurements of reactive nitrogen in the stratosphere, *J. Geophys. Res.*, *103*, 3571–3585.

Shen, T.-L., P. J. Wooldridge, and M. J. Molina (1995), *Stratospheric pollution and ozone depletion, in Composition, chemistry, and climate of the atmosphere*, 394–442 pp., Van Nostrand Reinhold, New York.

Sheridan, P. J., R. C. Schnell, D. J. Hofmann, and T. Deshler (1992), Electron microscope studies of Mt. Pinatubo aerosol layers over Laramie, Wyoming during summer 1991, *Geophys. Res. Lett.*, *19*, 203–206.

Sica, M. L., et al. (2008), Validation of the Atmospheric Chemistry Experiment (ACE) version 2.2 temperature using ground-based and space-borne measurements, *Atmos. Chem. Phys.*, *8*, 35–62.

Sioris, C. E., C. D. Boone, P. F. Bernath, J. Zou, C. T. McElroy, and C. A. McLinden (2010), Atmospheric Chemistry Experiment (ACE) observations of aerosol in the upper troposphere and lower stratosphere from the Kasatochi volcanic eruption, *J. Geophys. Res.*, *115*, doi:10.1029/2009JD013469.

Solomon, S., J. Daniel, R. N. Ill, E. Duton, and L. W. Thomason (2011), The persitently variable "backgound" stratospheric aerosol layer ans global climate change, *Science*, *333*, 866 – 870.

Soucy, M.-A., F. Chateauneuf, C. Deutsch, and N. Etienne (2002), ACE-FTS instrument detailed design, *SPIE*, *4814*, 70–81.

Steele, H., A. Eldering, B. Sen, G. C. Toon, F. P. Mills, and B. H. Kahn (2003), Retrieval of stratospheric aerosol size and composition information from solar infrared transmission spectra, *Appl. Opt.*, *42*, 2140–2154.

Steele, H. M., J. D. Lumpe, R. P. Turco, R. M. Bevilacqua, and S. T. Massie (1999), Retrievals of aerosol surface area and volume densities from extinction measurements: Application to POAM II and SAGE II, *J. Geophys. Res.*, *104*, 9325–9336.

Steele, H. M., A. Eldering, and J. D. Lumpe (2006), Simulations of the accuracy in retrieving stratospheric aerosol effective radius, composition, and loading from infrared spectral transmission measurements, *Appl. Opt.*, *45*, 2014–2027.

Textor, C., H.-F. Graf, C. Timmreck, and A. Robock (2004), *Emissions from volcanoes*, 269–303 pp., Klewer, Dordrecht, Netherlands, In: Grainer, C., Artaxo, P. and Reeves, C.: Emissions of Atmospheric trace components.

Tisdale, R. T., D. L. Glandorf, M. A. Tolbert, and O. B. Toon (1998), Infrared optical constant of low-temperature H_2SO_4 solutions representative of stratospheric sulfate aerosol, *J. Geophys. Res.*, *103*, 25,353–25,370.

Toon, O. B., and J. B. Pollack (1976), A global average model of atmospheric aerosol for radiative transfer calculations, *J. Appl. Meteorol.*, *15*, 225–246.

Toon, O. B., J. B. Pollack, and B. N. Khare (1976), The optical constants of serveral atmospheric aerosol species: Ammonium sulfate, aluminium oxide, and sodium chloride, *J. Geophys. Res.*, *81*, 5733–5748.

Vanhellemont, F., et al. (2008), Aerosol extinction profiles at 525 nm and 1030 nm derived from ACE imager data: comparisons with GOMOS, SAGE II, SAGE III, POAM III, and OSIRIS, *Atmos. Chem. Phys.*, *8*, 2027–2037.

Wang, P.-H., M. P. McCormick, T. J. Swissler, M. T. Osborn, W. H. Fuller, and G. K. Yue (1989), Interference of stratospheric aerosol composition and size distribution-from SAGE II satellite measurements, *J. Geophys. Res.*, *94*, 8435–8446, 88JD03965.

Yang, P., K. N. Liou, and W. P. Arnott (1997), Extinction efficiency and single-scattering albedo for laboratory and natural cirrus clouds, *J. Geophys. Res.*, *102*, 21,825–21,835.

B. Appendix

B.1. List of Figures

List of Figures

B.2. List of Tables

List of Tables

B.3. Acknowledgement

First, I would like to say thank you to my supervisor Prof Peter Bernath, who gave me the opportunity to conclude my Masters by Research project in this interesting and enjoyable topic and who helped me with constructional critiques, suggestions and motivation throughout the whole year, it was a pleasure to work for him. I am also indebted to Prof Peter Bernath for his support and motivation in allowing me to author a paper on my research that I have completed during my Masters by research at the University of York.

I am deeply indebted to Prof Annmarie Eldering, who provided the basic program for the retrieval of the sulphate aerosol properties and spent a great deal of work and much time on the phone to explain the structure of her program, which solved many problems and overcame barriers. In addition, she also edited my paper, giving me much constructive criticism and comments to improve my work. Without her, it would not have been possible for me to do my research as successful as it is now.

Furthermore, I thank Sean McLeod and Chris Boone for their support and help during my project, in sending and explaining important programs, helping me with the retrievals and finishing the program to retrieve the SO_2 VMR from ACE-FTS data.

I would like to thank the Bernath group, with whom it was always a pleasure to share the office, lunch breaks and social time with, throughout the year. I would also like to thank them for their support and critique of my written thesis. I would like to express my gratitude especially to Ganzalo Gonzaléz Abad for introducing me to the world of programming and his assistance in solving "unsolvable" problems in my own written programs.

I thank my parents, who made it possible for me to study, who supported my plans and provided financial support throughout my whole degree. I would like to express my gratitude to my wonderful fiancé David Griffin, who motivated me, supported me through my "ups" and "downs" and who was always there for me, when I needed someone to talk to. Thank you as well, David, for improving my spoken and written English skills, you are by far the best English teacher ever!

B.4. Declaration

I, Debora Doeringer, confirm that my work submitted in this thesis is my own and that all used sources and resources, in this thesis, are quoted correctly and accurately.

Parts of Chapter 4 and 5 are in the process of being submitted to the Journal of Geophysical Research (JGR).

Signature: _____ Date: _____